Magnetic Actuation of Biological Systems

DISSERTATION

Presented in Partial Fulfillment of the Requirements for the Degree Doctor of Philosophy in the Graduate School of The Ohio State University

By

Stephanie D. Lauback, M.S., B.S.

Graduate Program in Physics

The Ohio State University

2017

Dissertation Committee:

R. Sooryakumar, Advisor

Fengyuan Yang

Ciriyam Jayaprakash

Thomas Humanic

Abstract

Central to the advancement of many biomedical and nanotechnology capabilities is the capacity to precisely control the motion of micro and nanostructures. These applications range from single molecule experiments to cell isolation and separation, to drug delivery and nanomachine manipulation. This dissertation focuses on actuation of biological micro- and nano-entities through the use of weak external magnetic fields, superparamagnetic beads, and ferromagnetic thin films. The magnetic platform presents an excellent method for actuation of biological systems due to its ability to directly control the motion of an array of micro and nanostructures in real-time with calibrated picoNewton forces. The energy landscape of two ferromagnetic thin film patterns (disks and zigzag wires) is experimentally explored and compared to corresponding theoretical models to quantify the applied forces and trajectories of superparamagnetic beads due to the magnetic traps. A magnetic method to directly actuate DNA nanomachines in real-time with nanometer resolution and sub-second response times using micromagnetic control was implemented through the use of stiff DNA micro-levers which bridged the large length scale mismatch between the micro-actuator and the nanomachine. Compared to current alternative methods which are limited in the actuation speeds and the number of reconfiguration states of DNA constructs, this magnetic approach enables fast actuation ($\sim$ milliseconds) and reconfigurable conformations achieved through a continuous range of finely tuned steps. The system was initially tested through actuation of the stiff arm tethered to the surface, and two prototype DNA nanomachines (rotor and hinge) were successfully actuated using the stiff mechanical lever. These results open new possibilities in the development of functional robotic systems at the molecular scale. In exploiting the use of DNA stiff levers, a new technique was also

developed to investigate the emergence of the magnetization of individual superparamagnetic beads as a function of the applied field. Last, since proteins are frequently used for surface adhesion in assembling biomedical devices, preliminary tests were implemented to dynamically pattern proteins on a substrate using transformed *E. coli* that are magnetically labeled.

To my Heavenly Father, Lord, Savior and Friend.

Acknowledgments

To say that I have reached this goal on my own would be a huge understatement. I truly could not have made it this far without the help and support of many and would like to take a moment to thank those who have been a part of this journey with me. First, thanks to my advisor, Dr. Sooryakumar, for his support and advice over these past five years. He nurtured an encouraging and caring environment in the lab and motivated and inspired all of us. Thanks to the professors on my committee, Dr. Yang, Dr. Jayaprakash and Dr. Humanic. Much of this work has been in collaboration with other faculty and I am very thankful to each of them. Thanks, Dr. Castro, for all your experimental advice in assembling these DNA origami machines and letting me be a part of your lab. I have learned so much from the few years here. Thanks to Dr. Brian Lower and Dr. Steven Lower for your help in developing the protein pen. Additional thanks to other collaborators who have greatly assisted in various projects in the lab including Dr. Lee, Dr. Chalmers, Dr. Kwiek, and Dr. Besik.

I would also like to thank my physics undergraduate professor including Dr. Caragiu, Dr. Theisen, Dr. Pinkney, and Dr. Sheridan. The individual care of these professors and their belief in me were largely part of the reason I continued to pursue a graduate degree. Thanks to Dr. Caragiu for all your guidance even after I graduated! Thanks to past undergraduate research advisors who gave me the opportunity to conduct research in their lab in the summer through different REUs including Dr. Robert Collins at the University of Toledo, Dr. Chris Hammel at The Ohio State University, and Dr. Nick Wu at West Virginia University. Furthermore, had it not been for my caring high school physics teacher, Mrs. DeBrosse, I am not sure I would have ended up studying physics. It was

through her that physics really began to click and I started to catch a glimpse of how well physics explains our world.

I am so thankful for all the awesome past and present students in Dr. Sooryakumars lab who I have had the privilege of working with. Thanks to Dr. Marci Howdyshell who first introduced me to the lab and was an amazing mentor. Thanks to Dr. Greg Vieira who graduate before I started working in the lab but has been a support in answering many of my questions through email. Thanks to Dr. Mike Prikockis for all your advice and for being a great office mate. Thanks to Christopher Pease and Chris Pierce for all of your experimental help and great conversations. You both were always willing to discuss ideas and interested in how my research was coming. It has been a pleasure working with you. Thanks to Hiran Wijesinghe for all your help especially with simulations. Thanks also to Dr. Jon Zizka and Dylan Roderick for being great office mates even though our research did not overlap much. And thanks Jon for all your teaching job search advice and encouragement. Thanks to Kara Mattioli for all your help on the DNA nanomachines project and for your friendship. You were such a blessing to me. Thanks to the undergraduates that have worked with me on various projects and have been a tremendous help. Thanks to Pranav Pamidigantam for your help with the characterizing the wires, Carrie Gerding for your help in characterizing the disks, Emma Brown for your help growing the *E. coli* and developing the protein pen, Max Armstrong and Thomas Rudibaugh for your help with the DNA nanomachines project and James Etheridge for your help in characterizing the MyOne Dynabeads. I could not have done this without each of you. Thanks also to George Vogt for developing Lodestone and Magmeastro and therefore, making it much easier to run magnetic actuation experiments in other labs. Thanks to Gen Xu for your help in fixing the Lodestones.

Thanks to all the students in the Nanoengineering and Biodesign Lab (NBL). Thank you for helping me to understand the technique of folding DNA Origami structures and for being so welcoming to me in your lab. It has been such a pleasure working with each of you. Thanks to Alex Marras for the tremendous amount of helpful advice, for taking all of our TEM images and for making all of the solid works images of our structures. Thanks to Dr. Mike Hudoba for all your advice in surface attachment. Thanks to Dr. Chris Lucas

for your advice in troubleshooting different DNA Origami problems that came up and for your warm welcomes. You always cared about how everyone was doing in the lab and made everyone feel so welcome. Thanks to Randy Patton for all your guidance and for all your help on the TIRF and with slide prep. Thanks to Josh Johnson for your advice, for your help with slide prep and for keeping everything work. Thanks to Jenny Le for all your help and for keeping the lab running. Thanks to Molly Mollica for initially training me on the TIRF and answering questions I had even after you graduated. Thanks to Ehsan Akbari for helping with the platform and for great conversations. I am so thankful that I have been able to work with all students in NBL including postdoc, graduate and undergraduate students. You guys are such a fun group to be a part of.

Additional thanks to postdocs and graduate students in other labs who have collaborated on various projects. Thanks to Dr. Lingqian Chang for your help with nano electroporation. Thanks to Dr. Veysi Malkoc for answering so many of my endless questions and teaching me how to fabricate PDMS nanochannels. Thanks to Dr. Daniel Gallego Perez for all your advice in electroporation and nanochannel fabrication. Thanks to Eric Mumper for supplying MTB and for explaining the biology of these bacteria. Thanks to Lumarie Perez-Guzman for helping me to understand some aspects of molecular biology and for helping me to run gels. Thanks to students in Dr. Yangs group who have provided CoFe patterned thin films over the years to our group including Dr. Adam Houser, Dr. Brian Peters, Dr. Jeremy Lucy, and Jack Brangham.

Thanks to the staff in the physics department as well as in the NSEC and NTW facility for your assistance and support. Thanks to Paul Steffen and Denis Pelekov for helping to keep us safe in the lab. Thanks to Peter Janney, Derek Ditmer, Pete Gosser and Camelia Selcu for all the equipment training and advice. Thanks also to the administrators including Kris Dunlap, Trisch Longbrake, and Crystal Moloney for answering questions, reserving rooms and just keeping things going.

Thanks for the friends who have been a huge support over the years and made many lasting memories. Thanks to Natasha Nuzum, Oksana Strizheus, Deanna Rowley and Carol Napp for all your love and prayers. Your fellowship has meant so much to me and I have

been greatly sharpened by each you. Thanks for all the great memories! I will deeply miss our time together. Thanks to my small group and church family. I have been greatly blessed and encouraged by you.

My family has also been such a support over the years and I am very thankful for each of you. Thanks to the Lauback family including Mom and Dad Lauback, Jamie and Amy and Uncle Randy and Aunt Snyder for all your love and support in helping me reach this goal. Thanks to my amazing siblings and in-laws, Jon and Heather, Amber and Ryan and Bethany for all you love and encouragement. Thanks to my parents who have been there for me every step of the way. I could always depend on you for a word of encouragement and arms that were open wide. Thanks to all my family for their endless prayers for me. Thanks to my loving husband and friend, David. I couldn't have made it through grad school without your endless love and support. Thanks for all the walks in the park and the many great memories! Finally, I want to thank my Heavenly Father, Lord, Savior and Friend for strengthening me each day, for giving me everlasting life and for giving me a reason to live each day.

Grant funding for this work was provided by the U.S. Army Research Office under Contract W911NF-10-1-0353 and W911NF-14-1-0289, and in part by The Ohio State University Materials Research Seed Grant Program, funded by the Center for Emergent Materials, an NSF-MRSEC, grant DMR-1420451.

Vita

March 26, 1990 ..... Born—Dayton, OH

May, 2012 ..... B.S., Ohio Northern University, Ada, OH

August, 2015 ..... M.S., The Ohio State University, Columbus, OH

Awards

2015 ..... Nominated for 2015 American Association of Physics Teachers Outstanding GTA Award

2015 ..... Hazel Brown Outstanding Teaching Assistant Award

2015 ..... OSU Materials Week Best Student Poster Award

Publications

M. L. Howdyshell, M. Prikockis, S. Lauback, G. B. Vieira, K. Mahajan, J. Winter, R. Sooryakumar. "Deterministic and Stochastic Trajectories of Magnetic Particles: Mapping Energy Landscapes for Technology And Biology". *IEEE Transactions on Magnetics*, **50**,2303507 (2014).

R. Adur , S. Lauback, P. Banerjee , I. Lee , V. J. Fratello, P. C. Hammel. "Anisotropy and Field-Sensing Bandwidth in Self-Biased Bismuth-Substituted Rare-Earth Iron Garnet Films: Measurement by Ferromagnetic Resonance Spectroscopy". *IEEE Transactions on Magnetics*. **49**,2899 (2013).

G. M. McGuirk, H. Shin, M. Caragiu, S. Ash, P. K. Bandyopadhyay, R. H. Prince, R. D. Diehl. "Au(111) surface phases induced by adsorption: LEED I(E) analysis of (1x1) and (5x5) Au(111-S phases". *Surf. Sci.* **610**,42 (2013).

Conference Presentations

S. Lauback, K. Mattioli, M. Armstrong, C. Miller, C. Pease, C. Castro, R. Sooryakumar. American Physical Society March Meeting, *Magnetic Actuation of Self-Assembled DNA Hinges* March 2016, Baltimore, Maryland.

S. Lauback, M. Armstrong, C. Miller, C. Peace, C. Castro, R. Sooryakumar. American Physical Society March Meeting, *Self-Assembled DNA Structures for Molecular Force Measurement: A Magnetically Actuated Approach* March 2015, San Antonio, Texas.

S. Lauback, E. Brown, L. Prez- Guzman, C. Peace, C. Pierce, B. H. Lower, S. K. Lower, R. Sooryakumar. American Physical Society March Meeting, *Magnetically-Actuated Escherichia coli System for Micro Lithography* March 2015, San Antonio, Texas.

S. Ash, G. M. McGuirk, H. Shin, P. K. Bandyopadhyay, R. H. Prince, R. D. Diehl, M. Caragiu. Ohio Space Grant Consortium (OSGC) Research Symposium, *Low Energy Electron Diffraction Structural Analysis of AU(111)-(5x5)-7S.* March 2012, Cleveland, Ohio.

S. Ash, G. M. McGuirk, H. Shin, P. K. Bandyopadhyay, R. H. Prince, R. D. Diehl, M. Caragiu. Ohio Space Grant Consortium (OSGC) Research Symposium, *Low Energy Electron Diffraction Structural Analysis of AU(111)-(5x5)-7S.* March 2012, Cleveland, Ohio.

Fields of Study

Major Field: Physics

Table of Contents

List of Figures

Figure **Page**

List of Tables

Table **Page**

Chapter 1
Introduction

The ability to control the motion of micro and nanostructures in real-time with well-defined spatial and temporal precision is fundamental to the development of many biomedical and nanotechnologies. For example, these types of fine control are necessary for single molecule [1–4] studies where polymer dynamics and molecular motors [5, 6] are further understood. Often biomedical devices require exact control and coordination of biological systems including manipulation, isolation, and separation of cells [7–17]. Biosensors [18, 19] and therapeutic devices involving electroporation [20–23] and drug delivery [24–32] also exploit this level of control over biological entities.

Several techniques have been developed to control the movement of structures on the micron and nanoscale which include optical tweezers [33–38], atomic force microscopy [39–44], conventional magnetic tweezers [45–51], dielectrophoresis [52**?** –61], acoustic traps [62–64], fluid flow [65–69], electromagnetic tweezers [70, 71] and micromagnetic tweezers via ferromagnetic thin films [10–12, 22, 72–102]. In the 1970s and 1980s, optical tweezers were first observed to apply forces and to localize dielectric beads via laser beams [33, 34]. Later, even biological particles were trapped using optical tweezers which used infrared light to reduce damage to living cells [35]. Studies have shown that optical tweezers can apply calibrated forces and displace objects over distances ranging from tens of nanometers to tens of micrometers with nanometer precision [36, 37]. Particles with varying indices of refraction could even be sorted using optical tweezers [38].

Although Atomic Force Microscopy (AFM) was initially developed for high resolution

imaging [39, 40], the associated cantilevers are effective as a probe to apply forces on biological objects with picoNewton resolution [41–43] and move particles with nanometer precision [44]. In 1950, conventional magnetic tweezers were first demonstrated to measure the cell's elastic properties by use of large permanent magnets that apply forces on magnetic beads [45]. Later these principles were applied to other biological systems to study the elasticity of DNA [46] with femto to nanoNewton forces [47–50]. Through the use of microcontact protein patterning, an array of DNA tethered magnetic beads were formed enabling multiplexing of the experiment [51].

In Dielectrophoresis (DEP), non-uniform electric fields are applied to dielectric particles including biological materials that become polarized and experience a force in the direction with the greatest electric field gradient [52]. Biological entities such as viruses, bacteria, and eukaryotic cells as well as submicron particles have been transported, localized, separated and concentrated using DEP [53**?** –59]. Furthermore, the direct planar orientation of nanorods has been controlled by changing the electric field [60, 103]. In addition, multiple cells have been manipulated by illuminating a pattern of light on a photosensitive surface to create non-uniform local electric fields for DEP manipulation [61]. In microfluidic channels, acoustic traps created using standing waves give dynamic control of the position of microparticles or cells [62–64]. Alternatively, microfluidic devices have been designed to directly control fluid flow on the microscale [65, 66], trap particles [67] and stretch DNA to study its properties [68, 69].

Although all these methods mentioned above demonstrate a range of abilities in controlling micro and nanostructures, they are accompanied by several limitations and disadvantages. In applying forces on biological entities, careful measures must be taken to reduce damage to the structure under study. Lasers in optical tweezers can induce photodamage and local heating. Stiff probes utilized in AFM can lead to damage of soft biological materials and electric fields utilized in DEP must be calibrated to low enough levels to prevent cell lysis. Additionally, optical tweezers, AFM, DEP and microfluidics are generally limited in selectivity. In utilizing optical tweezers, since any dielectric particle in solution can become trapped, high purity samples are necessary and are often diluted to low concentrations. In

AFM measurements, it can be difficult to distinguish the interactions of the tip with the targeted structure from nonspecific binding. DEP will transport any dielectric structure which includes most biological entities, and microfluidics will, in general, move most microscopic structures in the fluid, and thus they, generally, lack a high level of specificity. Furthermore, both optical tweezers and AFM are usually limited to studying single molecules, and conventional magnetic tweezers and microfluidics are constrained in their ability to finely manipulate structures.

Many of these challenges are overcome in the following methods by utilizing patterned thin films to form magnetic traps. The electromagnetic tweezers system creates local magnetic field gradients by sending current through patterned microwires and has been used in nanoparticle assemblies [70] and cell manipulation [71]. However, these devices are limited to producing low magnetic fields due to its restraint in current to reduce local heating. In contrast, a larger range of magnetic field gradients is produced from patterning soft and harder ferromagnetic thin films and demonstrate greater control over conventional magnetic tweezers [72]. In patterned magnetic thin films, domain walls can be controlled by changing the orientation of an external field [104–106]. Using this principle, particles and cells have been isolated, manipulated and separated through simple repetitive changes in the magnetic field [10–12, 73–98]. Using this micromagnetic system, structures are even assembled into different arrangements [107] with tunable interactions [11, 12, 108–110].

Unlike previous methods which could easily damage biological entities, the micromagnetic tweezers system rely upon magnetic fields which can directly probe biological enviorments and manipulate biological structures without adverse consequences. Additionally, this method is highly selective in that only magnetic particles are actuated. Due to the ability to readily label magnetic beads with proteins or anti-bodies most biological structures can be targeted and attached to magnetic beads for specific manipulation. Although some of the alternative methods of control over structures have shown some capability to simaltaneously actuate multiple structures, the micromagnetic system greatly enables multiplexing and cyclic experiments with fine control over spatial and temporal movement as well as are characterized by picoNewton forces [22, 99]. Furthermore, both micro and nanostructures

[100, 101] as well as various biological entities such as microtubules [102] are able to be actuated. Although the micromagnetic system enables applications in direct manipulation of biological micro- and nano-entities, demonstrates improved selectivity and permits multiplexing and cyclic manipulation, the ability to actuate with nanoscale resolution is limited. By utilizing stiff DNA microlever arms with a high aspect ratio (nanometer cross section and micron lengths) and a relatively large persistence length ($\sim$20 μm), this dissertation uses micromagnetic control to directly manipulate nanosystems with nanometer resolution. Underlying these studies is the use of weak external magnetic fields, superparamagnetic beads, and ferromagnetic thin films since they offer excellent avenues to controllably actuate biological structures on the micron and nanoscale.

In applying thin film magnetic traps to biological systems, quantifying the forces and the motion of superparamagnetic beads moving from one trap to another is useful in advancing these technologies. Chapter 4 studies the energy landscape of both soft ferromagnetic (NiFe) disks and hard ferromagnetic (CoFe) zigzag wires and compares the theoretical models that correlate experimental trajectories and forces of several different sizes of superparamagnetic beads. In Chapter 6, nanomachines assembled from DNA using the method of DNA origami (discussed in Chapter 5) were magnetically actuated using a stiff mechanical lever, superparamagnetic beads, and weak external magnetic fields. In applying this approach, nanostructures were directly actuated in real-time within milliseconds and reconfigured over a continuous range of finely tuned steps - an advantage over alternative systems that are generally limited to actuation times of minutes and reconfiguration amongst a few states. By exploiting the use of the stiff DNA lever, the anisotropic component (i.e. permanent and anisotropic induced moments) of superparamagnetic beads were studied and quantified in Chapter 7. These results offer a new approach to determining the factors that control the magnetic torques on superparamagnetic beads in uniform magnetic fields. Preliminary results for developing a method to dynamically pattern proteins on the surface using the thin film magnetic traps with magnetically labeled *E. coli* engineered to express the desired protein for patterning were presented in Chapter 8. Last, Chapter 9 summarize the results from this dissertation and presents future work that could be continued.

Chapter 2
Background of Micro-Magnetic Traps and Superparamagnetic Beads

2.1 Superparamagnetic Beads

Superparamagnetic beads are often integrated into nanoscience and biomedical technology due to their fast magnetic response in an external magnetic field and negligible remanence when the field is removed which limits bead aggregation. In the experiments discussed, superparamagnetic beads were used since they can be strongly magnetized through external fields to apply femto and picoNewton forces and yet still remain singular during storage. In order to create this characteristic, small iron oxide nanoparticles are embedded in the polystyrene matrix of a spherical bead [111].

2.1.1 Characteristics of Nanoparticles in Superparamagnetic Beads

In order for the superparamagnetic beads to hold these ideal characteristics, the majority of the nanoparticles need to be smaller than the single domain limit and the superparamagnetic limit [112–114]. In magnetic materials, multiple domains of non-uniform magnetization separated by domain walls exist in order to optimize its free energy. Magnetic domains form to reduce the demagnetizing energy by reducing stray fields however in return increase the exchange energy created by the preferred alignment of the magnetic moments as shown in Fig. 2.1. At a critical volume, it energetically cost more to form an additional domain

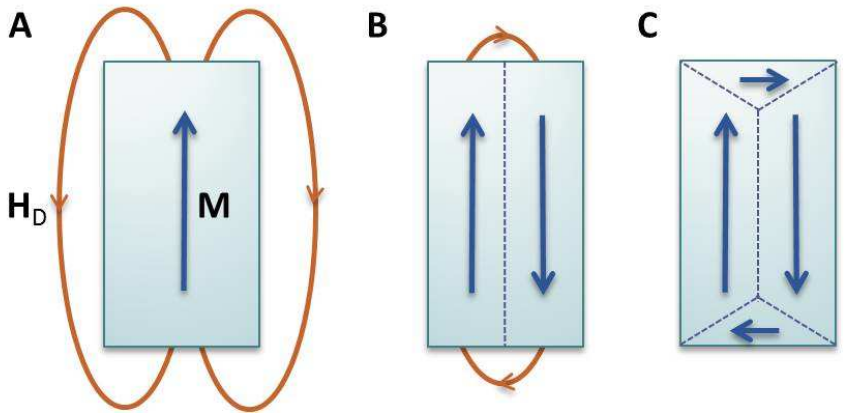

Figure 2.1: Multi-domains formation to decrease the demagnetizing energy. The demagnetizing energy from the stray fields caused by the surface charge of the magnetization is decreased from A to C as more domains are introduced to reduce the stray fields. However, as more domains are introduced the magnetic moments become less aligned and the exchange energy is increased.

then to remain as a single-domain state. This critical size, known as the single domain limit, is generally around a few tens of nanometers and is material dependent[112, 113].

Additionally, in order for the single domain particle to display paramagnetic behavior in the absence of an external field, the thermal fluctuations of the magnetic moment must be relatively rapid such that the magnetization averages to zero on short time scales. Due to the anisotropy of the particle, the magnetization of each single domain particle is considered to have a constant magnetic moment which randomly reverses direction due to thermal fluctuations. The magnetic moment is held to a specific orientation due to the anisotropy energy of the particle given by

$$E = KVsin^2(\theta) \tag{2.1}$$

where the magnetic anisotropy energy density is represented by K, the volume of the particle by V and the angle between the magnetization and the easy axis is represented by θ. The magnetic moment has two stable orientations along the easy axis which are anti-parallel to each other and are separated by a uniaxial anisotropy energy barrier (KV) shown in Fig. 2.2. As the particle size is decreased, the thermal energy (k_BT) needed to overcome the energy barrier and reorient directions is reduced. The superparamagnetic limit is therefore

defined by the size of the particle whose thermal energy is greater than the anisotropy energy barrier in which it appears as a paramagnet. The time that it takes for the magnetization to reverse is defined as Neel relaxation time (τ) and is given by the following expression

$$\tau = \tau_0 exp(\frac{KV}{k_B T}) \tag{2.2}$$

where τ_0 depends weakly on the temperature. Therefore, it is generally assumed to be constant, varying from ($10^{-13} - 10^{-9}$ seconds) [114]. As expressed in equation 2.2, the relaxation time depends on the ratio of the anisotropy energy compared to the thermal energy. Due to superparamagnetic relaxation, the magnetization hinges on the time scale of the experimental technique, also known as the characteristic measurement time (τ_m). If the relaxation is fast compared to τ_m ($\tau \gg \tau_m$), then the magnetization will reverse numerous times during a measurement. Hence, the magnetization will average to zero showing paramagnetic behavior in which the particle size is lower than the superparamagnetic limit. However, the magnetic susceptibility is much greater than paramagnets. If the relaxation is slow compared to the measurement time ($\tau \ll \tau_m$), then the magnetization does not reverse during that measurement. Hence, the magnetization will be static showing ferromagnetic behavior [112–115].

The temperature at which the relaxation time is equal to the time scale of the experimental technique ($\tau_m = \tau$) is the blocking temperature. For a single particle, the blocking temperature is given as

$$T_B = \frac{KV}{k_B ln(\frac{\tau_m}{\tau_0})} \tag{2.3}$$

where T_B is directly related to the size of the energy barrier [115]. Larger the energy barriers will trap the magnetization in one orientation at lower temperatures. As the particle size increases so will the blocking temperature. Therefore, the critical volume is also directly proportional to the temperature with the critical size being larger at higher temperatures. Bigger particles will become superparamagnetic at higher temperatures [114].

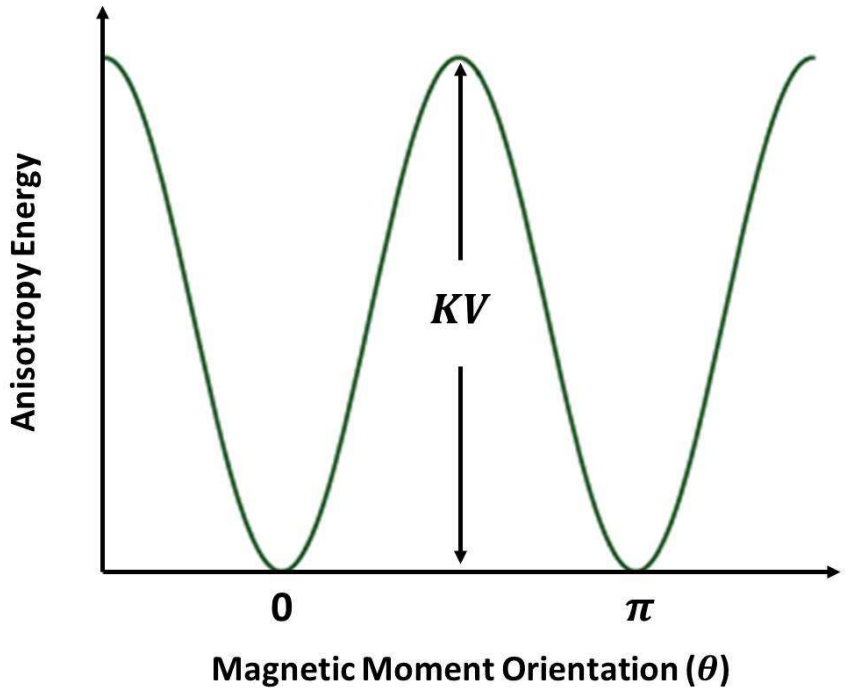

Figure 2.2: The magnetic moment of the nanoparticle has two stable orientations at the anisotropy energy minima 0 and π which is separated by an energy barrier.

2.1.2 Magnetization of Superparamagnetic Beads

The response of the entire bead from the net magnetization of each individual magnetic moment shows overall superparamagnetic behavior. The magnetization resulting from the vector sum of moments increase linearly as an external magnetic field is applied until it begins to saturate such that most of the magnetic moments are aligned with the field. The magnetization of the bead is given by

$$\mathbf{m} = \chi V \mathbf{H} \tag{2.4}$$

where the response of the bead is given by the magnetic susceptibility χ, the volume of the bead is V and the applied field is $\mathbf{H}$. In the linear regime before the magnetization begins to saturate, the susceptibility is approximated as a constant. The field at which the microbeads saturate is around 200 Oe [99]. Although, some residual magnetism as well as

overall bead anisotropy is observed, the strength of the permanent moment compared to the induced moment is relatively small. Generally, these anisotropic terms can be neglected in calculating forces on the bead in a non-uniform applied field except when specifically studying the torque on the bead caused by the permanent moment or easy axis from the induced moment. Cases, when the anisotropic components are the primary contributors of the torque an a superparamagnetic bead, will be discussed in more detail in Chapter 7.

2.2 Patterned Ferromagnetic Thin Films

Patterned soft and harder ferromagnetic thin films (permalloy and cobalt iron, respectively) were used to magnetically trap superparamagnetic beads. Through the use of external magnetic fields coupled with these ferromagnetic thin films, the beads could be transported to different trapping locations. The cobalt iron patterned thin films consisting of zigzag, straight and ″L″ shaped wires were initially magnetized using a large magnetic field (1 Tesla) after which the magnetization relaxed to lie in plane along the easy axis of the patterned structure as illustrated in Fig. 2.3. When small fields ($<$ 100 Oe) were applied, the magnetization of the CoFe films remained fixed. For permalloy patterns generally consisting of circles, octagons or other geometric shapes, the magnetization of the structure was random. However, as weak external fields were applied ($<$ 100 Oe), a net magnetization in the direction of the field resulted.

2.2.1 Magnetic Fields from Patterned Ferromagnetic Thin Films

Magnetic Point Charge Approximation

Magnetic fields from the change in magnetization at the domain walls can be calculated from the magnetic charge distribution and sometimes approximated as an effective magnetic point charge (ie. monopole). The magnetic charge density of the patterned ferromagnetic thin films can be calculated from the divergence of the magnetization ($\mathbf{M}$) given by

$$\rho_m = \nabla \cdot \mathbf{M} \tag{2.5}$$

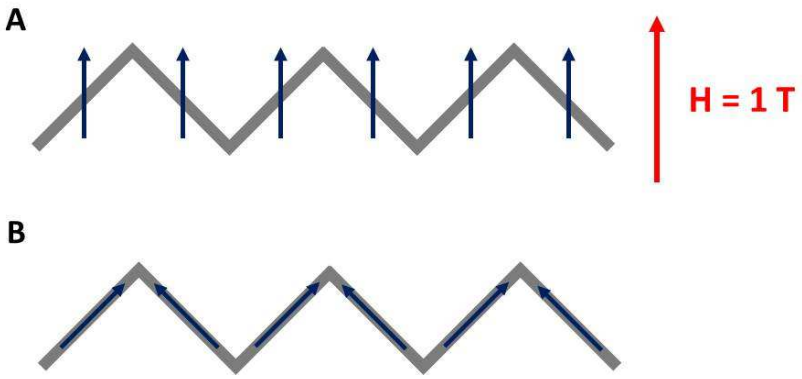

Figure 2.3: Magnetization of CoFe ZigZag Wires. (A) Initially, the wires are magnetized by applying a large external field of 1 T. (B) When the field is removed the magnetic moments relax along the direction of the wires due to shape anisotropy. Once magnetized, the magnetization of the wires do not change orientations in weak fields ($<$ 100 Oe).

The magnetic charge density only arises when the divergence is non-zero which occurs at the domain walls specifically found at the vertexes in the case of the CoFe zigzag wires or on the perimeter of the circular permalloy disks. The stray fields at the vertices where the domain walls arise can be approximated as a magnetic point charge in which the effective magnetic charge can be found by integrating over the region where the domain wall exists.The effective magnetic charge can be calculated using the divergence theorem

$$q_m = \iiint \rho_m \, dV = -\iiint \nabla \cdot \mathbf{M} \, dV = \oint_S \mathbf{M} \cdot \hat{n} \, dA \tag{2.6}$$

such that $\hat{n}$ is the outwardly directed normal to the surface [116]. In the case of the wires, only two sides of the surface will yield a non-zero flux resulting in the effective magnetic charge to be approximated as

$$q_m = 2M_s tw \tag{2.7}$$

such that M_s is the saturation magnetization of CoFe (16×10^5 A/m), t the thickness of the wires and w the width of the wires. This approximation best models wires whose length is much longer than the width and assumes a single domain wall whose magnetization is orientated toward or away from the domain wall on both sides of the wall. The field created

by the effective magnetic point charge at a distance r from the vertex is then equivalent to

$$\mathbf{H} = \frac{q_m}{4\pi}\frac{\mathbf{r}}{r^3} \tag{2.8}$$

Magnetic Charge Distribution Approximation

Additionally, the magnetization specifically around the vertex can be simulated using Object Oriented Micromagnetic Framework (OOMMF) which provides the magnetization profile as a 2D grid of magnetized cells [117]. The magnetization in the cell is confined to two dimensions since it generally lies in-plane due to the shape anisotropy of the thin film. To calculate the magnetization for CoFe patterned structures, an applied field of one Tesla was simulated and then removed allowing the magnetic moments in each cell to relax along their preferred anisotropy orientations along the wire. However, for permalloy structures, magnetic moments are initialized at random directions before reorientation through simulation of an applied weak in-plane field (between 10 Oe and 100 Oe). Using equation 2.5, the charge density can be calculated from the divergence of the simulated magnetization at each cell. The effective charge for each cell can then be determined from the charge density

$$q_m = \rho_m V_c \tag{2.9}$$

where V_c represents the cell volume. The stray fields produced at the domain walls can then be determined from the vector sum of the fields due to each effective point charge at each cell location using equation 2.8.

Magnetic Dipole Approximation

Furthermore, the magnetic moment in each quantized cell from the OOMMF simulations can be characterized as a magnetic dipole with a magnetic moment given by

$$\mathbf{m}_d(x, y, z) = \mathbf{M}(x, y, z)V_c \tag{2.10}$$

where $\mathbf{M}(x, y, z)$ is the magnetization in a specific cell of volume V_c. The magnetic field of

each dipole a distance r from the vertex can be calculated from

$$\mathbf{H} = \frac{1}{4\pi r^3}(3(\mathbf{m}_d \cdot \hat{r})\hat{r} - \mathbf{m}_d) \tag{2.11}$$

The vector addition of the stray fields at each dipole location gives the total field as a function of the position. The magnetic charge distribution approximation and magnetic dipole approximation give very similar results.

2.2.2 Potential Energy and Magnetic Forces

The potential energy of a magnetic dipole with moment $\mathbf{m}$ in an applied field is given by

$$U = -\mu_0 \mathbf{m} \cdot \mathbf{H}_{net} \tag{2.12}$$

where μ_0 is the permeability of free space and $\mathbf{H}_{net}$ is the total magnetic field. For a superparamagnetic bead, the magnetic moment varies as a function of the field (Equation 2.4). Therefore, the total potential energy as a function of the field can be calculated by integrating over the field.

$$dU = -\mu_0 d\mathbf{m} \cdot \mathbf{H} \tag{2.13}$$

$$d\mathbf{m} = \chi V d\mathbf{H} \tag{2.14}$$

$$U = -\mu_0 \chi V \int_0^{H_{net}} H dH \tag{2.15}$$

$$U = -\frac{1}{2}\mu_0 \chi V H_{net}^2 \tag{2.16}$$

Although the magnetic field produced at the domain walls from the patterned structures is much weaker than the external fields applied, it is vital in creating field gradients which will trap and repel the bead. The external field increases the trap strength and magnetizes the superparamagnetic bead, such that in aligning the magnetic moment with the stray fields at the domain wall, the bead will be attracted and repelled at specific domain walls.

Using the potential energy for a given bead in an applied magnetic field, the force on the bead can be calculated by differentiating the potential energy with respect to the position [91]:

$$F(\mathbf{r}) = -\nabla U(\mathbf{r}) = \frac{1}{2}\mu_0 \chi V \nabla H_{net}^2 \tag{2.17}$$

Chapter 3
Experimental Methods

3.1 Fabricating Patterned Magnetic Thin Films

Magnetic thin films were patterned onto substrates to trap and transport superparamagnetic beads as discussed in Chapter 2. Two methods have been used to pattern thin films which include electron beam (e-beam) lithography and photolithography. Micropatterns are created in photoresist polymers using a scanning electron microscope (as in e-beam) or ultraviolet light incident through a photomask (as in photolithography). In general, e-beam lithography has higher spatial resolution due to its direct exposure and is faster in making single prototypes since a mask is not required to be first fabricated.

3.1.1 CoFe Patterned Traps

E-beam lithography was used to pattern CoFe patterns (Fig. 3.1) with wire widths generally around 1 μm. Structures were often patterned on silicon substrates but were also patterned on glass coverslips for use on inverted microscopes. The substrate was initially cleaned by sonicating the substrate in acetone for 5 minutes followed by rinsing it with acetone, isopropyl alcohol and deionized water (DI). The substrate was then exposed to ultraviolet-ozone (UVO Cleaner 42, Jelight Company Inc.) for 5 - 10 minutes and any remaining moisture was removed by heating the sample on a hot plate ($\sim$ 190°C) for 5 minutes. Two e-beam resists are spun onto the substrate which assists in creating a uniform thickness and enabling better lift-off [118]. LOR 3B is initially spun for 5 seconds at 300 rpm to remove any bubbles and excess material and then spun for 1 minute at 3,000 rpm. The resist is

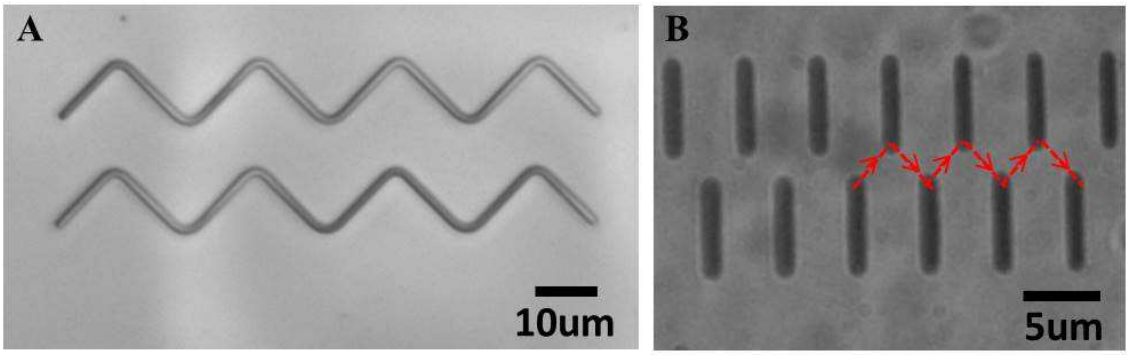

Figure 3.1: CoFe patterned Thin Films (A) Zigzag wires studied in Chapter 4. (B) ″Invisible″ zigzag wires designed for use on an inverted microscope enabling visualization of bead movement from one trapping sight to another. Image captured on an inverted microscope. Red lines show the zigzag path unblocked by thin film patterns.

cured on the hot plate by baking for 1 minute at 190°C. Following the same procedure, Shipley S1813 is spun initially for 5 seconds, then for 1 minute at 3,000 rpm followed by curing on the hot plate for 1 minute at 115°C. After the photoresist layers were deposited and cured on the substrate, the pattern is exposed for 18 milliseconds to an electron beam from a scanning electron microscope (FEI Helios Nanolab 600). Next, the patterns are developed by gently agitating the sample in MF-319 for 50 seconds. If not fully developed, the sample was agitated for an additional 30 seconds. $Co_{0.5}Fe_{0.5}$ is sputter deposited onto the chip and followed by a lift-off using heated acetone (60°C) removing the extra magnetic material and leaving behind the patterned CoFe wires. The wires were then capped by sputter deposition of a thin layer of SiO_2 (AJA Orion RF/DC Sputter Deposition Tool, RF, Ar 20 sccm, 3 mTorr, 500 W) to protect the wires from oxidation. Finally, the wires were magnetized in an external magnetic field of 1 Tesla.

3.1.2 Permalloy Patterned Traps

Permalloy ($Ni_{0.81}Fe_{0.19}$) disks (Fig. 3.2) were patterned on silicon wafers, quartz slides and glass coverslips using photolithography. Initially, the substrate was cleaned by rinsing it with acetone and isopropyl alcohol and then dried by baking for 5 minutes at 115°C. Using

a spin coater (CE 100CB Resist Coater and Hot Plate), two layers of positive photoresists are deposited onto the substrate to reduce any fences on the sides of the structure and improve the lift-off [118]. First, the lift-off resist LOR 2A is deposited at a rate 3,000 rpm and 10,000 rpm/s for 60 seconds followed by a 2 minute bake at 190°C. Then, S1813 resist is deposited at a rate 500 rpm and 300 rpm/s for 5 seconds and then increased to 3,000 rpm and 10,000 rpm/s for 45 seconds. The sample is then baked for 60 seconds at 115°C. The hardened resist is exposed to ultraviolet light for 3.5 seconds through a pre-designed mask in hard contact mode using an aligner (EV Group 620 Advanced Contact Aligner). Next, the sample is developed for 45 seconds by gently agitating the chip in Microposit^{TM} MF^{TM}-319 developer to remove the photoresist in the patterned region.

Once the sample is developed, 50-60 nm of permalloy ($Ni_{0.81}Fe_{0.19}$) is deposited using a sputter deposition tool (AJA Orion RF/DC Sputter Deposition Tool, DC, Ar 20 sccm, 3 mTorr, 200 W). If the substrate was a quartz wafer or glass coverslip, an initial 2 nm layer of titanium (RF, Ar 20 sccm, 3 mTorr, 300 W) was deposited before the permalloy to assist in the adhesion of the permalloy. Following deposition, the excess permalloy and titanium were removed in a lift-off step in which the sample was incubated in N-Methyl-2-Pyrrolidone (NMP) for 0.5 - 1 hour following a rinsing with isopropyl alcohol. The remaining permalloy disks were then capped by sputter deposition of a thin layer of SiO_2 (RF, Ar 20 sccm, 3 mTorr, 500 W) to protect the wires from oxidation.

3.2 Experiment Magnetic Setup

External magnetic fields could be applied to superparamagnetic beads on magnetic thin film patterns to trap and transport the bead or applied to superparamagnetic beads on a glass or silicon substrate to rotate or roll the bead. The setup generated in-plane magnetic fields using four orthogonal electromagnetics (opposite pole steel core electromagnets OP-2025, Magnetech Corp.) while generating an out-of-plane magnetic field from a wound copper solenoid surrounded by the electromagnets. The sample is placed in the center of the solenoid in which the magnetic fields are approximately uniform over the micron lengths

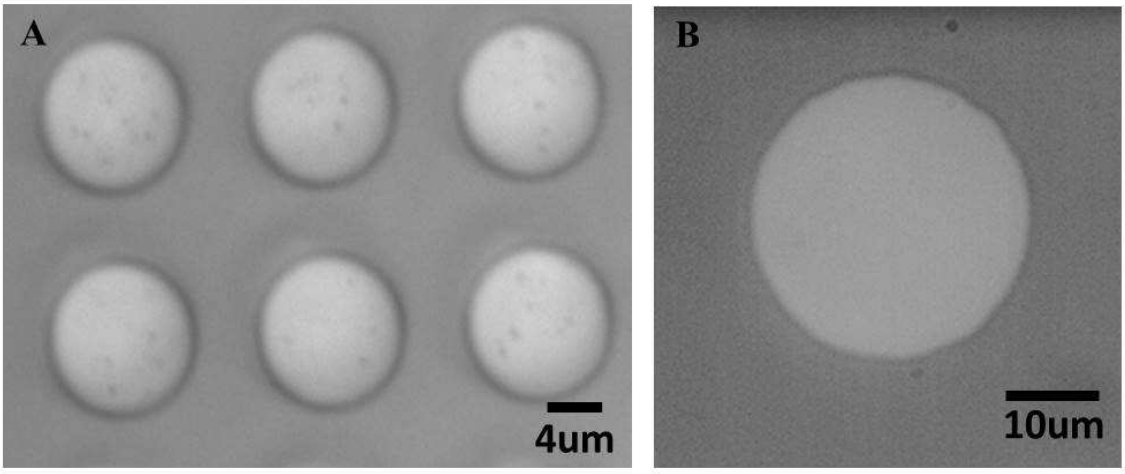

Figure 3.2: Permalloy Patterned Thin Films. Two sizes of disks were studied in Chapter 4 including disks with diameters of (A) 5 μm and (B) 30 μm. These disks were also used in Chapter 8 to transport beads labeled with *E. Coli* for applications in protein lithography.

studied.

Two setups were used to supply current to the electromagnets and solenoid. The first platform used a LabView interface to send current from three power supplies (solenoid, Kepco BOP 20-10ML; electromagnets, Kepco BOP 20-10ML4886) to the electromagnets and solenoid. However, it was necessary to design a platform which was portable and cost effective. New control hardware consisting of a small circuit board (″Lodestone″) was designed by Mr. George Voigt to interface the software programmed in C++ (″MagMaestro″), the small power supply (12 V, Mean Well NES-350-12), the electromagnets (OP-1212, Magnetech Corp.) and solenoid as illustrated in Fig. 3.3. The magnetic fields could be controlled through the software interface, an Xbox controller or voice commands.

It was also essential to design the the magnetic setup for use on different types of microscopes. Originally, the design was built for an upright microscope where the sample is imaged from above and the electromagnets and solenoid rested on the microscope stage. However, with an inverted microscope the electromagnets, solenoid, and sample need to be suspended so as to view the sample from below. Two separate designs were built such that one designed enabled use of the larger electromagnets (2.5 inches long, 2 inches in

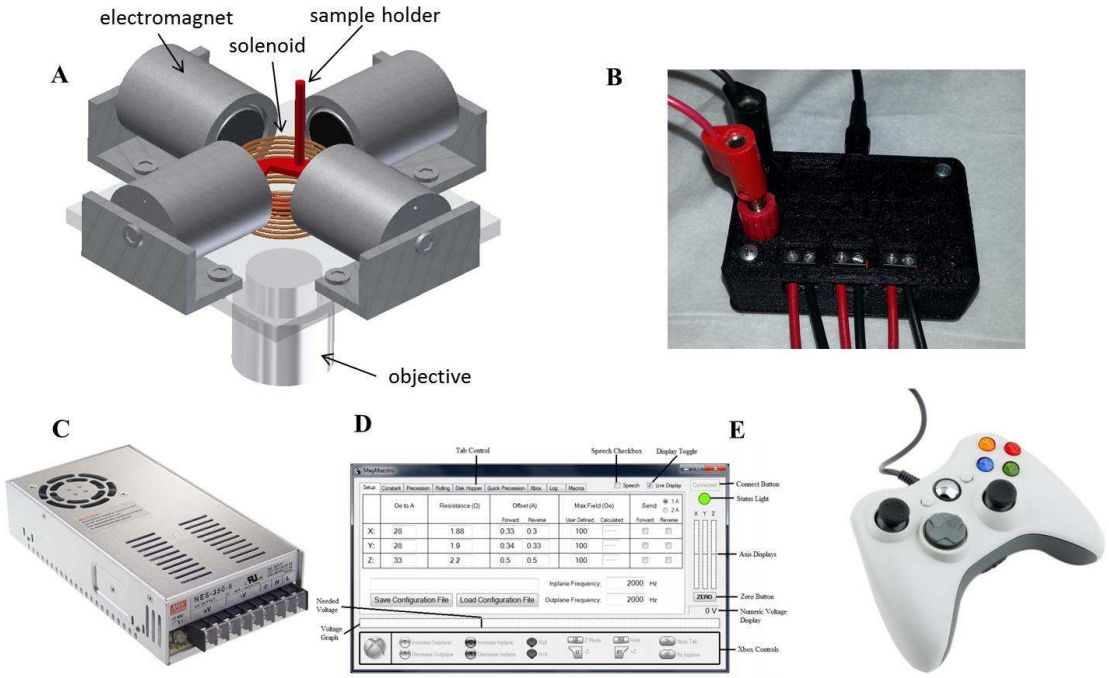

Figure 3.3: (A) External fields in three orthogonal directions are produced using four orthogonal electromagnets and one solenoid. For the inverted setup, the sample holder rests on an inside edge of the solenoid and is imaged through the objective from below. (B) Control hardware called Lodestone was designed to communicate to the (A) magnetic setup, (C) small 12 V Mean Well Nex-350-12 power supply and (D) the computer using a software interface called MagMaestro. An Xbox control was used to direct the external magnetic fields.

diameter, OP-2025, Magnetech Corp) utilized on the original upright microscope and the other design utilized smaller electromagnets (1.25 inches long, 1.25 inches in diameter, OP-1212, Magnetech Corp). Since the stage of a Nikon Eclipse Ti Microscope has a small removable inset platform, the magnetic setup was designed to fit the dimensions of the stage inset in order to be accessed on this microscope. The electromagnets and solenoid were suspended from a platform which rested in the stage inset. The solenoid had a 3D printed lip inside the center where a 3D printed sample holder rested. Smaller electromagnets (1.25 inches long, 1.25 inches in diameter, OP-1212, Magnetech Corp) had to be used due to the space limitation of the stage inset. However, larger electromagnets were used on inverted microscopes by shifting the entire stage down so that the objective could reach the sample

focal plane inside the solenoid. The electromagnets and solenoid could then set directly on top of the stage. A concentric opening was located on the platform in line with the solenoid which enabled imaging of the sample from below.

3.3 Channels

3.3.1 PDMS O-rings

In experiments where the introduction and removal of additional solutions were not required, a polydimethylsiloxane (PDMS) o-ring was used to confine the fluid and structures being studied. By changing the ratio of the curing agent to the liquid PDMS the thickness of the PDMS was tuned with a 1:1 ratio being the thinnest and 1:10 ratio being the thickest. After the liquid PDMS and curing agent were mixed together, it was placed under vacuum for 15 - 30 minutes to remove bubbles. Next, the mixture was poured into a petri dish and curried at 65°C for 30 minutes to 2 hours depending on the thickness. Alternatively, the PDMS could be curried at room temperature but would require several days to harden. After curing, a PDMS o-ring used to contain the fluid was created by cutting out a section of the PDMS and punching a hole in the center. When utilized on an upright microscope, a coverslip was often placed on top of the o-ring.

When the PDMS need to be bonded to the surface, two instruments could be used to oxidize the surface. Using the PTS Oxygen Plasma System (10 - 20 sccm O_2, 50 W power, 35 mT base pressure), the PDMS and substrate were exposed for 15 - 30 seconds to oxygen plasma and pressed together afterward. Alternatively, the PDMS and substrate were oxidized in UVO cleaner for 15 - 30 minutes and pressed together. The oxygen plasma method generally had faster bonding and the sample could be used immediately after bonding.

3.3.2 Tape Channels

In experiments which required introduction and removal of different reagents, tape channels were employed. Two strips of double sided tape were laid down in parallel along a coverslip (22 mm x 22 mm) to form the edges of the channel. A smaller coverslip (18 mm x 18 mm)

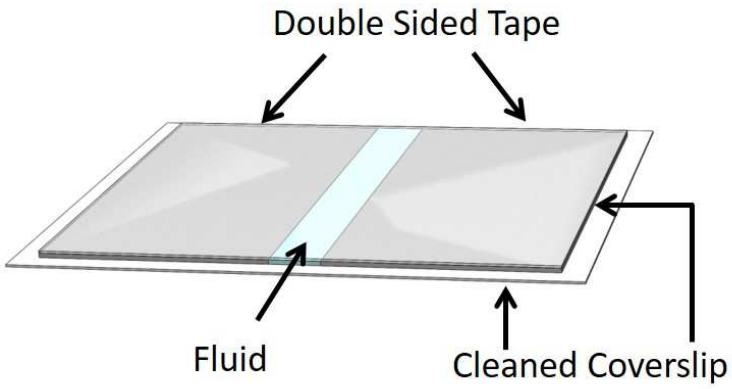

Figure 3.4: Tape channels were assembled using double sided tape to stick two coverslips together creating a channel with a width ∼0.5 cm.

was placed on top forming the top of the channel as illustrated in Fig. 3.4. Coverslips were exploited on the top and bottom of the channel so that the sample could be viewed on an inverted microscope from below and an upright microscope from above. The fluid was introduced into the channel by placing fluid on one side of the channel and pulled through using filter paper.

3.4 Surface Treatments for Reducing Nonspecific Binding

One large challenge, when working with structures near a surface, is reducing non-specific binding and increasing binding of specific proteins or structures of interest to the surface. Using various surface treatments and surfactants, the chemistry of the surface and interactions of molecules with the substrate can be altered to reduce nonspecific binding. Various cleaning techniques in combination with polymer, protein, and detergent blockers were employed in the experiments conducted in this dissertation and are discussed below.

3.4.1 KOH Coverslip Cleaning

Potassium Hydroxide (KOH) was exploited to etch the surface of a coverslip, clean the surface of impurities and reduce nonspecific binding. Initially, KOH (100 g) is dissolved in 100% ethanol (300 mL) and degassed along with another beaker of 100% ethanol (300 mL)

and two beakers of double distilled H_20 (ddH_20) (300 mL). The coverslips were placed in the KOH ethanol solution and sonicated for 5 minutes and then submerged slowly in the 100% ethanol beaker and two ddH_20 beakers. The coverslips were rinsed off with ddH_20 and followed by ethanol. The coverslips were dried with nitrogen and further desiccated in the oven at 65°C for 1 hour. The coverslips were sealed in an airtight container and usable for about one month following the process.

3.4.2 PEG-Biotin Coating

In experiments requiring structure fixation to the surface, mono-functional Poly-ethylene Glycol (m-PEG) and biotin-modified PEG (bio-Peg) was coated on the surface for attachment of streptavidin and reduced nonspecific binding. PEG is a common polymer blocker which blocks non-occupied sites and improves the material's affinity to water. The process involves an initial slide cleaning step using piranha, a silanization step to prepare the surface for adherence of PEG molecules and a pegylation step using PEG and bio-PEG. In a staining jar, sulfuric acid (H_2SO_4 Sigma 320501 - 2.5 L) is mixed with 50% Hydrogen Peroxide (H_2O_2 Sigma 516813 - 500 ML). The coverslips are incubated in the hot, bubbling piranha solution for 1.5 hours preceded by rinsing in ddH_20 through submersion in three beakers of ddH_20. The coverslips are then dried using Nitrogen.

Next, the coverslips are silanized. An unopened bottle of highly purified acetone (Sigma 650501-1 L) is poured over the slides in the staining jar (enough to fully submerge) and mixed on a shaker table for 10 minutes on medium-low so as to swirl vigorously without exposing the slides to air. Then 8 mL of silane (MP biomedicals 215476680) is slowly dripped into the swirling acetone over the course of 1 - 2 minutes to reach a final concentration of about 2%. The reaction is allowed to proceed for 2 more minutes before the coverslips are quickly transferred to a staining jar containing 50% acetone/50% ddH_20 to quench the reaction. The slides are washed by submerging in three beakers of ddH_20 and then dried in the oven at 65°C overnight.

Last, the slides are PEGylated. m-Peg (m-PEG-SVA MW 5,000) and bio-PEG (bio-functional Biotin-PEG-SVA MW 5,000) are mixed together at a mass ratio of 100 m-Peg :

1 bio-Peg in solution with potassium tetraborate buffer ($K_2B_4O_7$ 0.1 M, pH 8.11). bio-PEG and m-Peg solution are placed on one side of a coverslip with an additional coverslip placed on top and squeezed together to spread the solution across the area of the two coverslips. The solution is incubated in between the coverslips for 1 - 1.5 hours before being rinsed off in a beaker of ddH_20. Finally, the slides are dried with nitrogen and stored in a dried airtight container for up to three months following the procedure.

3.4.3 PEG-Silane Treatment

In the previous treatment, biotin molecules were bound to the surface for streptavidin adherence. However, when structure-surface fixation is not necessary, PEG without bio-PEG could be absorbed to the surface to reduce nonspecific binding. Initially, the surface was oxidized using a UV-ozone cleaner for absorption of PEG molecules and then soaked for 30 minutes in 1 mM Peg Silane (mPeg - SIL MW 2,000 Laysan Bio, Inc., lot #114-08) dissolved in ethanol. The surface was then rinsed with ethanol and dried on a hot plat at 110°C for 30 minutes.

3.4.4 Protein Blockers

Additional blocking proteins were utilized to reduce nonspecific binding in most experiments. Both Casein, which is a protein commonly found in mammalian milk, and Bovine Serum Albumin (BSA), a serum albumin protein derived from cows, were used interchangeably. These proteins absorb on the surface and block non-occupied sites [119]. Although they are considered permanent blockers, the protein may occasionally disabsorb. Therefore, additional blocking proteins or blocking detergents are sometimes included in the buffer solution. Generally, casein was incubated in channels at 1 mg/mL for 10 minutes to limit beads sticking to the surface whereas BSA was incubated in channels at 0.1 mg/mL to reduce molecular binding. The proteins were dissolved in the buffers that the samples were suspended in.

3.4.5 Detergent Blockers

Detergents were often included in the buffers to disrupt ionic and hydrophobic biomolecule-surface bonds [119]. Detergent blockers are temporary blockers. If a new buffer was introduced into the channel, the detergent blocker would be removed, unlike the blocking polymers and proteins. The common detergents appropriated in the experiments conducted in this dissertation include NP40 and Tween20. Generally, detergents were added at 0.1 - 0.2% however, in some cases, the detergent was added up to 1%.

3.5 Superparamagnetic Bead Functionalization

3.5.1 Janus Particles

Janus particles (Fig. 3.5) were used in Chapter 4 to study the motion of superparamagnetic particles transported along CoFe zigzag wires. By generating asymmetric particles such that one side was darker (less opaque) than the other side, the orientation of the particle can be readily observed. This was accomplished by placing a thin layer of gold (Au) on one side of the particle. The process involved initially washing carboxyl functionalized beads in isopropyl alcohol (IPA) and then drying with an air gun to create a layer of beads on a silicon wafer. Using an evaporator (Denton DV-502A E-Gun Evaporator) 100 nm of Au is deposited at a rate of 0.3 A/s on the wafer hence coating one side of the particles with Au. Particles are removed by rinsing the wafer with DI. The particles can be concentrated and resuspended in another buffer using the centrifuge to pellet the particles, removing the original buffer and resuspending in a new buffer.

3.5.2 Beads Labeled with Anti-digoxigenin

Beads employed in actuation of DNA origami structures in Chapter 6 and 7 mandated anti-digoxigenin labeling for attachment to DNA structures. Carboxyl coated beads (Dynabeads MyOne^{TM} Carboxylic Acid, Catalog # 65011) were labeled by initially washing and resuspending in 15 mM 2-(Nmorpholino)ethanesulfonic acid (MES) buffer (pH 6.0). Next, the beads were affixed with 1-Ethyl-3-(3-dimethylaminopropyl)carbodiimide (EDC) by incubat-

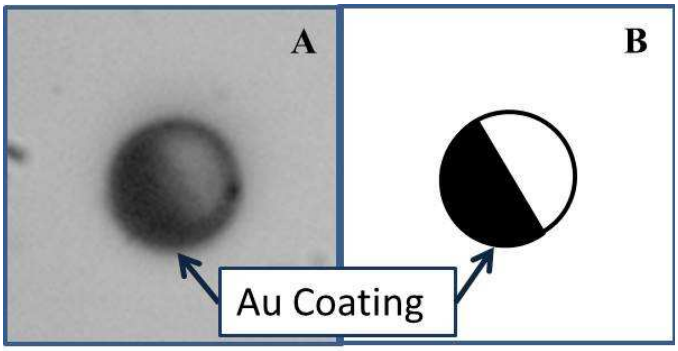

Figure 3.5: Janus particles were made by coating one side with gold (Au) as seen by the darker section on the bead (A) imaged in bright field and (B) illustrated in the schematic.

ing with 10 mg/mL of EDC for 2 hours on a rotisserie followed by a wash step to remove the excess EDC. Then, the beads were incubated on the rotisserie overnight with 2 mg/mL of anti-digoxigenin suspended in 15 mM MES buffer. Last, the excess anti-digoxigenin was removed and resuspended in the desired buffer.

3.6 DNA Structure Purification

DNA origami structures which will be discussed in Chapter 5, 6, and 7 were purified using three different techniques: Gel Electrophoresis Purification, PEG Purification, and Spin Column Purification. While gel purification produces a higher purity, it results in a much lower yield than the other methods. PEG purification generates a much higher yield however can sometimes interfere with structure polymerization. Spin Column Purification also generates a higher yield but requires more resources to purify the same amount of structure.

3.6.1 Gel Electrophoresis Purification

DNA structures are purified by separating excess staples from structures in a gel through the process of electrophoresis. The gel is fabricated by dissolving 2% agarose (Invitrogen, Carlsbad, CA) with 0.5x TAE (buffer containing tris base, acetic acid, and EDTA) through heating the solution in the microwave. $MgCl_2$ is added to the gel to bring the salt concentration to either 4 mM $MgCl_2$ or 11 mM $MgCl_2$. In order to image the DNA structures

under ultraviolet light, 400 ng/ml of ethidium bromide was added to the gel and mixed for 1 - 2 minutes before pouring into the gel tray. To create wells for sample placement, a comb was inserted in the gel before it hardens. A small gel (49.6 g) with 10 wells and a large gel (124 g) with 20 wells were used depending on the sample size. The samples were prepared by mixing 15 μL of folded DNA structures with 3 μL of 6x gel loading dye (New England Biolabs Inc., Ipswich, MA) and 17 μL of the solution were loaded into the wells. Gels were run at 70 V for 2 hours (small) to 3 hours (large) and imaged on a UV illumination table. The bands formed from well-folded DNA structures were cut out and extracted from the gel by centrifuging Freeze′N Squeeze^{TM} gel extraction spin columns (Bio-Rad, Hercules, CA) containing the gel bands for 10 minutes at 10,000 rpm and 4°C. Gel electrophoresis was not only valuable in structure purification but also in structure analysis. Typical images from gel purification and analysis can be viewed in Appendix A.

3.6.2 PEG Purification

Another method for purifying DNA nanostructures used PEG 8000 to separate DNA nanostructures from excess staples which are much smaller. Equal volumes of 15% PEG 8000 with 500 mM NaCl and DNA nanostructures were mixed together in a tube and spun at 16,000 relative centrifugal force (rcf) for 25 minutes at room temperature [120]. The supernatant containing the excess staples was removed leaving behind a small DNA pellet of nanostructures which was not always observable by eye. The structures were then resuspended in the desired buffer to any specific concentration (normally 0.5x TAE with 4 mM $MgCl_2$). Last, structures were incubated at 37°C overnight to further break up the pellet and reduce structure aggregation.

3.6.3 Spin Column Purification

DNA nanostructures could also be purified using Amicon filters through spin column purification (Fig. 3.6). Initially, a 100 kDa Amicon filter membrane is equilibrated by centrifuging 500 μL of the buffer solution through the filter at 5000g for 15 minutes. After the solution is removed, unpurified DNA structures are diluted to 5 nM in 0.4x TAE with 4 mM $MgCl_2$

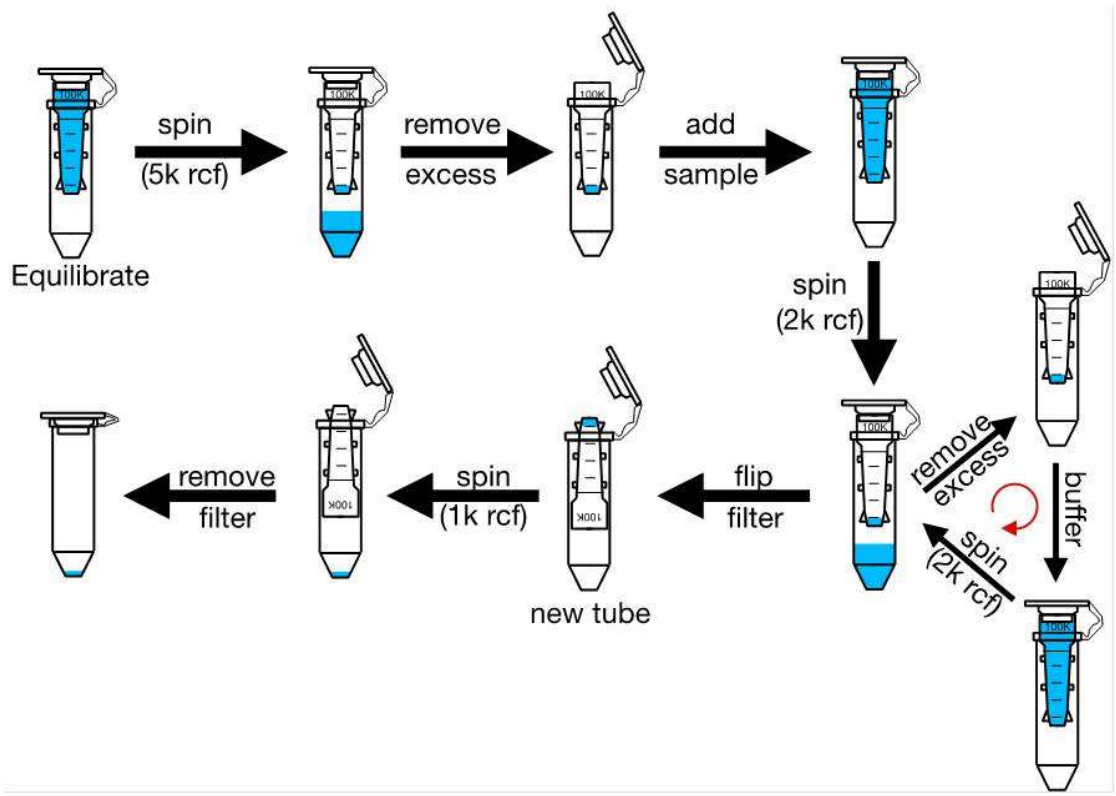

Figure 3.6: DNA structures were purified using spin column purification steps shown in the diagram.

and spun down at 2000g for 30 minutes. The remaining solution at the bottom of the tube, which contains the excess staples, is extracted out. For further staple removal, 500 μL of the buffer can be spun multiple times through the filter at 2000g for 30 minutes. Last, the DNA structures are recovered by reversing the filter tube in a new tube and centrifuging at 1000g for 2 minutes. Around $\sim$ 25 μL of solution should be recovered.

3.7 Imaging Preparation

DNA origami structures which will be discussed in Chapter 5, 6 and 7 were imaged using Atomic Force Microscopy (AFM), Transmission Electron Microscopy (TEM) and in real-time using Total Internal Reflection Fluorescence (TIRF) Microscopy. In each case, the samples had to be initially prepared for imaging using any of these technique. These

preparations are discussed below.

3.7.1 AFM Imaging

Nanostructures were imaged using a Bruker AXS Dimension Icon AFM (Bruker, Billerica, MA). DNA nanostructures were fixed onto a 12 mm Mica Discs (Ted Pella, Inc., Redding, CA). By removing a strip of double-sided tape adhered to the mica substrate, a mono layer of mica was formed. Next, 5 μL of structures at 1 nM were incubated on the mica substrate for 2 minutes and washed off with 1 mL of ddH_20. The substrate was quickly dried using an air gun and filter paper. The structures were imaged on the AFM in Scanasyst Air mode.

3.7.2 TEM Imaging

In order to image the DNA origami structures on TEM the following steps were initially taken to prepare the sample for imaging. First, stock solutions of 2% Uranyl-Formate (UFo) stain solution with 25 mM NaOH. 5 ml of UFo (SPI-Chem - 16984-59-1) was dissolved in boiled de-oxygenated ddH_20 by vortex vigorously and then was filtered through the 0.2 μm syringe filter (Fisher - SLGP033RS). Aliquotes were made of the solution, covered in aluminum foil to reduce exposure to light and stored in -20°C freezer for later use up to two months. When using the UFo aliquoted solution for staining, 5 M NaOH was added to the thawed UFo solution and vortexed for 2 minutes before centrifuging at top speeds for 3 minutes. Second, samples were deposited on the substrate and stained. TEM grids (Electron Microscopy Sciences - FCF400-Cu-50) were initially exposed to oxygen plasma for 30 seconds to create a hydrophilic surface for structure attachment. 3 μL of sample were deposited on the grid for $\sim$4 minutes. Drops of UFo staining solution were placed on the sample in the last minute of incubation. The excess fluid was absorbed off the edge of the grid using filter paper (Fisher 1004070) and the grid sample was immersed in 10 μL drop of UFo staining solution. The solution is then dabbed off the grid with filter paper followed by a second immersion in a 20 μL drop of UFo staining solution and 40 second incubation with the staining side faced down. Excess UFo staining solution is removed using filter paper and is air-dried for 15 minutes before being imaged.

3.7.3 TIRF Imaging

For real-time imaging, DNA structures were imaged using TIRF on an inverted microscope (Nikon Eclipse Ti). To visualize the structures, fluorophores were attached via single-stranded DNA (ssDNA) overhangs. If the structures were in a tape channel, 6 μL of conjugated ssDNA with fluorophores at 10 nM were flown into the channel and incubated for 4 minutes. Several 20 μL of buffer was flowed through the channel afterward to remove excess fluorophores. Structures were also confined to 2D surfaces by placing 0.5 μL - 1 μL of structure between 2 coverslips. To reduce attachment of structures to coverslips, 1 mg/mL of casein was first incubated between the slides for 10 minutes, washed off with ddH_20 and then dried. If the structures did not have fluorophores already attached, 0.5 μL of conjugated ssDNA with fluorophores at 10 nM was incubated with 1 μL of structure before placement between coverslips.

Chapter 4
Energy Landscape of Patterned Magnetic Traps

Thin magnetic patterns used to create mobile magnetic traps as discussed in Chapter 2 were studied by exploring their energy landscape using superparamagnetic beads as the probe. In order to fully utilize the capabilities of these mobile magnetic traps, it is vital to understand the changes in energy landscape due to external fields and bead sizes, the trapping locations of the bead and the forces acting on the bead. As discussed in Chapter 8, these mobile magnetic traps transport beads labeled with *E. coli* to targeted locations for applications in protein lithography. Additionally, the thin magnetic patterns could be incorporated into actuating and confining DNA origami structures as discussed in the future work in Chapter 9. The energy landscape of $Co_{0.5}Fe_{0.5}$ wires and permalloy (NiFe) disks (5 μm and 30 μm diameter) were studied. The theoretical models (Chapter 2) of the energy landscape and forces were compared with the experimental forces measured from the spatial and temporal coordinates of beads transported from vertex to vertex on the wires and displaced off the disks visualized using a high-speed camera (Phantom Miro M120, Vision Research).

4.1 Permalloy Disks

In displacing a superparamagnetic (SPM) bead off a permalloy disk, the in-plane ($\mathbf{H}_{XY}$) and out-of-plane fields ($\mathbf{H}_Z$) are tuned. Since permalloy is a relatively soft ferromagnetic material, disks become magnetized in the direction of weak in-plane external fields. The mobile domain wall on the perimeter of the disk produces stray fields $\mathbf{H}_{DW}$ and can be

circumferential rotated around the disk by precessing $\mathbf{H}_{XY}$. The induced moment in a SPM bead located at a given height above the disks is determined by the net field, $\mathbf{H}_{ext} + \mathbf{H}_{DW}$. In an applied external field ($\mathbf{H}_{ext}$), the SPM will become trapped on the perimeter of the disk at the domain wall. By reversing $\mathbf{H}_Z$, the SPM will be repelled from the trap off the disk. When $\mathbf{H}_{XY} < \mathbf{H}_Z$, the bead will be forced away from the disk, however when $\mathbf{H}_{XY} > \mathbf{H}_Z$, a secondary trap is formed slightly off the outer edge of the disk and the bead remains trapped near the disk edge. Two sizes of disks with a diameter of 5 μm and 30 μm were studied using a bead of diameter 2.8 μm and 8.8 μm under two field comparisons: $\mathbf{H}_{XY}$ = 30/80 Oe, $\mathbf{H}_Z$ = 80/30 Oe and $\mathbf{H}_{XY}$ = 80/120 Oe, $\mathbf{H}_Z$ = 120/80 Oe.

4.1.1 Probing the Energy Landscape of Permalloy Disks with 5 μm Diameter

Permalloy disks with 5 μm diameters (50 nm thick) were initially studied by displacing superparamagnetic beads with diameters of 2.8 μm (Dynabeads cat. no. 14305D) off the disk. Fig. 4.1 compares the energy landscape and forces on the SPM bead when $\mathbf{H}_{XY}$ = 30 Oe, $\mathbf{H}_Z = \pm$80 Oe and when $\mathbf{H}_{XY}$ = 80 Oe, $\mathbf{H}_Z = \pm$30 Oe. In Fig. 4.1A, the out-of-plane field ($\mathbf{H}_Z$) is reversed from +80 to −80 Oe while the in-plane field remains at $\mathbf{H}_{XY}$ = 30 Oe. For $\mathbf{H}_Z$ = +80 Oe (dashed curve), the particle (dark circle) sits in a potential minimum near the perimeter of the disk. When $\mathbf{H}_Z$ is reversed to −80 Oe (solid curve), this trap becomes repulsive and the bead moves steadily from this unfavorable energy state away from the disk to lower energy levels until it slows to a stop. When $|\mathbf{H}_{XY}| > |\mathbf{H}_Z|$, as in Fig. 4.1B ($\mathbf{H}_{XY}$ = 80 Oe, $|\mathbf{H}_Z| = \pm$30 Oe), a secondary trap near the disk perimeter results such that the bead is trapped quickly after $\mathbf{H}_Z$ is reversed to −30 Oe. As demonstrated in Fig. 4.1C, when $|\mathbf{H}_{XY}| < |\mathbf{H}_Z|$, the bead moves much farther (∼5 μm) than when $|\mathbf{H}_{XY}| > |\mathbf{H}_Z|$ where the bead is abruptly trapped (∼1 μm) which are in agreement with the energy landscape as seen in Fig. 4.1A and B. The peak magnetic forces repelling the bead off the disk were experimentally calculated from spatial and temporal coordinates of the bead to be 12 and 9 pN (Section 4.2.4). The initial trapping location relative to the disk edge as displayed by the energy landscape in Fig. 4.1D agrees with the experimentally

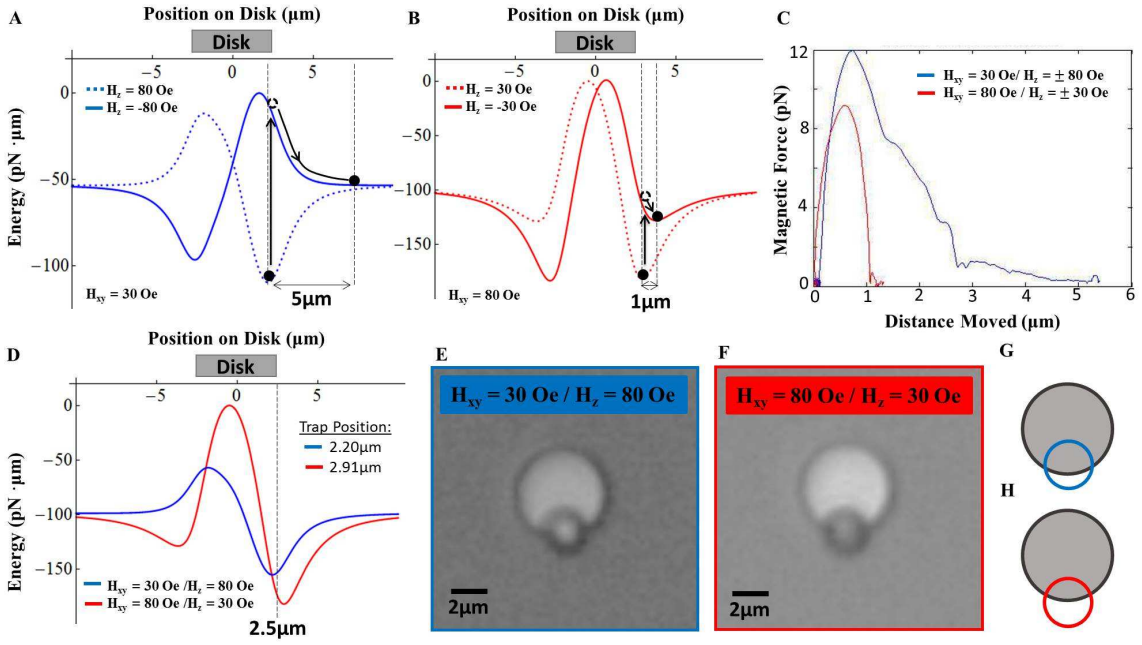

Figure 4.1: Potential energy landscapes for a 2.8 μm bead on a 5 μm disk in (A) $\mathbf{H}_Z = \pm 80$ Oe and $\mathbf{H}_{XY} = 30$ Oe. (B) $\mathbf{H}_Z = \pm 30$ Oe and $\mathbf{H}_{XY} = 80$ Oe. (C) Experimentally measured magnetic forces on the same bead displaced off the 5 μm disk corresponding to the potential energy landscapes in A (blue) and in B (red). (E) The bright-field image of the initial position of the bead corresponding to the blue energy landscape in D. (F) The bright-field image of the initial position of the bead corresponding to the red energy landscape in D. (G,H) The schematic of the bright-field images of E and F, respectively, displays the shift of the bead (G, blue and H, red) on the disk (gray).

verified starting locations of the bead shown in the bright-field images in Fig. 4.1E and F and the corresponding schematic images in Fig. 4.1G and H. When $|\mathbf{H}_{XY}| < |\mathbf{H}_Z|$, the bead is trapped inside the perimeter of the disk whereas when $|\mathbf{H}_{XY}| > |\mathbf{H}_Z|$, it is trapped outside of the perimeter (Fig. 4.1E and F). Due to the translucent nature of the bead, a lighter center is visualized when the bead is located on the disk since more light is reflected.

In Fig. 4.2A, the out-of-plane field ($\mathbf{H}_Z$) is reversed from +120 to −120 Oe while the in-plane field remains at $\mathbf{H}_{XY} = 80$ Oe. For $\mathbf{H}_Z = +120$ Oe (dashed curve), the particle (dark circle) sits in a potential minimum near the perimeter of the disk. When $\mathbf{H}_Z$ is reversed to −120 Oe (solid curve), this trap becomes repulsive and the bead moves steadily

from this unfavorable energy state away from the disk to lower energy levels until it slows to a stop. When $|\mathbf{H}_{XY}| > |\mathbf{H}_Z|$, as in Fig. 4.2B ($\mathbf{H}_{XY}$ = 120 Oe, $|\mathbf{H}_Z| = \pm 80$ Oe), a secondary trap near the disk perimeter results such that the bead is trapped quickly after $\mathbf{H}_Z$ is reversed to −80 Oe. As shown in Fig. 4.2C, when $|\mathbf{H}_{XY}| < |\mathbf{H}_Z|$, the bead moves much farther (∼5 μm) than when $|\mathbf{H}_{XY}| > |\mathbf{H}_Z|$ where the bead is quickly slowed down and trapped (∼1.5 μm) which are in agreement with the energy landscape as seen in Fig. 4.2A and B. The peak magnetic forces repelling the bead off the disk were experimentally calculated from spatial and temporal coordinates of the bead to be 12 and 9 pN (Section 4.2.4). The initial trapping location relative to the disk edge as displayed by the energy landscape in Fig. 4.2D agrees with the experimentally verified starting locations of the bead shown in the bright-field images in Fig. 4.2E and F and the schematic images in Fig. 4.2G and H. When $|\mathbf{H}_{XY}| < |\mathbf{H}_Z|$, the bead is trapped inside the perimeter of the disk whereas when $|\mathbf{H}_{XY}| > |\mathbf{H}_Z|$, it is trapped outside of the perimeter. In this case, the difference between the bead starting location is much smaller than when the fields are $\mathbf{H}_{XY}$ = 30/80 Oe, $\mathbf{H}_Z$ = 80/30 Oe.

4.1.2 Probing the Energy Landscape of Permalloy Disks with 30 μm Diameter

Permalloy disks with 30 μm diameters (60 nm thick) were initially studied by displacing superparamagnetic beads with diameters of 8.8 μm (Spherotech cat. no. CM-80-10) off the disk. Fig. 4.3 compares the energy landscape and forces on the SPM bead when $\mathbf{H}_{XY}$ = 30 Oe, $\mathbf{H}_Z = \pm 80$ Oe and when $\mathbf{H}_{XY}$ = 80 Oe, $\mathbf{H}_Z = \pm 30$ Oe. In Fig. 4.3A, the out-of-plane field ($\mathbf{H}_Z$) is reversed from +80 to −80 Oe while the in-plane field remains at $\mathbf{H}_{XY}$ = 30 Oe. For $\mathbf{H}_Z$ = +80 Oe (dashed curve), the particle (dark circle) sits in a potential minimum near the perimeter of the disk. When $\mathbf{H}_Z$ is reversed to −80 Oe (solid curve), this trap becomes repulsive and the bead moves steadily from this unfavorable energy state away from the disk to lower energy levels until it slows to a stop. When $|\mathbf{H}_{XY}| > |\mathbf{H}_Z|$, as in Fig. 4.3B ($\mathbf{H}_{XY}$ = 80 Oe, $|\mathbf{H}_Z| = \pm 30$ Oe), a secondary trap near the disk perimeter results such that the bead is trapped quickly after $\mathbf{H}_Z$ is reversed to −30 Oe. As shown

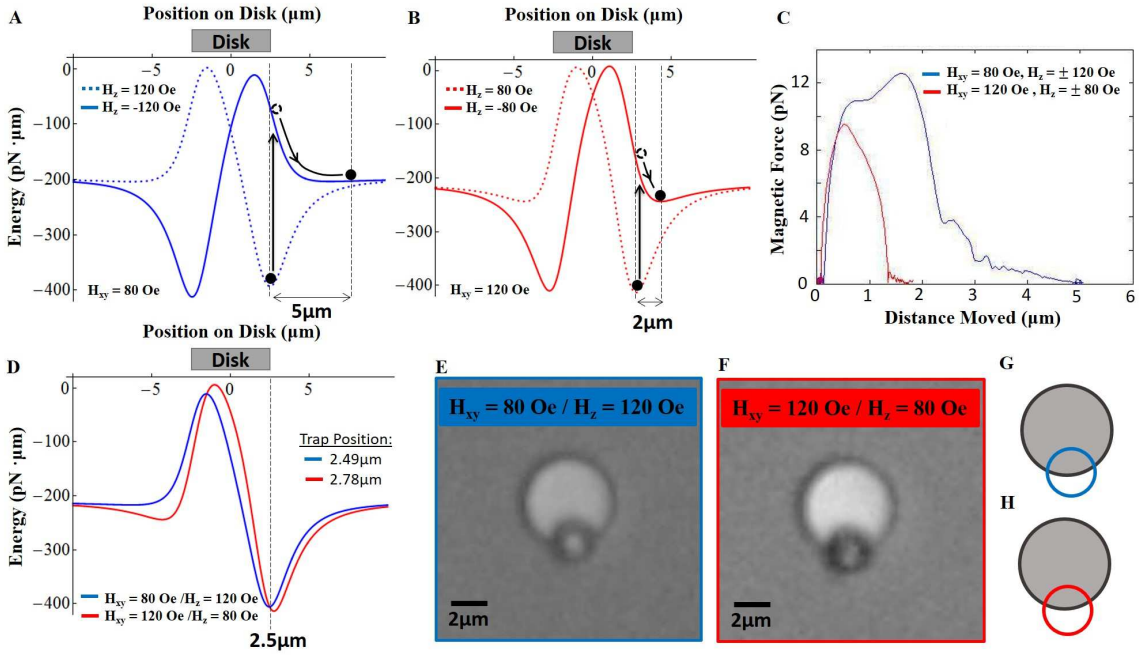

Figure 4.2: Potential energy landscapes for a 2.8 μm bead on a 5 μm disk in (A) $\mathbf{H}_Z = \pm 120$ Oe and $\mathbf{H}_{XY} = 80$ Oe. (B) $\mathbf{H}_Z = \pm 80$ Oe and $\mathbf{H}_{XY} = 120$ Oe. (C) Experimentally measured magnetic forces on the same bead displaced off the 5 μm disk corresponding to the potential energy landscapes in A (blue) and in B (red). (E) The bright-field image of the initial position of the bead corresponding to the blue energy landscape in D. (F) The bright-field image of the initial position of the bead corresponding to the red energy landscape in D. (G,H) The schematic of the bright-field images of E and F, respectively, displays the shift of the bead (G, blue and H, red) on the disk (gray).

in Fig. 4.3C, when $\mid \mathbf{H}_{XY} \mid < \mid \mathbf{H}_Z \mid$, the bead moves much farther ($\sim$8 μm) than when $\mid \mathbf{H}_{XY} \mid > \mid \mathbf{H}_Z \mid$ where the bead is abruptly trapped ($\sim 2\mu$m) in agreement with the energy landscape as seen in Fig. 4.3A and B. The peak magnetic forces repelling the bead off the disk were experimentally calculated from spatial and temporal coordinates of the bead to be 60 and 15 pN (Section 4.2.4). The initial trapping location relative to the disk edge as displayed by the energy landscape in Fig. 4.3D is similar to the experimentally verified starting location of the bead shown in the bright-field images in Fig. 4.3E and F and the schematic images in Fig. 4.3G and H. When $\mid \mathbf{H}_{XY} \mid < \mid \mathbf{H}_Z \mid$, the bead is trapped inside the perimeter of the disk whereas when $\mid \mathbf{H}_{XY} \mid > \mid \mathbf{H}_Z \mid$, it is trapped outside of the perimeter (Fig. 4.3E and F). Due to the translucent nature of the bead, a lighter center is

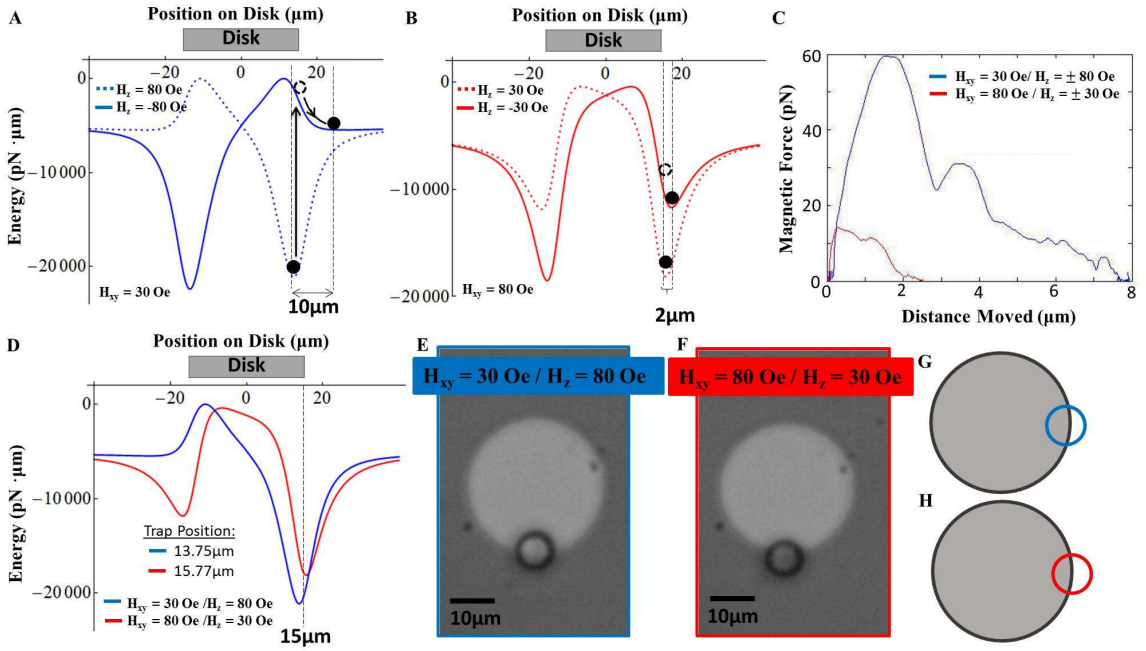

Figure 4.3: Potential energy landscapes for an 8.8 μm bead on a 30 μm disk in (A) $\mathbf{H}_Z = \pm 80$ Oe and $\mathbf{H}_{XY} = 30$ Oe. (B) $\mathbf{H}_Z = \pm 30$ Oe and $\mathbf{H}_{XY} = 80$ Oe. (C) Experimentally measured magnetic forces on the same bead displaced off the 30 μm disk corresponding to the potential energy landscapes in A (blue) and in B (red). (E) The bright-field image of the initial position of the bead corresponding to the blue energy landscape in D. (F) The bright-field image of the initial position of the bead corresponding to the red energy landscape in D. (G,H) The schematic of the bright-field images of E and F, respectively, displays the shift of the bead (G, blue and H, red) on the disk (gray).

visualized when the bead is located on the disk since more light is reflected.

In Fig. 4.4A, the out-of-plane field ($\mathbf{H}_Z$) is reversed from +120 to −120 Oe while the in-plane field remains at $\mathbf{H}_{XY} = 80$ Oe. For $\mathbf{H}_Z = +120$ Oe (dashed curve), the particle (dark circle) sits in a potential minimum near the perimeter of the disk. When $\mathbf{H}_Z$ is reversed to −120 Oe (solid curve), this trap becomes repulsive and the bead moves steadily from this unfavorable energy state away from the disk to lower energy levels until it slows to a stop. When $|\mathbf{H}_{XY}| > |\mathbf{H}_Z|$, as in Fig. 4.4B ($\mathbf{H}_{XY} = 120$ Oe, $|\mathbf{H}_Z| = \pm 80$ Oe), a secondary trap near the disk perimeter results such that the bead is trapped quickly after $\mathbf{H}_Z$ is reversed to −80 Oe. As shown in Fig. 4.4C, when $|\mathbf{H}_{XY}| < |\mathbf{H}_Z|$, the bead moves much farther (∼7 μm) than when $|\mathbf{H}_{XY}| > |\mathbf{H}_Z|$ where the bead is quickly slowed down

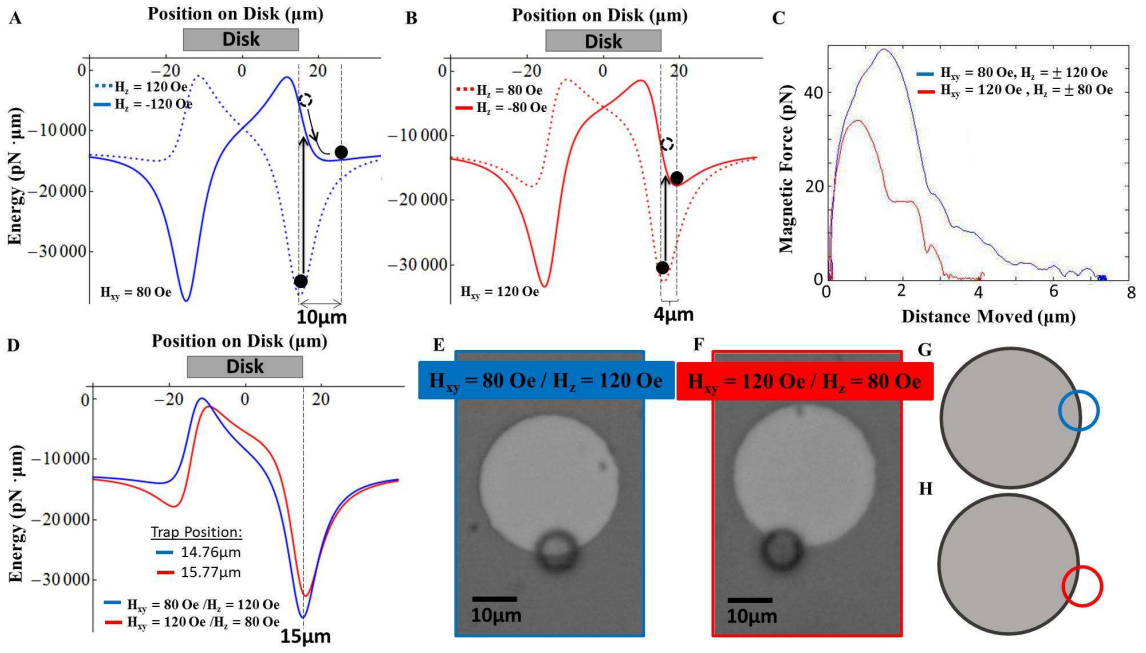

Figure 4.4: Potential energy landscapes for an 8.8 μm bead on a 30 μm disk in (A) $\mathbf{H}_Z = \pm 120$ Oe and $\mathbf{H}_{XY} = 80$ Oe. (B) $\mathbf{H}_Z = \pm 80$ Oe and $\mathbf{H}_{XY} = 120$ Oe. (C) Experimentally measured magnetic forces on the same bead displaced off the 30 μm disk corresponding to the potential energy landscapes in A (blue) and in B (red). (E) The bright-field image of the initial position of the bead corresponding to the blue energy landscape in D. (F) The bright-field image of the initial position of the bead corresponding to the red energy landscape in D. (G,H) The schematic of the bright-field images of E and F, respectively, displays the shift of the bead (G, blue and H, red) on the disk (gray).

and trapped ($\sim$4 μm) in agreement with the energy landscape seen in Fig. 4.4A and B. The peak magnetic forces repelling the bead off the disk were experimentally calculated from spatial and temporal coordinates of the bead to be 50 and 35 pN (Section 4.2.4). The initial trapping location relative to the disk edge as displayed by the energy landscape in Fig. 4.4D stands in agreement with the experimentally verified starting locations of the bead shown in the bright-field images in Fig. 4.4E and F and the schematic images in Fig. 4.4G and H. When $|\mathbf{H}_{XY}| < |\mathbf{H}_Z|$, the bead is trapped inside the perimeter of the disk whereas when $|\mathbf{H}_{XY}| > |\mathbf{H}_Z|$, it is trapped outside of the perimeter. In this case, the difference between the bead locations is much smaller in the cases when the fields are $\mathbf{H}_{XY}$ = 30/80 Oe, $\mathbf{H}_Z$ = 80/30 Oe.

4.2 CoFe Zigzag Wires

Similar analysis was done for the CoFe zigzag wires in which these results were published [96] and further discussed in Howdyshell's dissertation [99]. These findings have been included for completeness. In transporting a SPM bead from one vertex to an adjacent vertex, the in-plane ($\mathbf{H}_{XY}$) and out-of-plane fields ($\mathbf{H}_{Z}$) are tuned. These weak fields do not modify the general location of the domain walls in the zigzag wires in any significant way [91] and thus the associated domain wall fields ($\mathbf{H}_{DW}$) are determined solely by the CoFe wire dimensions and initial magnetization. The moment induced in a SPM bead located at a given height above the wires is determined by the net field, $\mathbf{H}_{ext} + \mathbf{H}_{DW}$. In the absence of $\mathbf{H}_{ext}$, adjacent vertices and their associated $\mathbf{H}_{DW}$ act as primary trapping sites for the bead. With increasing $\mathbf{H}_{Z}$, the bead induced moment is proportionally determined by $\mathbf{H}_{ext}$ and the energy landscapes of adjacent HH and TT vertices, which steadily transform to become attractive and repulsive, respectively as seen in Fig. 4.5. The introduction of $\mathbf{H}_{XY}$ in the presence of $\mathbf{H}_{Z}$, with $\mathbf{H}_{XY}$ oriented along the straight segment of the zigzag wire, further transforms the character and location of the traps. In particular, the primary traps weaken and shift away from the zigzag vertex to positions that lie between vertices. The resulting secondary traps (S_i) are crucial to the transport of the beads, which, depending on the depth of the trapping potential, can be slowed down, momentarily stalled, or completely halted in their movement between vertices. These features are highlighted in Figs. 4.6, 4.7 and 4.8 for beads (diameters 2.8 μm and 11 μm) of different magnetic susceptibilities.

4.2.1 Probing the Energy Landscape with 2.8 μm Beads

The CoFe zigzag wires (14.5 μm long, 1 μm wide and 12 nm thick) were initially studied by transporting superparamagnetic beads with diameters of 2.8 μm (Dynabeads cat. no. 14305D) from one vertex to another. The Dynabeads have a very narrow size distribution that ranged in diameter between $\pm$1.4% of the mean diameter of 2.8 μm [111, 121]. Fig. 4.6 shows the influence of $\mathbf{H}_{XY}$ and $\mathbf{H}_{Z}$ on the energy landscape during transport of a 2.8 μm diameter bead along the wire between adjacent vertices. In Fig. 4.6A, the out-of-plane

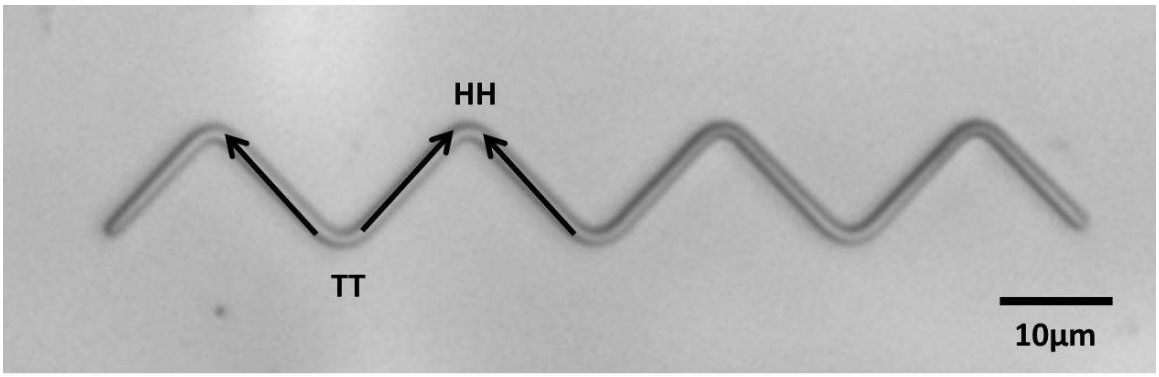

Figure 4.5: CoFe zigzag wires are magnetized with a large in-plane field of 1 T in which the magnetization relaxes to lie along the direction of the wire after removing the external field creating head-to-head (HH) and tail-to-tail (TT) domain walls.

field ($\mathbf{H}_Z$) is reversed from +40 to −40 Oe while the in-plane field $\mathbf{H}_{XY}$ = 10 Oe. For $\mathbf{H}_Z$ = +40 Oe (dashed curve), the particle (dark circle) sits in a potential minimum (initial trap S_0) near the first vertex.

When $\mathbf{H}_Z$ is reversed to −40 Oe (solid curve), this vertex becomes repulsive and, since no intermediate traps are stabilized between the vertices, the particle moves steadily from this unfavorable energy state toward the neighboring final trap (S_f) located at the other vertex. When $\mid \mathbf{H}_{XY} \mid > \mid \mathbf{H}_Z \mid$, as in Fig. 4.6B ($\mathbf{H}_{XY}$ = 80 Oe, $\mid \mathbf{H}_Z \mid$ = 40 Oe), two secondary traps of different energy depths occur. The intermediate trap (S_i) nearer to the initial vertex is weakened by the repulsive contribution of $\mathbf{H}_Z$ to the potential energy while the constructive superposition of $\mathbf{H}_Z$ and $\mathbf{H}_{DW}$ at the second vertex renders a deeper secondary trap (S_f). For a given $\mid \mathbf{H}_Z \mid$, the intermediate trap S_i steadily becomes more pronounced with increasing $\mathbf{H}_{XY}$ and S_i transforms from a weak shoulder to a distinct trap that slows the particle's motion. For weak planar fields ($\mid \mathbf{H}_{XY} \mid \leq \mid \mathbf{H}_Z \mid$), $\mathbf{H}_{XY}$ is not strong enough to effectively influence the orientation of the bead's induced magnetic moment to generate a clear intermediate trap, as shown in Fig. 4.6C and D, where $\mathbf{H}_{XY}$ = 10 Oe and $\mid \mathbf{H}_Z \mid$ = 10 and 80 Oe, respectively.

As shown in Fig.4.7, the energy profiles presented in Fig. 4.6 are consistent with the measured speeds of the bead. Fig. 4.7A confirms that for low $\mathbf{H}_{XY}$ (10 Oe) and $\mathbf{H}_Z$ (40

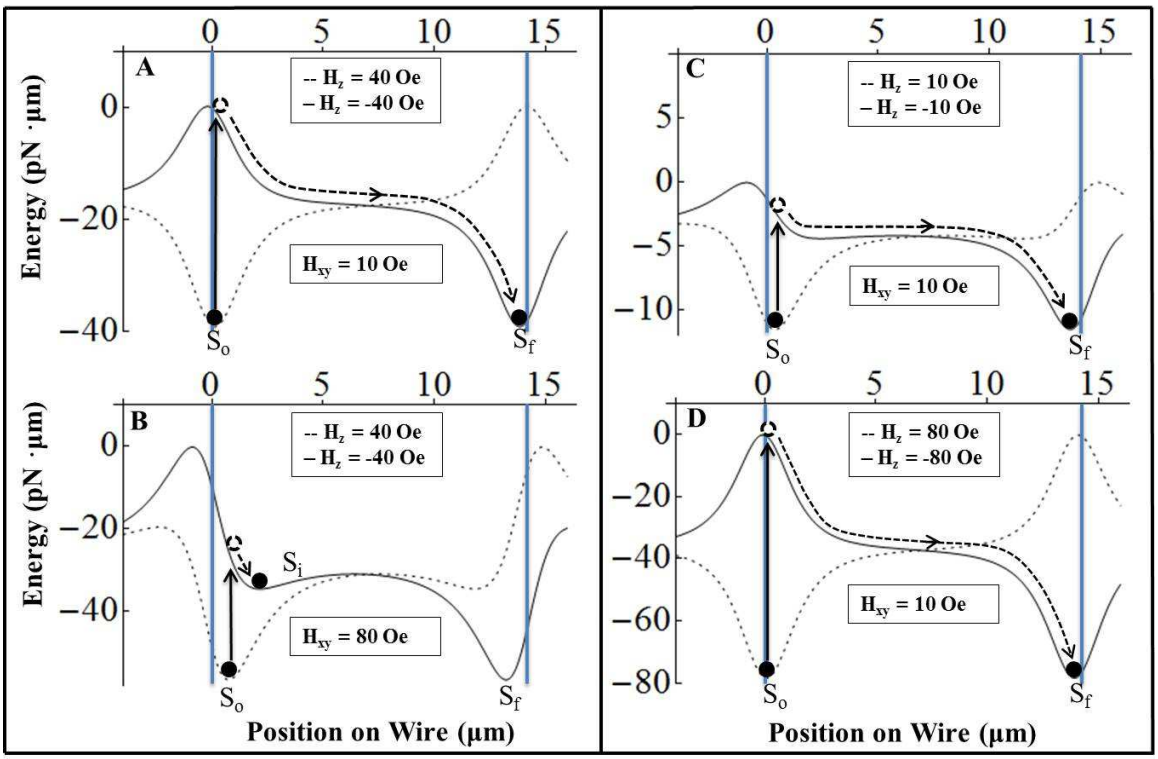

Figure 4.6: Potential energy landscapes for a 2.8 μm bead on a wire in (A) $\mathbf{H}_Z = \pm 40$ Oe and $\mathbf{H}_{XY} = 10$ Oe. (B) $\mathbf{H}_Z = \pm 40$ Oe and $\mathbf{H}_{XY} = 80$ Oe. (C) $\mathbf{H}_Z = \pm 10$ Oe and $\mathbf{H}_{XY} = 10$ Oe. (D) $\mathbf{H}_Z = \pm 80$ Oe and $\mathbf{H}_{XY} = 10$ Oe. In the presence of a positive $\mathbf{H}_Z$ field, the initial position of the bead (expected position indicated by a dark circle) is at the initial trap S_0. $\mathbf{H}_Z$ is then reversed, causing the bead to move to the lower energy at S_f. The movement of the bead along the energy profile is indicated by arrows. S_0, S_i, and S_f indicate initial, intermediate, and final traps. Vertical lines (blue) indicate locations of wire vertices. The largest deviation of S_i and S_f from the vertices occurs at large $\mathbf{H}_{XY}$ values ($\mid \mathbf{H}_{XY} \mid > \mid \mathbf{H}_Z \mid$).

Oe), the bead initially accelerates reaching speeds ~60 μm/s as it moves away from the initial trap (S_0), which is transformed into a repulsive site by reversing $\mathbf{H}_Z$. The motion is then slowed as the bead encounters a flatter energy landscape before emerging and gaining speed as it moves toward the deeper final trap (S_f) where it is rapidly brought to rest. In Fig. 4.7B, $\mathbf{H}_{XY} = 70$ Oe ($\mid \mathbf{H}_{XY} \mid > \mid \mathbf{H}_Z \mid$) and an intermediate trap causes the particle to be temporarily localized before eventually escaping from S_i to reach target destination S_f. For $\mathbf{H}_{XY} = 80$ Oe (Fig. 4.7C), however, the intermediate trap is sufficiently deep that the particle is, as expected, permanently halted well before reaching the adjacent vertex. Fig.

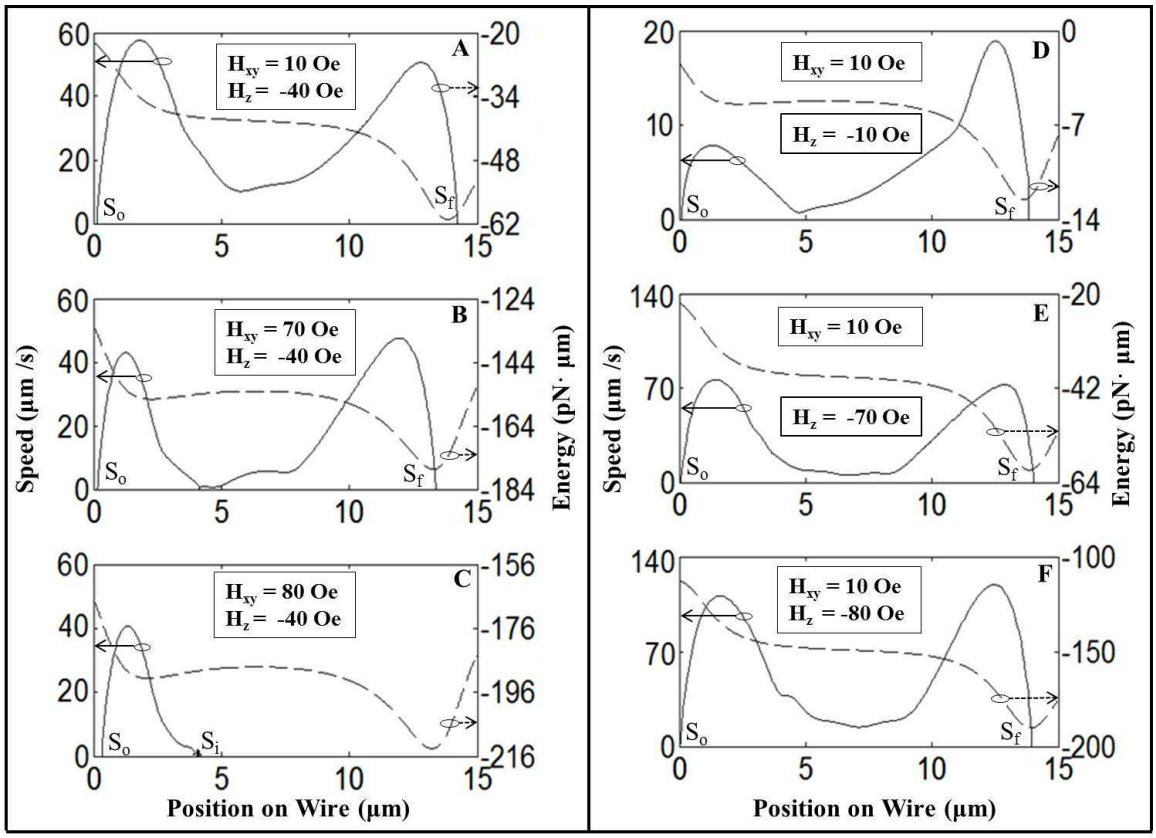

Figure 4.7: Experimentally measured speed of 2.8 μm bead moving along the wire (solid lines) and corresponding potential energies (dashed lines) calculated from the model. Plots are for $\mathbf{H}_Z = -40$ Oe and $\mathbf{H}_{XY}$ = (A) 10, (B) 70, and (C) 80 Oe. As $\mathbf{H}_{XY}$ increases, an intermediate secondary trap S_i emerges, causing the bead (B) to slow or (C) come to rest. Experiments on the same bead with $\mathbf{H}_{XY} = 10$ Oe and $\mathbf{H}_Z$ = (D) -10, (E) -70, and (F) -80 Oe do not result in intermediate traps and the bead reaches the destination vertex.

4.7D-F demonstrates experimental confirmation that when $|\mathbf{H}_{XY}| < |\mathbf{H}_Z|$, intermediate traps do not form thereby enabling the particle to reach the next vertex.

4.2.2 Probing the Energy Landscape with 11 μm Beads

CoFe wires with the same dimensions were probed with a SPM bead that had a diameter of 11 μm (Spherotech cat. no. CM-80-10). The beads from Spherotech normally had a much wider distribution with diameters on average ranging from 8.0 to 9.9 μm. A single bead of 11 μm in diameter was used in all the experiments presented in this section to

reduce variation in the experimental results since the magnetic content and susceptibility vary from bead to bead. The 11 μm SPM bead offer different responses compared with their 2.8 μm counterpart. These changes can be traced to the effective bead moment above the vertex. Despite having larger expected susceptibilities (which increases the magnetic potential energy), the 11 μm beads experience weaker effective fields and broader primary traps due to the large field gradients associated with $\mathbf{H}_{DW}$. The initial (S_{01}, S_{02}) and final (S_{f1} and S_{f2}) traps are located along the wire a few micrometers from the vertex center; this distance increases with increasing $\mathbf{H}_{XY}$. On 14.5 μm long wires, the broadened primary traps approach each other with no intermediate traps evident (Fig. 4.8A-D). According to the model, for wires $\sim$40 μm and longer, the initial and final traps are more separated (not shown), enabling an intermediate trap to emerge for the 11 μm sized particles. The experimental results of Fig. 4.8E and F for the 11 μm particles confirm that the corresponding translational speeds are smaller than those on the 2.8 μm particles. The smaller measured speeds and reductions in the distance traveled along the wire with increasing $\mathbf{H}_{XY}$ are in line with the model. Confirmation of theoretical predictions (Fig. 4.6 Fig. 4.8) of the measured starting and ending locations, as well as recorded changes in particle speed with applied fields for the different particles thus validates the models related to: 1) domain-wall generated fields ($\mathbf{H}_{DW}$); 2) response of the energy landscape to $\mathbf{H}_{XY}$ + $\mathbf{H}_{Z}$; and 3) the magnetic properties of the beads.

4.2.3 Rotational and Translational Motion of Beads observed using Janus Particles

We have also observed (Fig. 4.9) that the 11 μm Janus particles exhibit an initial rolling motion prior to sliding along the wire. Upon reversing $\mathbf{H}_{Z}$, (Fig. 4.9A, iviii), the entire bead is observed to rotate to align with the net field prior to sliding along the wire to reach the neighboring vertex while maintaining its orientation (Fig. 4.9B, iviii). These findings reveal a field-induced rotational torque on the microparticle immediately after the field is reversed. This, in turn, suggests the presence of a small permanent characteristic due to larger nanoparticles with slower relaxation times embedded in the bead or easy axis char-

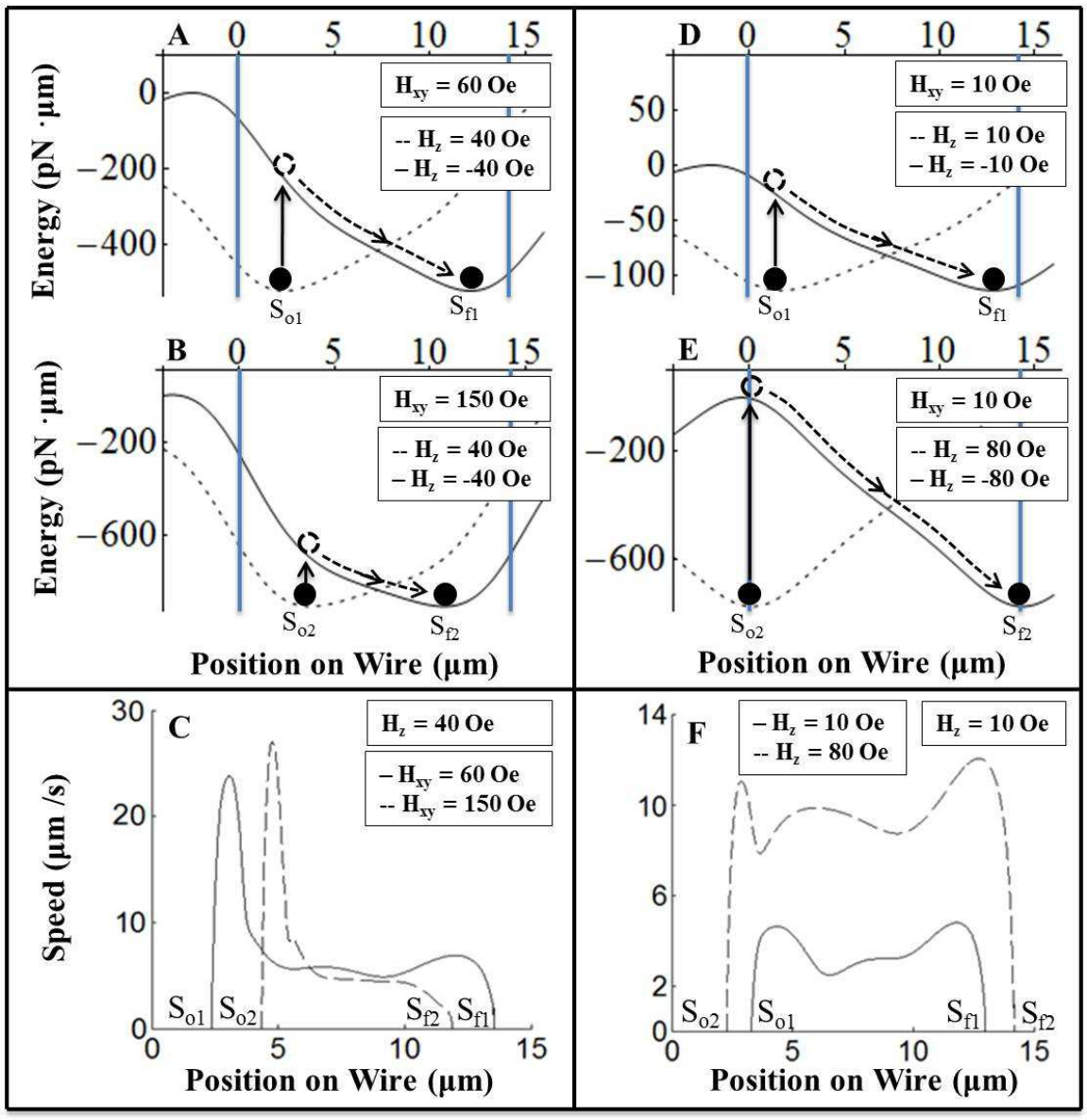

Figure 4.8: Experimentally measured speed of the 11 μm bead along the wire and corresponding potential energy landscape calculated from the model. (A) and (B) Potential energy in elds $\mathbf{H}_Z = \pm 40$ Oe and $\mathbf{H}_{XY} = 60$ and 150 Oe, respectively. (C) and (D) Potential energy for $\mathbf{H}_{XY} = 10$ Oe and $\mathbf{H}_Z = \pm 10$ and ± 80 Oe, respectively. Vertical lines (blue) indicate locations of wire vertices. (E) Experimentally determined particle speed in $\mathbf{H}_Z = -40$ Oe and $\mathbf{H}_{XY} = 60$ and 150 Oe. (F) Measured particle speed for $\mathbf{H}_{XY} = 10$ Oe and $\mathbf{H}_Z = -10$ and -80 Oe. As $\mathbf{H}_Z$ increases relative to $\mathbf{H}_{XY}$ secondary traps shift closer to wire vertex and, as predicted in (A)(D), the particle travels a larger distance. S_{01}, S_{02}, S_{f1}, and S_{f2} are the initial and final traps for different field values.

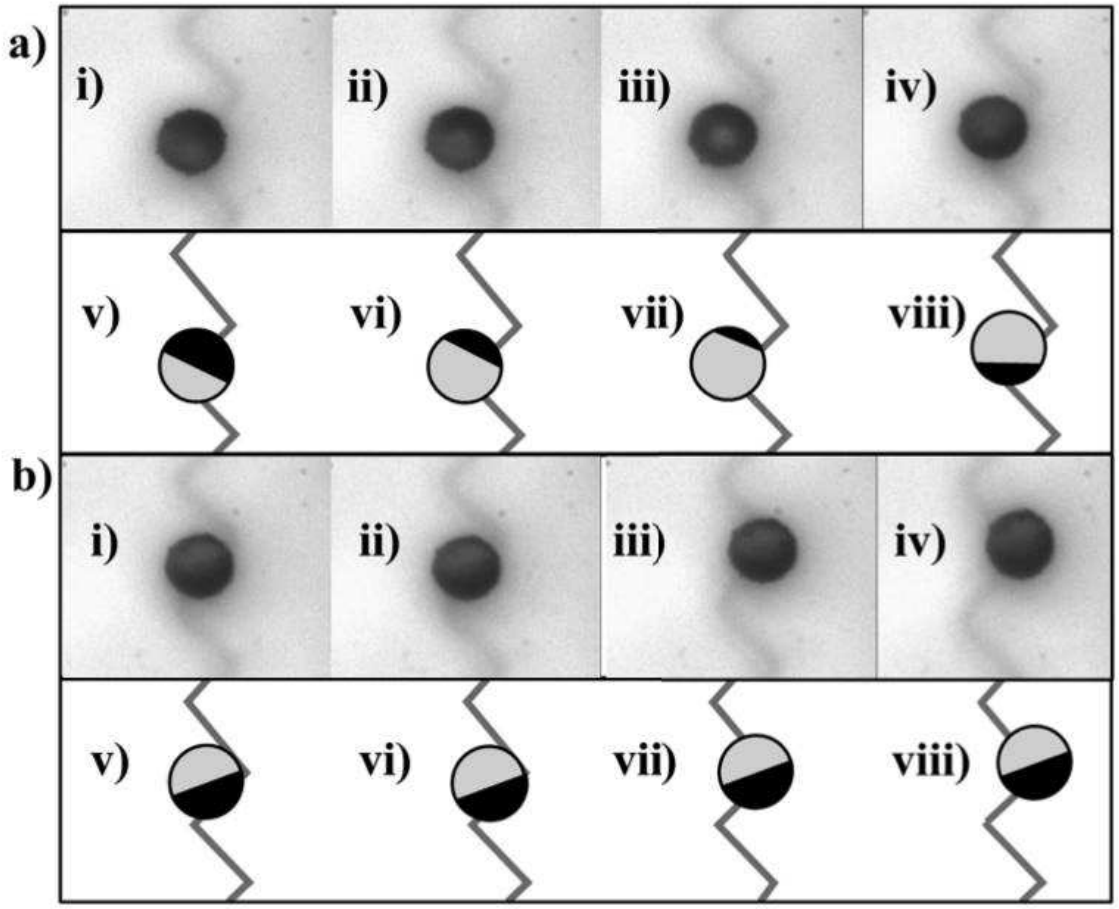

Figure 4.9: 11 μm Janus particle exhibits (A) rolling and (B) sliding motion during vertex-to-vertex transport. Schematic images (iiv) are paired with (vviii) illustrating the orientation of dark- and light (translucent)-colored regions during rolling and translational motion.

acteristic from shape anisotropy of the smaller nanoparticles with faster relaxation times. Further studies are done characterizing these smaller contributions in superparamagnetic beads in Chapter 7. However despite these smaller contributions, the overall field response of the beads is largely in agreement with that of a SPM microsphere.

4.2.4 Forces

The in-plane magnetic force on the SPM bead moving from one vertex to another can be calculated from the spatial and temporal coordinates of the bead. To experimentally

calculate this force, two primary forces are taken into account acting on the bead - the magnetic force propelling it forward and the hydrodynamic drag force resisting the forward propulsion which is determined by Stokes law:

$$F_d = 6\pi\eta r v \tag{4.1}$$

where η is the dynamic viscosity of the fluid, r is the radius of the bead and v is the velocity of the bead. The near wall effects are neglected in this model. The velocity and acceleration for the bead can be calculated thus finding the drag force and the net force which is negligible. Therefore, the magnetic force which equivalently opposes the drag force can be evaluated as shown in Fig. 4.10A for the 2.8 μm beads. Furthermore, the theoretical magnetic force can be calculated from differentiating the energy landscapes shown in Fig. 4.6. The qualitative comparison of the theoretical forces to the experimental forces match very well. However, quantitatively, the peak forces are slightly larger for the theoretical predictions. This may be due to the model not including the initial rolling motion of the bead before translating down the wire and not considering the near-wall effects. These results confirm the ability of the micromagnetic tweezers system to apply picoNewton forces on SPM beads which is very relevant in biological environments.

4.3 Conclusion

The CoFe zigzag wires and permalloy disks are beneficial in trapping and transporting particles. The traps can be tuned in both the CoFe and NiFe ferromagnetic patterned thin films during the design of the structure and choice of microbead diameters as well as during the experiment by applying different strengths of external fields. The energy landscape was probed and the forces on the bead were calculated for multiple external fields. In general for both the wires and the disks, when $\mid \mathbf{H}_{XY} \mid < \mid \mathbf{H}_Z \mid$, no secondary traps were created. In this case, when $\mathbf{H}_Z$ was reversed, the bead was repelled from the initial trap to a final trap on the wires or off the disk. If another disk would have been within reach, then the bead would have been trapped at a new location on a neighboring disk. However, when

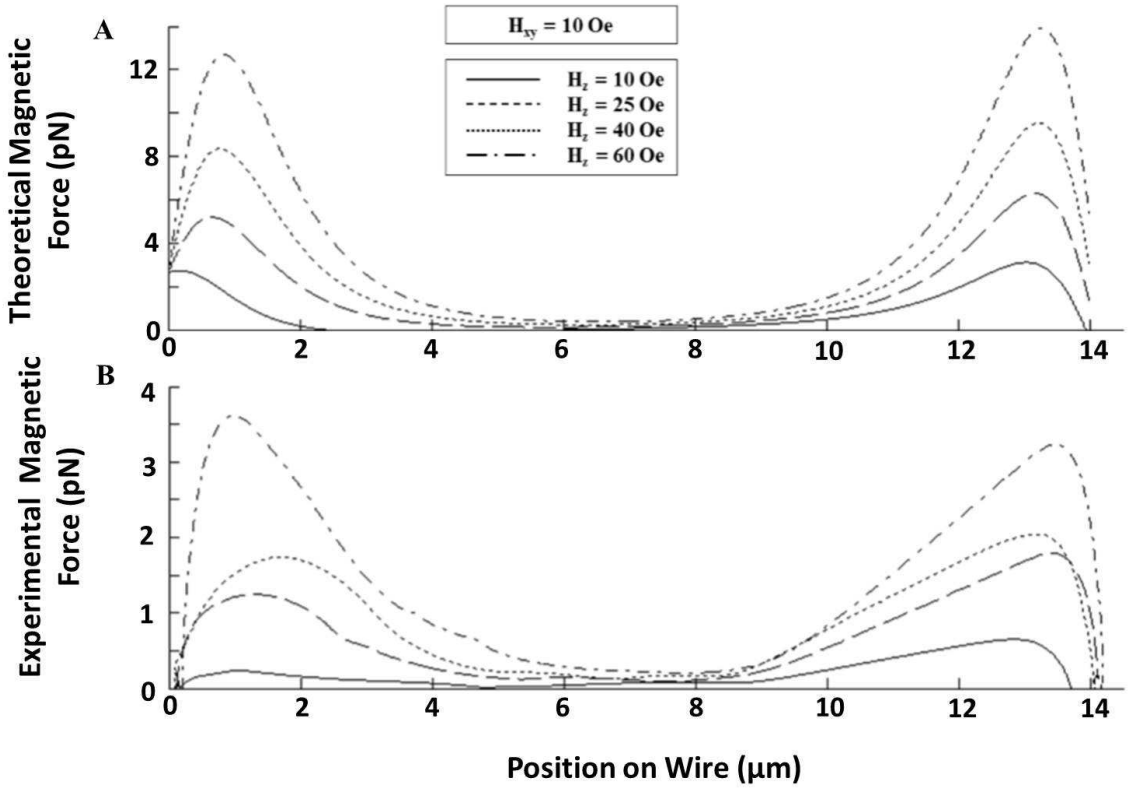

Figure 4.10: Magnetic forces on a SPM bead with a diameter of 2.8 μm. (A) Theoretical in-plane magnetic force derived from differentiating the energy landscape of bead on wires for field strengths $\mathbf{H}_{XY}$ = 10 Oe and $\mathbf{H}_Z$ = 10, 25, 40, and 60 Oe. (B) Experimental in-plane magnetic force calculated from spatial and temporal coordinates of bead transported from on vertex to another for the same field strengths in A. In both plots, the CoFe wires were 14.5 μm long.

$| \mathbf{H}_{XY} | > | \mathbf{H}_Z |$, a secondary trap was created in which the bead could either be slowed down or completely stopped before reaching the final trap. When utilizing the disks, the secondary trap was normally 1 - 4 μm outside of the edge of the disk depending on the disk dimensions and the field strength. By changing the ratio between $| \mathbf{H}_{XY} |$ and $| \mathbf{H}_Z |$, new traps were created as a function of the position of the bead relative to the patterned structure and could be tuned such that the bead would slow down more abruptly or more gradually. The peak forces on the bead located on the wires and disks were measured to lie in the picoNewton regime with forces as high as 60 pN from the 8.8μm beads on 30 μm

permalloy disks. Furthermore, the initial trapping locations can be tuned by changing the ratio between $\mid \mathbf{H}_{XY} \mid$ and $\mid \mathbf{H}_{Z} \mid$ and well-predicted using the theoretical model. This ability to finely control and tune the trapping location for soft and hard magnetic material offers excellent avenues to actuate biological structures.

Chapter 5
Background to DNA Origami

Micron and nanosized molecular machines enable the cell to function and perform tasks in our body in comparable ways to everyday machines used in the world. In order to study biological systems or utilize the potential of these molecular machines, it is necessary to engineer devices on the micron to nanoscale. Watson and Crick's discovery of the base-pairing interaction of DNA [122] established DNA as the best candidate for programming and constructing these small machines. In the early 1980s, Nadrian Seeman paved the way to utilize the base pairing interactions in DNA to form structures through flexible branched DNA junctions [123–125]. More rigid structures were developed from these junctions and DNA motifs assembling including lattices [126–136], enabling fabrication of nanotubes and arrays [137–140], and forming polyhedral constructs [141–146]. Later, 2-dimensional [147] and 3-dimensional [148] shapes were formed from DNA tiles and blocks made from the DNA junctions which also included some curvature [149].

The initial breakthrough in the advancement of complex 2D and 3D shapes was greatly enabled through the technique called DNA origami, first introduced by Paul Rothmand in 2006 [150]. Prior to the DNA origami method, the technique to create DNA structures utilized only short strands of single-stranded DNA (ssDNA). Measuring precise stoichiometric ratios of ssDNA is challenging, and often led to low folding yields. However, DNA origami does not depend as much on precise stoichiometric ratios to produce high folding yields since it uses a long loop of ssDNA and short strands of ssDNA to fold the structure [151]. Furthermore, it has allowed for more complex structures to be engineered with nanoscale

precision including 3D structures [152–156], DNA bundles and nanotubes [157–163], programmed twist and curvature [164–166], microstructures from polymerized DNA nanostructures [167–174] and dynamic DNA devices [175–188]. These DNA structures have shown great potential in measurement techniques, precise nanoscale templates, molecular motors, medical applications such as drug delivery, and electronic applications [151, 179, 189–191]. This chapter will briefly discuss the progression of DNA nanotechnology and will explain the background of DNA origami and the energetics of its formation. In Chapter 6, the optimization, assembly and actuation of three specific DNA nanostructures will be discussed. In Chapter 7, micron length DNA rods assembled from DNA nanostructures will be utilized to study the magnetic moments in superparamagnetic beads.

5.1 Deoxyribonucleic Acid (DNA)

The building material of DNA origami structures is deoxyribonucleic acid (DNA) which is composed of a chain of nucleotides. In nature, DNA encodes the genetic makeup of each person. Each nucleotide is assembled from a sugar, a phosphate and one of four nitrogenous bases [192, 193] (Fig. 5.1A). The names of these bases are adenine, thymine, guanine and cytosine, often symbolized as A, T, G and C respectively. These nucleotides are chemically linked to one another when the sugar base of one nucleotide binds to the phosphate group of an adjacent nucleotide forming single-stranded DNA (ssDNA) including a sugar-phosphate backbone with a string of connected nitrogenous bases (Fig. 5.1B). Furthermore, ssDNA is directional in that the ends of the strand are not chemically identical since one side ends with a sugar base (hydroxyl group) and the other ends with a phosphate (phosphate group) and are referred to as the $3'$ and $5'$ ends respectively. When the sequence of bases is written down, generally, it is written from the $5'$ to the $3'$ end.

Double-stranded DNA (dsDNA) forms when the nucleobases hybridize with complementary nucleobases (adenine and thymine, guanine and cytosine) via hydrogen bonds (Fig. 5.1C). The specificity of which bases is complementary are determined by the conformational design of each base including the number of hydrogen bonding sites available and

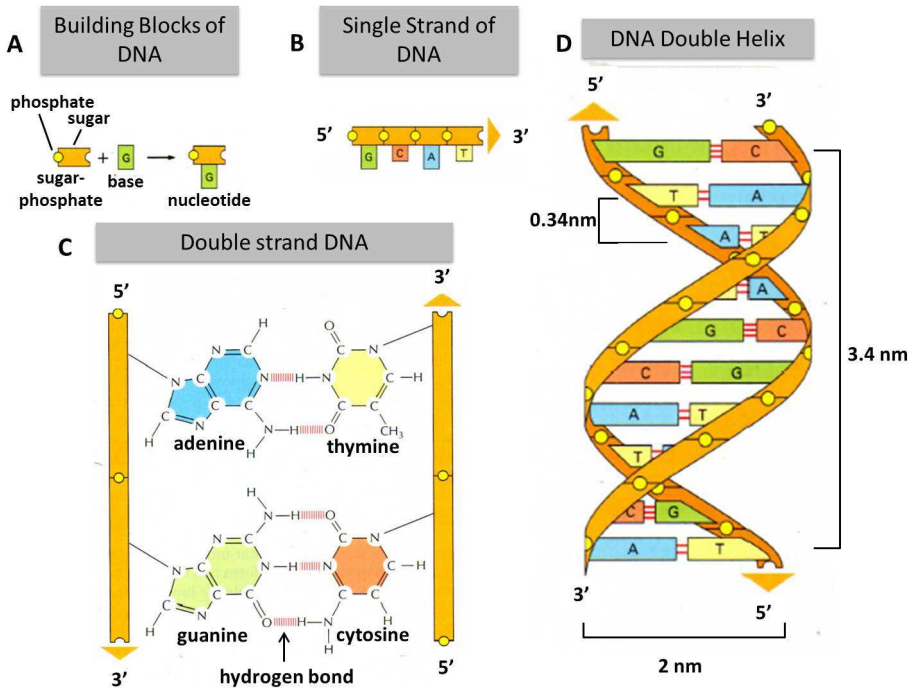

Figure 5.1: Structure of DNA. (A) Each nucleotide which forms DNA is comprised of a sugar, a phosphate and one of four nitrogenous bases (adenine (A), thymine (T), guanine (G) and cytosine (C)). (B) Single Stranded DNA (ssDNA) forms when these nucleotides are chemically linked together through the sugar-phosphate backbone. (C) Double-stranded DNA (dsDNA) construct when complementary basis (AT and GC) hybridize via hydrogen bonds. (D) dsDNA most commonly assembles a helix structure in which the base pair stacking separation is around 0.34 nm, the distance for a complete turn is around 3.4 nm, which is about 10.5 bases, and the width is around 2 nm [193, 195].

the size of the base molecule [194]. Adenine and guanine referred to as purines are larger than thymine and cytosine referred to as pyrimidines. Therefore, each of the base pairs in dsDNA form between a large (purine) nucleobase and a small (pyrimidine) nucleobase. This selection is specific to the number of hydrogen bonds in each case in that A-T has only two hydrogen bonds whereas C-T has three hydrogen bonds.

DNA is energetically more stable when it creates double helical strands (Fig. 5.1D) rather than single strands or straight double strands due to the base pairing interaction, base stacking interaction and hydrophobic interaction [196]. The base pairing interaction describes the attraction of the specific complementary bases. The base stacking interaction

– a complex interaction depending on several noncovalent forces – refers to the vertical attraction between nucleotides. The hydrophobic interaction, sometimes included in the base stacking interaction, denotes the repulsive interaction of the hydrophobic bases in water. Since sugars and phosphates both are hydrophilic, the sugar-phosphate backbone surrounding the bases reduces the contact between water and the bases by forming a helical structure. When dsDNA constructs its standard helical state, the nucleobases become spaced out by 0.34 nm with a diameter of approximately 2 nm [193]. These geometric size dimensions are very important constraints when using dsDNA to construct 3D structures.

5.2 Progression of DNA Nanotechnology

5.2.1 Junctions

Structural DNA nanotechnology emerged in 1982 when Nadrian Seeman first self-assembled DNA junctions and used it to form 2-dimensional lattices [123]. These DNA junctions were based on naturally occurring DNA crossovers called Holliday junctions where two dsDNA are separated into four ssDNA in order to exchange certain genetic information. The sequence of the strands is such that the junction is mobile. However, Seeman showed that semimobile and immobile junctions could be assembled by limiting the number of bases that were complementary to one another near the junction. In the case of the semimobile junction shown in his original work in Fig. 5.2A, a base on ssDNA 1 which is initially bound to a base on ssDNA 4 is also made complementary to the base on ssDNA 2 such that 3 or 4 bases in ssDNA 1 can bind to ssDNA 2. In Fig. 5.2B, Seeman designed a junction that was completely immobile such that only the first 8 bases on ssDNA 1 would bind to ssDNA 4 while the second 8 bases would only bind to ssDNA 2. Seeman′s 4-arm junctions paved the way to junctions of increased number of connection strands with others creating 8-arm and a 12-arm junctions [125] as shown in Fig. 5.2C.

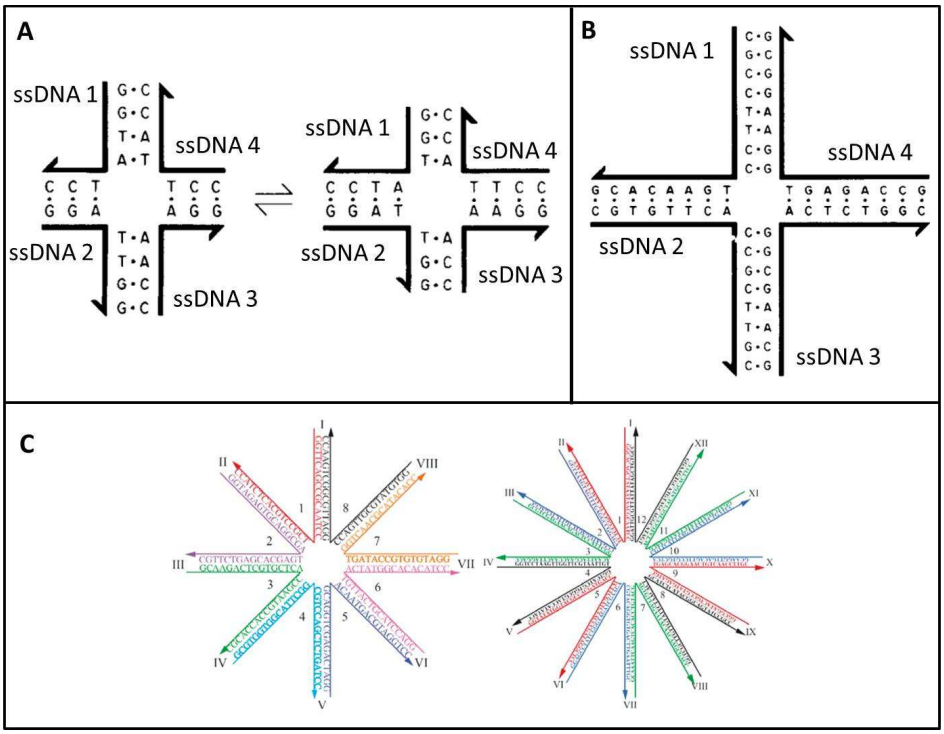

Figure 5.2: DNA Junctions(A) A 4-arm semimobile junction was designed using 4 ssDNA that are complimentary to the other strands such that two possible binding configurations can form. Hence, the junction is able to move by one base pair [123]. (B) A 4-arm immobile junction was designed using 4 ssDNA such that only one binding configuration is formed. Hence the junction is not able to move [123]. (C) An 8-arm junction formed by 8 ssDNA and 12-arm junction formed by 12 ssDNA [125].

5.2.2 Constructs Assembled from DNA Junctions and Motifs

These junctions can then be used to form 2- and 3-dimensional lattices. Fig. 5.3A shows Seeman′s original design to form 2 dimensional lattices structures from immobile 4-arm junctions. ″Sticky ends″ were formed on each side of the junction in which single strands of DNA were left in excess and made complementary to the single strands on other sides of the junction. For example in Fig 5.3A, the ssDNA at A is complementary to the ssDNA at A′ and ssDNA at B is complementary to the ssDNA at B′. Therefore, when the junctions are combined together they self-assemble into a 2-dimensional lattice by binding the complementary sticky ends together. This theoretical design was later confirmed by arranging these 4-arm junctions such that 2D arrays were formed and imaged on the AFM (Fig. 5.3B)

[126]. Other lattice formations were then realized [126–136] with some images showing the different lattice formations in Fig. 5.3C-F.

Nanotubes constructed from these DNA junctions and motifs were then formed [137–140]. The nanotubes were made up of DNA tiles constructed from DNA motifs and junctions that were connected together to assemble DNA helices circumferentially connected together to create nanotubes with DNA helices completing the parameter. The diameter of the nanotubes ranged from 7 nm up to 25 nm with lengths in the tens of microns. Fig. 5.3G and H show a fluorescent and an AFM image respectively of two different nanotubes that were fabricated.

Nano Polyhedral structures were also designed and assembled using DNA junctions and DNA motifs [141–146]. Seeman first synthesized a 3D block-like structure (Fig. 5.3I) in a series of steps where ssDNA was hybridized to form these specific junctions [141]. Other structures were formed including octahedron, tetrahedra, bipyramid and polyhedra. Fig. 5.3J and K show two of these structures that were constructed and imaged using cryo-electron microscopy (cryo-EM). Furthermore, dynamic nanodevices were also assembled from DNA junctions and DNA motifs where structures could reconfigure as well as display a range of complex motions. Since this dissertation focuses on the method of DNA Origami to self-assemble 3D devices, the dynamics of these initial DNA structures will not be discussed. The following reviews can be explored for more information on dynamic nanodevices and static structures formed from DNA junctions and motifs and the progression of nanotechnology [151, 179, 189–191].

5.2.3 Constructs from DNA Origami

Assembly of more complex geometries was greatly enabled through the development of DNA origami where a long loop of ssDNA (scaffold) is folded into a precise, compact geometry using hundreds of short oligonucleotides (staples), via programmed molecular self-assembly. The initial breakthrough came in 2006 when Rothmund demonstrated that a long scaffold strand derived from the M13mp18 bacteriophage viral genome (∼7,000 bases long) was programmed to self-assemble into two-dimensional shapes such as a square, rectangle, star,

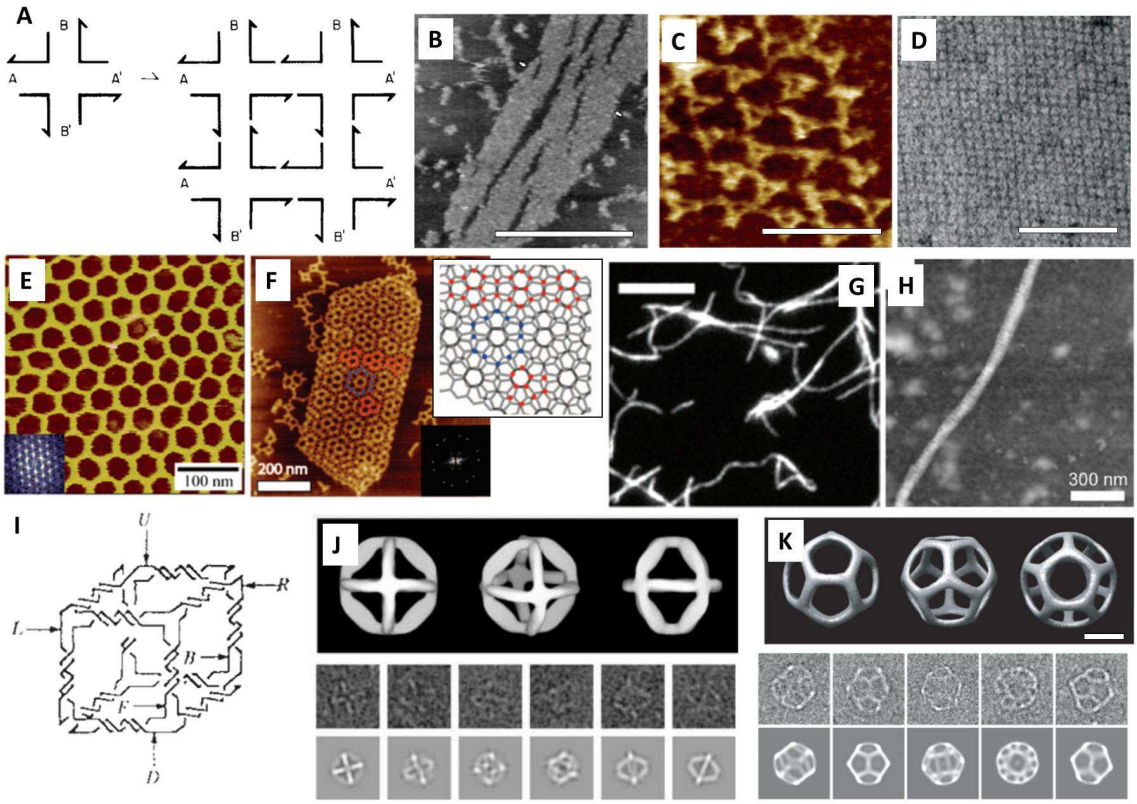

Figure 5.3: Constructs formed from DNA junctions and motifs. (A-F) Lattices: (A) Theoretical design showing how DNA junctions can form 2D lattice using ″sticky ends″ such that A and A′ bind and B and B′ bind [123]. (B) AFM image of a two-unit lattice. Scale bar: 300 nm [126]. (C) AFM image of DNA triangle arrays. Scale bar: 100 nm [130]. (D) TEM image of a RuvA-DNA crystal lattice. Scale bar: 100 nm [131]. (E) AFM image of 2D crystalline DNA arrays self-assembled from three-point-star motifs. Inset is the Fourier transform. Scale bar: 100 nm [132] (F) AFM image of two layers of a DNA hexagonal array rotated 20° with respect to one another. Inset is Fourier transform. A diagram of the two layer assembly is illustrated such that the blue and red dots correspond to dots on AFM image. Scale bar: 200 nm [135]. (G-H) Nanotubes: (G) Fluorescent image of DNA filaments. Scale bar: 5 μm [137]. (H) AFM image of DNA nanotube formed from triple-crossover tiles. Scale bar: 300 nm [138]. (I-K)Polyhedral objects: (I) Synthetic scheme used to synthesis a cube-like object [141]. (J) Three views of the 3D DNA octahedron projection reconstructed from individual raw cryo-electron microscopy images [143]. (K) Three views of the 3D DNA dodecahedron projection reconstructed from individual raw cryo-electron microscopy images. Scale Bar: 20 nm [146].

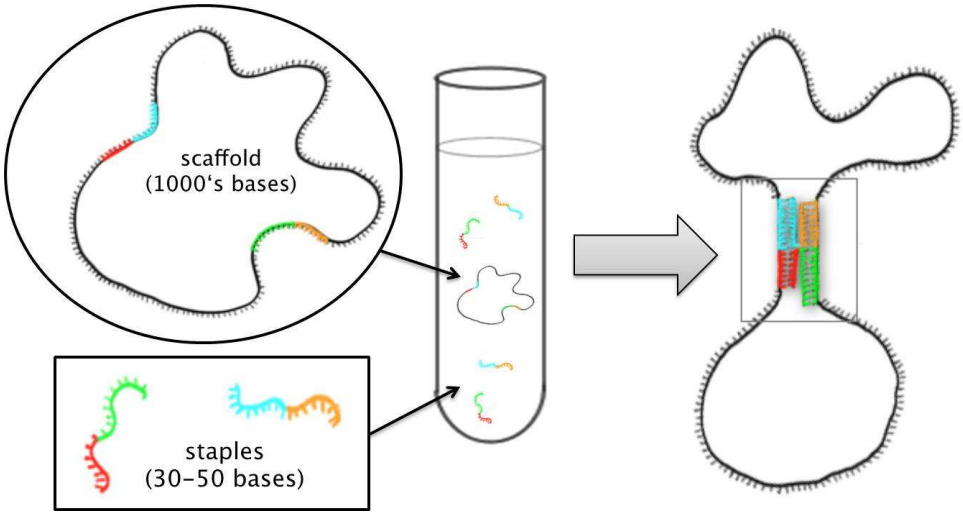

Figure 5.4: Origami Folding Principle. DNA origami is folded by suspending a scaffold strand, which is a long loop of ssDNA, with staples that are piecewise complementary to sections on the scaffold. In the single fold illustrated, the staple with the red and the green sequence design will hybridize to the red and green template strand on the scaffold and the staple with the blue and the yellow sequence design will bond to the blue and yellow template strand on the scaffold. When the staples attach in this manner, the scaffold strand is pulled together in the middle. Using this principle, more complex structures can be folded. Image curtsy of Dr. Hendrik Dietz at Technical University of Munich (TUM).

smiley, and triangle through the use of short ssDNA as seen in Fig. 5.5A [150]. This folding principle is illustrated in Fig. 5.4 in which a scaffold or template strand, composed of a long (7,000 to 8,000 bases) loop of ssDNA, is folded into a structure using 100 to 200 piecewise complementary staples (short ssDNA 30 to 50 bases long) according to the Watson-Crick interaction [195].

Three-dimensional structures were designed through utilizing the DNA origami method to form structures such as a prism structure [152], tetrahedron molecular container [153], box with a controllable lid [154], and other 3D shapes including a rectangular prism, square nut, railed bridge, slotted cross (Fig. 5.4B) and a stacked cross [155]. Cryo-EM imaging of 3D DNA origami structures enabled more precise imaging and mapping of the each helix composing the structure [156]. The method of DNA origami could not only be used to make DNA nanotubes [157–159] as seen in the fluorescent image in Fig. 5.4C but also could easily modify various versions of nanorods with rectangular lattices [160, 163], honeycomb lattices

[161, 163] and even hybrid versions with both lattices [162]. By varying the number of helices, the thickness and length of the structure could be modified. In exploiting mechanical stress in DNA nanostructures, twist and curvature were then programmed into these 3D objects to design bends such as nanogears (Fig. 5.4D) [164] and spherical objects such as a nanoflask (Fig. 5.4E)[165]. Incorporating ssDNA components creates entropic forces that further induce compression or bending in DNA structures [166, 167]. Although these 3D nanostructures are limited in size (10 - 100 nm), they can be designed to polymerize and form larger structures (several microns in length) via ssDNA that bind one side of the structure to another forming two-dimensional arrays [168], larger patterned tiles (Fig. 5.4F) [169, 170], nanoribbons [171, 172] and nanorods (Fig. 5.4G) [173, 174].

Furthermore, structures were designed to exhibit dynamic behavior and functionality such as reconfiguration or actuation. Initial progress was made in conformational changes such as reconfiguration of nanoribbons [175], sensing devices such as DNA pliers and forceps which reconfigure in sensing certain molecules [176], or opening and closing of containers [154, 177, 178]. Further dynamic structures were designed by utilizing the mechanical properties of DNA and exploiting the ability to induce mechanical stress [179] such as in creating bistable mechanisms [180, 181], and joints such as hinges (Fig. 5.4H) and sliders (Fig. 5.4I) [182, 183]. By combining joints and stiff rods together more complex mechanisms can be formed such as the crank slider, bennett linkage [182] and a multicomponent rotor [184]. Other work has involved exploring how to utilize these machines to perform work in which several methods have initially been tested including using strand displacement [154, 175, 177, 180, 182, 183, 185], molecular sensing [176, 178, 186], hydrophobic interactions [187], temperature changes [185], ionic changes [185] and exploiting plasmonic nanoparticles [188]. Most of these approaches release or facilitate local interactions, and hence their control is limited typically to stabilizing a pre-programmed state as opposed to directly manipulating the structure with an applied force to achieve a specific state. In Chapter 6, a magnetic approach to directly manipulate the structures by exploiting superparamagnetic beads will be discussed.

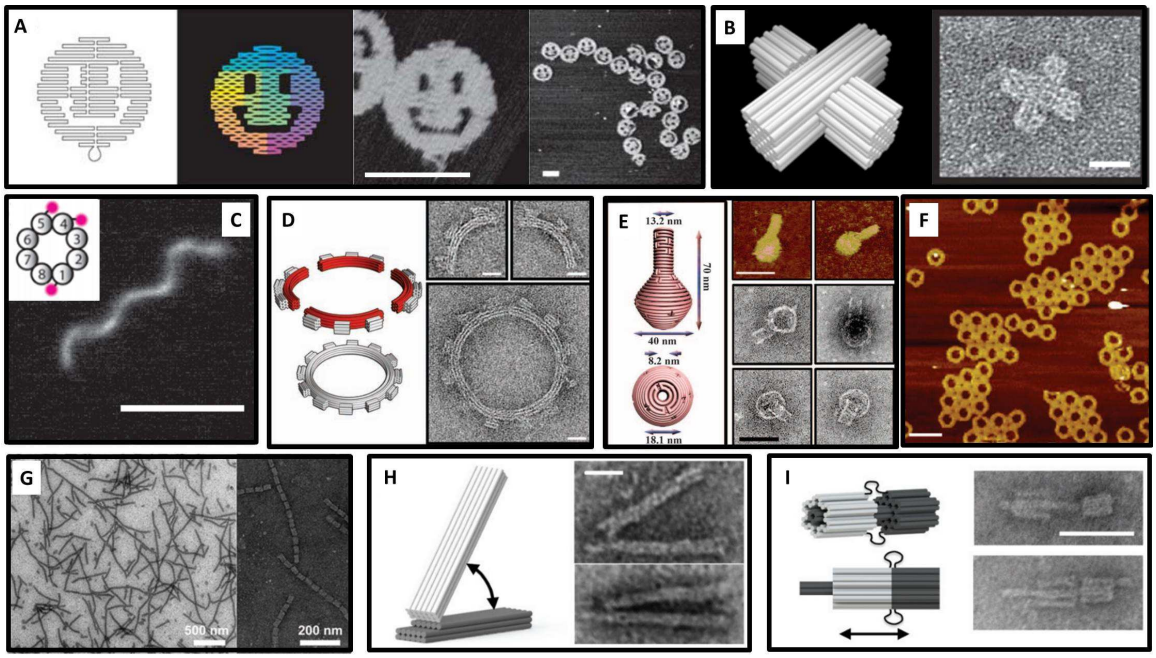

Figure 5.5: Constructs Formed from DNA Origami (A) Scaffold routing of 2D disk-shaped smiley. Diagram shows the bending of helices at crossovers. AFM images of structure. Scale bar: 100 nm (both)[150]. (B) Cylinder model of slotted cross (cylinder=helix) and TEM image. Scale bar: 20 nm [155]. (C) Fluorescence microscopy image of 8 Helix nanotubes. Scale bar: 5 μm [159]. (D) Cylinder model of 3-by-6helix bundle modified to bend into a quarter circle with a 50 nm radius in which a hierarchical assembly yields 12-tooth gears. TEM images of structures. Scale Bar: 20 nm [164]. (E) Schematic representation of DNA nanoflask. (Top) AFM images, Scale bar: 75 nm. (Bottom) TEM images, Scale bar: 50 nm [165] (F) AFM images of hexagonal staple tiles assembled into a superstructure. Scale 200 nm [169] (G) TEM images of polymerized DNA origami bundles. Scale bar: 500 nm and 20 nm respectively [173] (H) Cylinder model of DNA hinge joint. TEM images showing hinge at two orientations. Scale bar: 20 nm [182]. (I) Cylinder model of slider Joint. TEM images of joint at two orientations. Scale bar: 50 nm [182].

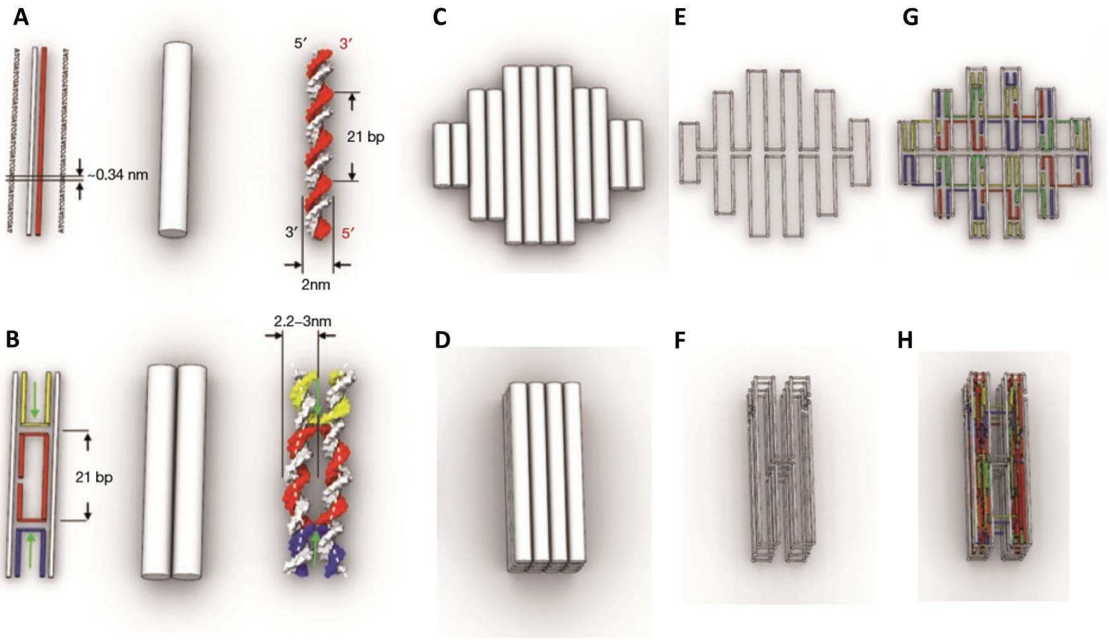

Figure 5.6: Designing DNA Origami Structure. (A) Structures are composed of dsDNA in which the helix is represented by a cylinder. The helix is formed when the scaffold strand (white) binds to the staple (red). (B) Individual helices are connected to adjacent helices through interhelix cross-overs in which a staple binds two different sections of the scaffold. (C-D) Cylinder model representing the design of two structures. (E-F) Scaffold routing for each structure. (G-H) Completed scaffold-staple layout where the staples are shown in multiple colors. Figure from Castro et al. [195].

5.3 Basics of DNA Origami

5.3.1 Steps to Assemble a DNA Origami Structure

Five basic steps can be followed to assemble DNA structures using the method of DNA origami [195]. First, the targeted structure is envisioned, which includes identifying the dimensions, packing lattice and mechanical functions of the structure. Since dsDNA has a diameter of around 2 nm, often each individual helix is represented as a cylinder of 2 nm with the length given by the specific length of each helix in the design (Fig. 5.6A). Structures are formed by connecting helices together (Fig. 5.6B). Examples of two envisioned structures represented using the cylindrical models are shown in Fig. 5.6C and D.

Second, the structure is engineered by designing scaffold routing (Fig. 5.6E and F)

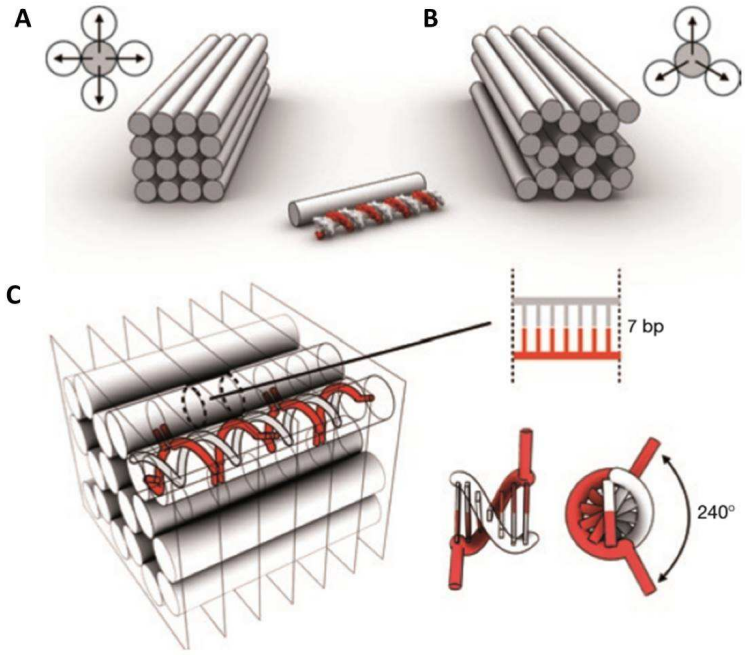

Figure 5.7: The DNA helices in the structure can either be close-packed into (A) a square lattice with fourfold symmetry or into (B) a honeycomb lattice with threefold symmetry. (C) In order to form crossovers every 240° to connect adjacent helices at 0°, 120° and 240°, staples must crossover every 7 bases. Figure from Castro et al. [195].

and determining its complementary staple sequences (Fig. 5.6G and H) which are often accomplished through the assistance of the computer program caDNAno [161]. In this interface, the user can initially design the cross-section of the structure and route the scaffold such that it travels through all the cylinders without going through a cylinder twice. When populating the scaffold with the staples, the program takes into account specific crossover rules which determine the packing lattice structure and prohibits incorrect staple crossovers.

The DNA helices in the structure can either be close-packed into a square lattice with fourfold symmetry or into a honeycomb lattice with threefold symmetry (Fig. 5.7). The staple crossover position along the helical axis of one helix to a neighboring helix determines the placement of the neighboring helix. In order to form a square lattice, a helix will have four neighbors that are 90° from one another whereas the honeycomb lattice will have three neighbors that are 120° from one another. Since the B-form DNA double helix has a natural

helicity of 10.5 base pairs per turn, the double helical domain will rotate 240° in 7 base pairs. Therefore, honeycomb lattices are formed by placing staple crossovers every 7 base pairs giving the threefold symmetry with neighboring helices at 0°, 120° and 240°. The natural helicity of the B-form DNA, however, does not easily form 90° rotations. Therefore by assuming an average helicity of 10.67 base pairs per turn, fourfold symmetry can be accomplished with 8 bases between crossovers which would relate to a 270° turn of the backbone. Although this crossover rule enables square lattice formation, it introduces an internal torque which can result in global twist deformation [160, 164, 195].

These staples form the majority of crossovers in the structure and are generally designed to lie between 30 - 50 bases in length using 150 - 200 unique staples in total. Generally, the staples should have at least three sections of 7 sequential base pairs complementary to the scaffold in order to be energetically favorable to remain bound at room temperature. Since the scaffold is circular, the staple sequence is determined by choosing a virtual starting point for the scaffold and then assigning the reverse complementary sequences to the staples. By shifting the starting location, a complete set of different staples can form the exact same structure.

Third, the scaffold is prepared through phage plus purification of the M13mp18 bacteriophage genomic DNA and the staples are commercially purchased. A protocol for the scaffold production from the M13mp18 bacteriophage genomic DNA [157] producing a loop of 7249 bases can be found in the supplemental information of Castro et al [195]. Derivatives of this scaffold can also produce scaffolds of other lengths including 7560 and 8064 bases. The staples were commercially purchased either from Eurofins or IDT and typically came in single tubes or multiwell plates with a concentration around 100 μM.

Fourth, the staples are pooled with the correct volumetric ratios. Staples are combined together in equal amounts to form several pre-stocks which form a collection of different sections or components of the structure. The pre-stocks are then merged together in equal volumetric ratios to form a working stock where all the staples will result in the same concentration (500 nM for structures in this dissertation). For one structure, multiple workstocks may be made which will have different modifications to the same structure.

Finally, the folding reaction is prepared and thermal annealing cycle is implemented for molecular self-assembly of the structure. The folding reaction varied from structure to structure. Generally, the scaffold strand (final concentration of 20 nM or 40 nM) is combined with the working stocks (final staple concentration of 200 nM) such that the staples are 5 to 10 fold excess to the scaffold to ensure better folding yields. The assembly buffer contained 1 mM EDTA, 5 mM NaCl, 5 mM Tris, and $MgCl_2$ ranging between approximately 16 - 22 mM (varied from structure to structure). The positive divalent ions from the magnesium served to screen the negative phosphate backbone of DNA in order to form close-packed structures. This will be further discussed in the following section which presents the energetics of folding the structure.

The structures are then self-assembled through a slow or quick fold thermal denaturation and annealing procedure. The slow fold reaction entails heating the sample to its melting temperature at 65°C and then slowly cooling it to 4°C over a time period of days depending on the complexity of the structure. The quick fold reaction, first introduced in 2012 [197], entails heating the sample to its melting temperature at 65°C and then holding the temperature constant at a specific lower annealing temperature for a much shorter amount of time which varies from structure to structure. Using this process structures can be folded within a few hours. The salt concentrations and annealing temperature and ramps must be specifically optimized for the highest folding yields for each structure. The constructs are confirmed to be well folded through gel electrophoresis, TEM or AFM imaging. Furthermore, structures are purified from the excess staples through multiple methods including gel electrophoresis, peg purification, and spin column purification which are discussed in Chapter 3.

5.3.2 Energetics of Folding DNA Origami Structures

Similar to the stability of dsDNA, DNA origami structures are more stable in lower free energy states. In minimizing the free energy, there is competition between minimizing the internal energy of the DNA origami structure and maximizing the entropy which measures the number of possible folding states of the structure. At high temperatures, maximizing

the entropy is more beneficial and at low temperatures minimizing the internal energy is more beneficial. Therefore, DNA structures will unfold at high temperatures, known as the melting temperature, since this increases its entropy more, and will fold at lower temperatures, since this decreases its internal energy more.

The internal energy of DNA origami structures is decreased through stabilizing interactions and increased through destabilizing interactions. The base pairing interaction and the base stacking interaction, both of which are also important in the formation of the DNA double helix, are stabilizing interactions in the formation of DNA origami constructs [198]. As explained earlier, the base pairing interaction describes the attraction of complementary bases. In minimizing the internal energy, the attraction of bases causes the structure to fold since more internal energy is needed to separate bases in close proximity than used to allow them to bind. This effect is amplified as the number of complementary bases in a strand is increased, causing faster attachment. Futhermore as previously explained, the base stacking interaction describes the attraction between vertically stacked bases. Interestingly, the base stacking interaction more largely impacts the stability of DNA structures than the base pairing interaction [198]. Furthermore, there is a greater attraction in GC stacks than in AT stacks, causing sequences with more GC patterns to have higher melting temperatures. Both base pairing and base stacking interactions are increased as bases are brought closer together. Therefore, a structure can more easily fold when key staples attach to the scaffold, making it more energetically favorable for other staples to bind. This effect, known as cooperative folding, largely enables the folding of the structure. Cooperative folding may potentially be the reason why the fast folding technique works, although this is not fully understood.

The main destabilizing interactions in the formation of DNA origami structures are electrostatic repulsion between the DNA helices and internal stress. Since DNA helices are negatively charged, a greater amount of internal energy is needed to fold the structure by bringing the DNA helices closer [195]. By adding salt into the solution, positive ions from the salt act as a shield causing the DNA helix to appear neutral at a certain distance. This reduces the electrostatic repulsion allowing the structure to fold more easily [192]. The

distance in which the DNA will appear neutral is dependent on the concentration of positive ions in the solution and therefore the formation of DNA origami structures are dependent on salt concentration. Hence, by increasing the salt concentration in the solution, structures becomes more stable and the melting temperature increases [195]. Internal stress energy arises from several factors including mechanical strain and incorrect scaffold or staple pairing [195]. Mechanical strain refers to energy stored in bent or twisted structures programmed to occur by engineering staple crossovers at certain helix locations. Incorrect scaffold or staple pairing refers to energy from incorrect binding of the scaffold strand or staples which prohibit correct staples from attaching.

As the structure seeks to minimize its internal energy and maximize its entropy, the system can become caught in smaller energy minima referred to as kinetic traps [195]. Programming of the sequences and routing of the staples can be important in helping to reduce these kinetic traps. For example, if a staple is routed to connect four helices in which its longer sequence strands are located on the outer helices, the longer stands will attach first, since it is more energetically favorable. However, the inner helices will not attach since the ends are not free to move to enable the staples to twist and form the double helix with the scaffold strand. This kinetic trap can be avoided by programming the larger sequences to form along inside helices. There is other similar scaffold and staple routing rules that can be followed to reduce the number of kinetic traps.

5.3.3 Mechanical Properties of DNA Origami Structures

In designing structures on the nanoscale, the mechanical properties play a vital role in the functionality of the structure. By increasing rigidity, thermal fluctuations of the structure can be reduced and more well-defined shape created. In designing kinematic mechanisms and machines, two design parameters are necessary: (1) relatively stiff links that connect to joints and (2) joints need to be flexible to allow for various degrees of freedom. Typically, the links are assumed to be infinitely rigid, however, in practice, this implies that the mechanical stiffness of the link must be much greater than the stiffness of the joint. These parameters hold true whether the designing macro or nanomachines.

In the fabrication of nanomachines out of DNA, these design criteria are met by utilizing dsDNA for links and ssDNA for joints. The main deformation mode that affects the links is bending which is characterized in terms of the persistence length (L_p) given by the equation:

$$L_P = \frac{EI}{k_B T} \tag{5.1}$$

where EI is the beam bending stiffness, k_B is Boltzmann′s constant, and T is absolute temperature. The bending persistence length of a filament characterizes the competition between the entropy of the filament wanting to increase, by allowing the filament to bend in various orientations, and the internal energy that would increase due to the energetic cost of bending the filament. Hence, L_p describes the length in which the filament will bend significantly due to thermal fluctuations. Therefore, if the filament is much shorter than L_p, it will behave as a stiff straight rod. However, if the filament is much longer than the L_p, it will freely bend in all directions and behave as a random coil.

Type	Size	Persistence Length	Reference
Nanotubes	7-20 nm diameter	3.9 μm	[137]
Nanotubes	5 helix tube	2.0 μm	[159]
Nanotubes	10 helix tube	16.8 μm	[159]
DNA Origami Bundles	6 hb	1.6 μm	[166]
DNA Origami Bundles	4 hb	0.74 μm	[158]
DNA Origami Bundles	6 hb	1.88 μm	[158]

Table 5.1: Persistence Length of DNA Structures. Summary of persistence length measured for DNA nanotubes and DNA origami bundles. Persistence length increases with increasing number of helices.

Although the persistence length is partially dependent on salt concentration, for ssDNA, its L_p is approximately 2 nm [199] and for dsDNA, its L_p is approximately 50 nm [200]. By bundling multiple helices together, the difference in L_p compared to ssDNA can be further magnified. Table 1 shows the experimentally measured persistence lengths for nanotubes and DNA origami bundles with different number of helices. Castro et al. has further

Joint	Symbol	DOF	Diagram	DNA Origami Design
Revolute	R	1		
Prismatic	P	1		
Cylindrical	C	2		
Universal	T	2		2R
Spherical	S	3	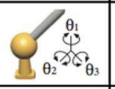	
Planar	E	3	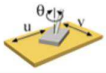	2P + R

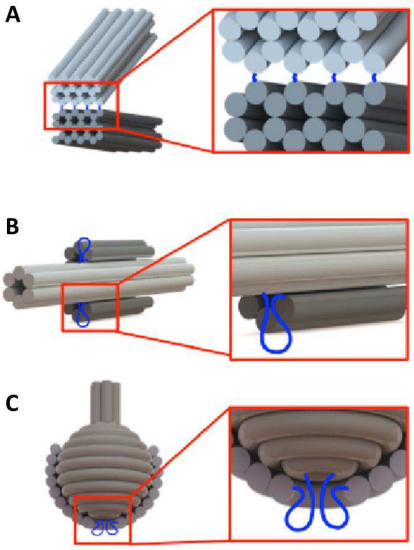

Figure 5.8: Table of possible joints with listed degrees of freedom, macroscale diagram and cylindrical model representing possible DNA origami design. Links are connected with single-stranded overhangs shown in blue in the cylindrical model of the (A) hinge joint, (B) slider joint, (C) ball bearing joint. Table and figure from Marras et al. [201].

analyzed how L_p scales as a function of the number of helices [179]. In order to make micron length stiff rods out of DNA, DNA origami bundles of 56 helices were used in the work presented in this dissertation.

Joints in nanomechanisms are created by connecting these stiff DNA bundles together via ssDNA to define the motion and degrees of freedom of each stiff DNA bundle. Even more complex paths can be created by combining joints together. Marras et al, discuss and illustrate six types of joints (revolute, prismatic, cylindrical, universal, spherical, and planar joints) with their corresponding potential DNA origami design as shown in Fig. 5.8 [201]. Flexible ssDNA join two rigid DNA structures in which a revolute joint acts like a hinge, a prismatic joint extends the length of the ssDNA, and a spherical joint behaves as a ball and socket joint. Specifically hinges and rotors were assembled and magnetically actuated in the work presented in this dissertation. In Chapter 9, future work will discuss the potential of magnetically actuating similar joints.

Chapter 6

Real-time control of DNA origami nanodevices via Magnetic Actuation

6.1 Introduction

The ability to control the motion of molecular devices in real-time with well-defined temporal and spatial control is a central goal of nanotechnology. Tremendous advances have been made in the self-assembly of complex nanodevices or nanomaterials from DNA [189, 202–204], amino acid components [205–207], colloids [208–210], or nanomaterials [211–213]. In particular, DNA origami nanotechnology [150, 155, 195] has enabled the design and fabrication of dynamic nanodevices that can exhibit complex motion [179, 182, 185], programmed conformational changes [180, 185, 188], long range motion or transport [214], and tunable mechanical response [167], making this a highly attractive approach for the development of nanomachines. The ability to control these nanodevices in real-time is essential to enable functional robotic systems at the molecular scale. Current methods to actuate DNA nanodevices typically rely on introducing strands into solution that bind to or displace components on the structure to reconfigure a device with response times of ∼1 min or greater [182]. Other recent developments have introduced changing buffer conditions such as ion concentrations to reconfigure structures [215], and one study demonstrated actuation times on the scale of ∼10 seconds via temperature changes [185]. Achieving actuation response times at the sub-second scale remains a challenge. Furthermore, all current actuation ap-

proaches release or facilitate local interactions, and hence the control is limited to stabilizing one or a few pre-programmed states as opposed to directly manipulating the device into a specific configuration with an applied force. The goal of this work is to establish a robust approach for the direct real-time manipulation of DNA nanodevices with precise spatial resolution, sub-second response times, and tunable applied forces.

While direct manipulation is challenging at the molecular scale, mechanical control of microscale systems is well-established, for example through manipulation of micron-sized magnetic particles via an externally applied magnetic field [85, 91, 92]. The main challenge of translating this approach to directly manipulate molecular scale devices is that scaling magnetic particles down in size results in increased thermal fluctuations and decreased forces. For example, Xu et al. [216] measured forces of <1 femtoNewton for superparamagnetic nanoparticles with a diameter of ∼30 nm at magnetic fields up to 300 Oe. However, previous studies have shown the forces and torques required to reconfigure dynamic DNA nanostructures to be on the scale of ∼1 picoNewton or ∼10 - 50 pN·nm [182], respectively, which would require superparamagnetic beads that are ∼1 μm in diameter. Therefore, providing the necessary forces for actuation presents the challenge of a large mismatch in length scales between the actuator and the machine.

In this study, the challenge of bridging microscale manipulation to nanoscale devices was overcome using a stiff mechanical lever with a high aspect ratio where the cross-sectional dimensions are on the scale of the nanomachines (∼24 nm), but the length is on the scale of the actuator (∼1 μm). To effectively couple the motion of the bead to the nanomachine,a highly stiff lever was designed that exhibits a persistence length of 22 μm, which allows nearly rigid mechanical coupling of microscale bead motion to nanoscale reconfiguration of the DNA device over lever lengths of $\sim 1 - 5$ μm. Magnetic manipulation of two prototype DNA origami nanomachines including a rotor system that can exhibit continuous rotational motion (Fig. 6.1A), and a hinge system that exhibits a finite range of angular motion (Fig. 6.1B) are demonstrated. This approach allows specific control over the angular conformation with resolution of ±4°, continuous rotational motion up to 2 Hz, and we confirmed the capability of applying up to 80 pN·nm/rad of torque.

6.2 Design of DNA Origami Systems

6.2.1 Design and fabrication of nanoscale components and microscale assemblies

Two prototype nanomachines were designed to demonstrate our manipulation capabilities, which are similar to previously published DNA origami devices. Our continuous rotational motion prototype machine, the nano-rotor (Fig. 6.1A), utilizes a rotor anchored to a platform by a flexible connector similar to a pin connection located at the center of the rotor so steric interactions force in-plane rotations. Specifically, the nano-rotor consists of three components: (i) a base platform, (ii) a 56 helix nano-brick that functions as the rotor arm, and (iii) a flexible pivot that connects the rotor to the base platform. Our finite angular motion prototype machine (Fig. 6.1B), the nano-hinge, design builds on previous hinge designs [182, 217, 218] with two arms connected along an edge via ssDNA linkers that enable relative rotation of the arms over a finite range of angles. Specifically, the nano-hinge designed in this study is constructed from two ∼40 nm long arms, each containing 36 dsDNA helices, which are connected at one edge by eight ssDNA linker connections to form the hinge joint. For actuation of these two prototype machines, a stiff mechanical lever was designed with the following primary design criteria: i) the length of lever arm should be $\geq$ 1 μm for compatibly with micro beads, and ii) the lever arm should be mechanically stiff to enable effective coupling of bead motion to the DNA nanomachines. Therefore, a large cross-section composed of 56 double-stranded DNA (dsDNA) helices bundled together to form a nano-brick with a large bending stiffness was chosen(Fig. 6.1C). This nano-brick was connected end-to-end to construct the mechanical lever (Fig. 6.1D). For both the nano-rotor and nano-hinge, the cross-section of the rotor or hinge arm components was specifically designed to enable connection to the lever arm.

Three assemblies for microscale actuation were developed(Fig. 6.2). First, the mechanical lever was directly actuated as a test system to quantify our manipulation capabilities in terms of position resolution, speed, and force. In actuating the mechanical lever, one of its ends is affixed to the substrate, and then a superparamagnetic bead is attached to the free

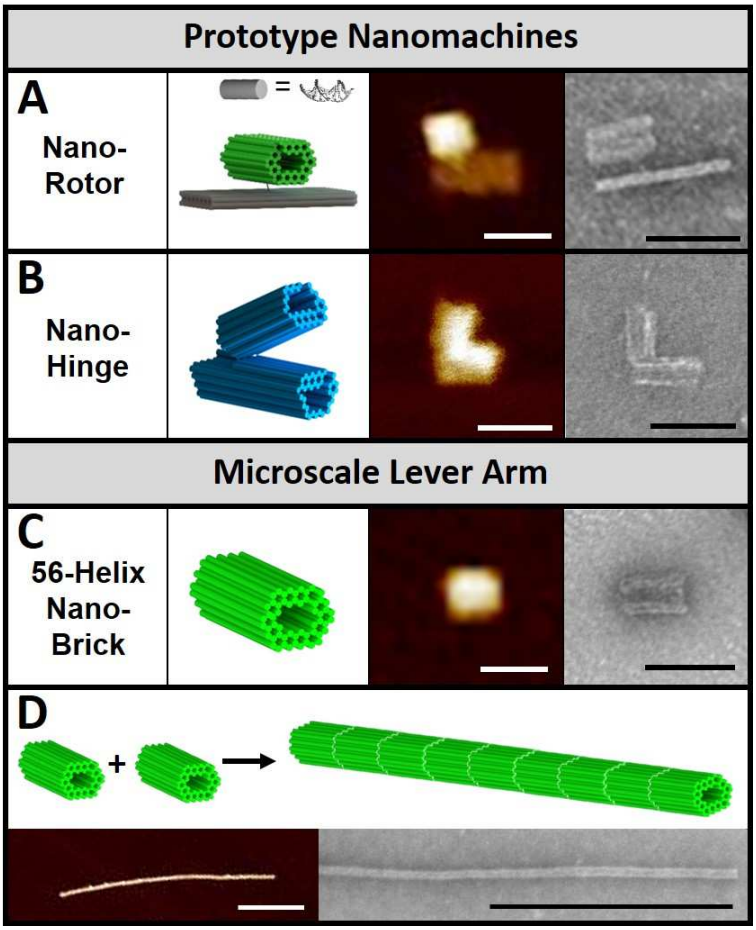

Figure 6.1: The Prototype nanomachines include (A) a nano-rotor composed of two separate nanoconstructs, the nano-brick and a nano-platform, which are connected together via ss-DNA overhang and (B) a nano-hinge consists of two stiff nano-rods with 36 double-stranded DNA (dsDNA) helices attached by 8 single-stranded DNA. Prototype nanomachines are actuated using the(C) 56-helix nano-brick composed of 56 dsDNA helices bundled together to form a nano-brick with a large bending stiffness. (D)The DNA mechanical lever arm for actuation is composed of a 1D array of nano-bricks connected via ssDNA. Cylindrical models are shown for each with each cylinder representing a DNA helix. AFM and TEM images are shown respectively with Scale bar 50 nm for images A-C and 500 nm for image D.

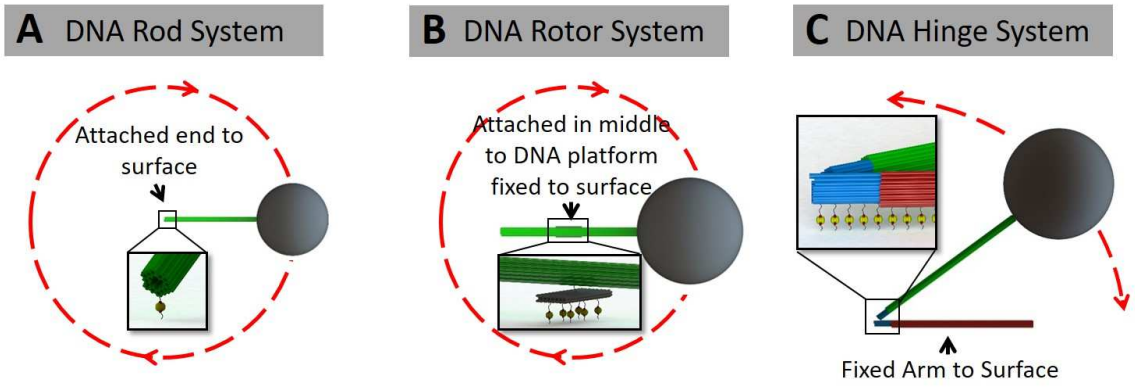

Figure 6.2: Schematic illustration of three DNA micosystems (A) DNA Rod System, (B) DNA Rotor System, and (C) DNA Hinge System – were assembled from DNA nanostructures to actuate three DNA nanoconstructs 56 Helix nano-brick, nano-rotor and nano-hinge. (A) The nano-rod was attached to the surface via biotin-streptavidin affinity while a micro-lever arm attached to the other end. (B) The nano-platform in the nano-rotor was attached to the surface via biotin-streptavidin affinity while two micro-lever arms were attached on both sides of the nano-rotor arm. (C) Two micro-lever arms are attached to the nano-hinge. One micro-arm of the hinge is fixed to the surface via biotin-streptavidin affinity while the other micro-arm is free to fluctuate. Micromagnetic beads are attached to the free end of the micro-lever arm in each system. Rotating in-plane fields apply a torque on the bead precessing the nano-rod and nano-rotor and opening and closing the nano-hinge.

end of the lever arm. Rotation of the lever arm can then be driven by a rotating magnetic field (Fig. 6.2A). In the case of the nano-rotor, two stiff levers are coupled to each end of the 56-helix rotor arm to form a micro-rotor. A magnetic bead was added to one of the free ends of the extended lever arm to enable rotation of the nano-rotor about the central pivot between the rotor-arm and nano-platform (Fig. 6.2B). Similarly, in the nano-hinge system, mechanical levers are connected to both of the nano-hinge arms to form a micro-hinge. One lever arm is fixed to the surface while the other is rotated by a magnetic bead attached to its end (Fig. 6.2C).

6.2.2 Assembly/Fabrication of Microscale Systems for Actuation

The microscale mechanical lever arm was constructed from a 1D array of nano-bricks connected in series via single-stranded DNA (ssDNA) strands which connected the right edge

of one nano-brick to the left edge of another (Fig. 6.3A). These ssDNA strands are referred to as polymerization strands. The lever arm was constructed in a channel by incubating purified nano-brick structures with polymerization strands at a concentration that was five times in excess of the structure concentration, which yielded stiff DNA origami lever arms ranging in length from ∼1 - 5 μm. The persistence length of the lever was characterized through analysis of shape fluctuations in TEM images as previously done for actin filaments [219] as well as compared to preliminary characterization done by tracking the bending fluctuations of levers confined in plane between two coverslips as previously done for actin filaments, microtubules, and amyloid fibers [220, 221]. The persistence length was determined by measuring the variance in transverse fluctuations from TEM images to be 22 ± 4 μm (mean ± standard deviation). This compares with the preliminary results of the TIRF images giving a persistence length to be 27 ± 19 μm (mean ± standard deviation).

The rotor was assembled by first connecting the platform to nano-brick (the rotor arm) via a single complementary ssDNA overhang (Fig. 6.3) and showed an attachment efficiency of ∼14% with 27% of nano-bricks and nano-platforms remaining unattached quantified by gel intensity analysis (Fig. A.5). Well-formed nano-rotors (i.e, nano-bricks attached to platforms) were purified via gel electrophoresis. Pre-assembled lever arms formed in a tube were then attached to the nano-rotor to form a micro-rotor by incubating the lever arms together with the nano-rotors, polymerization strands and lever arms at an 1 - 5 fold excess concentration relative to the nano-rotors(Fig. 6.3D). When attached to the surface in a channel, 3 - 6 fully formed micro-rotors on average were observed in an 80 μm by 80 μm window.

The final system, the extended hinge, was assembled by adding two levers to the nano-hinge to extend each arm to microscale lengths. The lever attachment was carried out in two steps. First, a single nano-brick was attached to the top and bottom arms of the nano-hinge through ssDNA strands that connect the ends of the hinge arms to the left end of a nano-brick. To allow specific attachment of a nano-brick to each arm, a different version of the nano-brick was constructed that has the same exact design, but the scaffold was shifted by 30 bases to change the sequences that are available for binding at the left edge

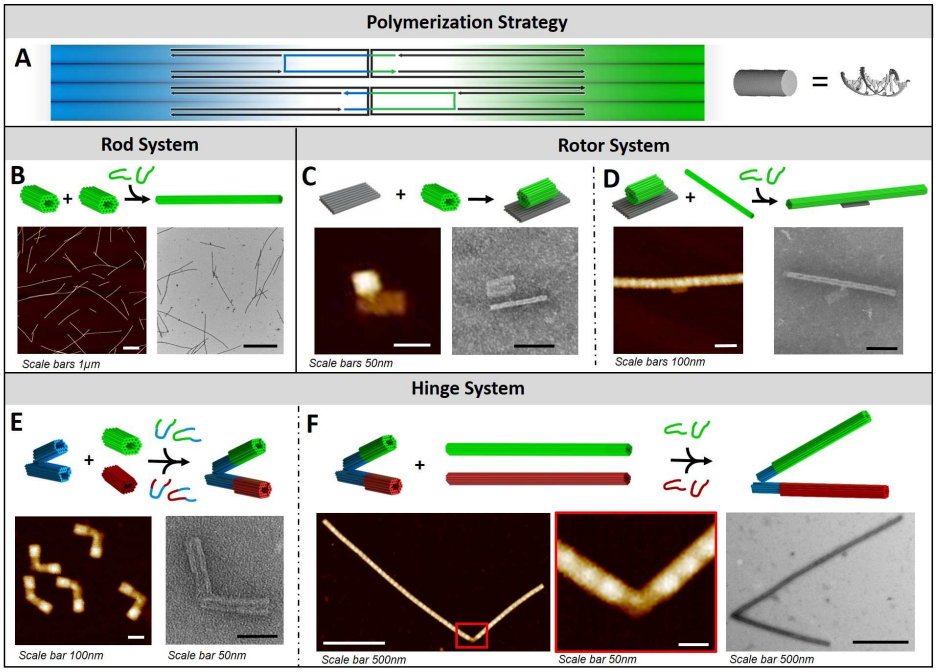

Figure 6.3: Assembly of Systems. (A) ssDNA connecting two structures (polymerization strands) were designed with a u-shaped motif where half have a higher affinity to attach to the end of one structure while the other half have a higher affinity to the opposite end of another structure. (B) Stiff micro-levers are assembled by attaching 56 helix nano-bricks end to end using polymerization strands. AFM and TEM images of micro-levers. Scale Bar, 1 μm. (C) The nano-rotor is assembled by attaching a nano-platform to a nano-brick via a single ssDNA overhang. AFM and TEM images of the nano-rotor construct. Scale Bar, 50 nm. (D) Stiff micro-levers are formed off the arm of the nano-rotor using polymerization stands to connect the nano-arm to the micro-lever. AFM and TEM images of polymerized nano-rotor. Scale Bar, 100 nm. (E) A single nano-brick is attached initially to the top and bottom of the nano-hinge using two separate sets of polymerization strands for top (green-blue) and bottom (red-blue). AFM and TEM images of the hinge with top and bottom nano-bricks attached. AFM image with Scale Bar, 100 nm and TEM image with Scale bar 50 nm. (F) Stiff micro-levers are formed off the initial nano-bricks by attaching top nano-rods (green) and bottom nano-rods (red) using two separate sets of polymerization staples for the top (green) and the bottom (red). Zoomed out image of AFM and TEM image of polymerized nano-hinge with Scale Bar, 500 nm. Zoomed in image of the nano-hinge from in the AFM image with Scale Bar, 50 nm.

of the nano-brick. The specific arm attachment is critical to define which arm is attached to the surface. This approach also decreases the number of steps needed to assemble the extended hinge system by allowing simultaneous attachment of the nano-bricks to the top and bottom arms of the hinge in the first step and concurrent attachment of top lever arm (composed of top nano-bricks) and bottom lever arm (composed of bottom nano-bricks). The initial nano-bricks were attached to the top and bottom arms of the nano-hinge by mixing them together in equal concentrations with excess polymerization strands for both nano-bricks shown in corresponding colors in Fig. 6.3E resulting in high yield of ∼27% attachment of nano-bricks to nano-hinges with less than 4% excess nano-bricks and nano-hinges remaining unattached as quantified by gel intensity analysis (Fig. A.6). When only a single nano-brick is attached to the nano-hinge the attachment efficiency is increased to 47% since there is no aggregation which is around 26% in the case of the attachment of both nano-bricks. This sample was gel purified to remove excess hinge-brick polymerization strands, so they would not interfere with subsequent attachment of the lever arms. The microscale lever arm extensions were subsequently added by incubating this assembly with pre-made micron length rods (Fig. 6.3F). This approach yielded micro-hinges with typical arm lengths of 1 - 5 μm with 2 - 5 micro-hinges attached to the surface in an 80 μm by 80 μm viewing window.

6.3 Magnetic Actuation

6.3.1 Actuation of Rod System

Each of the three systems was actuated using external magnetic fields provided by four orthogonal electromagnets and a solenoid. First, to quantify our actuation capabilities, the lever arm was directly actuated by attaching one end to a streptavidin functionalized cover-slip through a biotin-labeled strand on the structure and the other end to an anti-digoxigenin coated superparamagnetic bead via a digoxigenin-labeled strand on the structure. Complete and continuous 360° rotations of the lever were driven by applying a weak ($<$ 100 Oe) in-plane precessing magnetic field. A torque can be applied to superparamagnetic beads due

to the anisotropic component of the magnetization which rotates the bead in a precessing field. Earlier studies as well as results in Chapter 7 characterizing MyOne Dynabeads have shown that in low fields ($<$ 30 Oe) a small permanent moment has been measured [222], and in high fields ($>$ 150 Oe) and anisotropic component of the induced magnetization is manifested as an easy axis such that it is favorable to align in opposing directions along the axis [223]. Under bright-field, beads attached to lever arms tethered to the surface are readily confirmed from their circumferential motion since a detached bead would simply spin on its own axis. As illustrated in Fig. 6.4, it was thus possible to rapidly ($\sim$milliseconds) rotate the DNA nano-brick and to finely tune its speed of actuation up to rotation rates of 2 Hz with an in-plane precessing field of 40 Oe. For fields (40 Oe) rotating at frequencies beyond 2 Hz, due to their different magnetic content [223], most beads did not consistently maintain pace and track synchronously with the field. The inset in Fig. 6.4B displays the circumferential path from representative trajectories of a single bead attached to a lever and actuated at frequencies of 0.1, 0.5, 1 and 2 Hz for 10 seconds. Levers with lengths ranging from 0.5 μm to 2 μm were consistently actuated at these distinct frequencies. Even though the magnetic moments of each bead differ largely from bead to bead [223], the trajections vs time plot of the overlaid rotation rates for 17 individual beads with varying extension lever lengths demonstrates the reproducibility of each bead rotating synchronously with the field (Fig. 6.4B).

In addition to driving continuous rotation, it is also possible to hold the lever arm at a specific orientation by applying a constant in-plane magnetic field as shown in Fig. 6.4C. To quantify the corresponding position resolution, several lever arm constructs were magnetically restrained at four distinct angles under six different magnetic field strengths (10, 20, 30, 40, 50, and 100 Oe). An example of tracking the Brownian fluctuations of one bead linked to a lever arm constrained to a given position is shown in Fig. 6.4D. From the bead tracking which detects the center of the bead in each frame, the in-plane fluctuations were determined from the angular changes around the circumferential path of a tethered bead. Since the lever arm is relatively stiff, radial changes seen in the projects from the bead tracking were understood as out-of-plane fluctuations. The in- and out-of-plane fluctuations

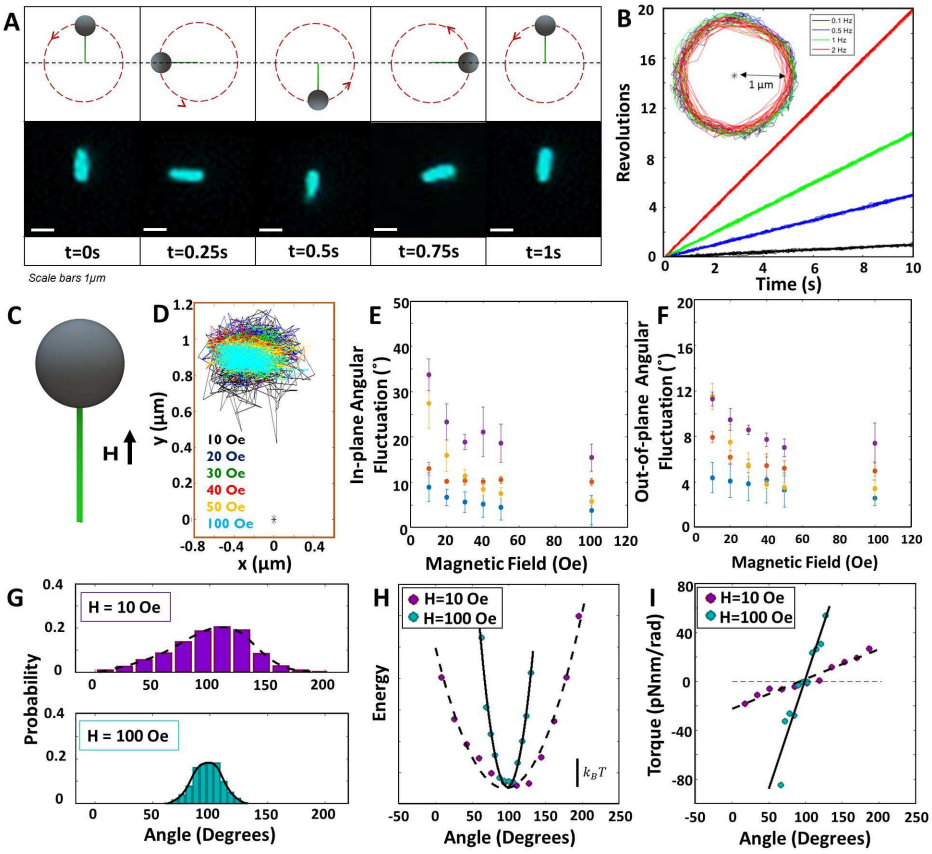

Figure 6.4: Actuation of Nano-brick. (A) TIRF images of nano-brick magnetically actuated via extension of the micro-lever arm attached to micromagnetic beads. Nano-brick is rotated by 360° with a frequency of 1 Hz and rotates by 90° every fourth of a second corresponding to video time frames at 0 s, 0.25 s, 0.5 s, 0.75 s and 1 s. (B) Nano-bricks were actuated at four different frequencies 0.1 Hz, 0.5 Hz, 1 Hz and 2 Hz (black, blue, green and red) with rotation rates overlaid for 17 different beads. Inset: Representative tracking of one microbead attached to the micro-lever. (C) External in-plane magnetic fields were applied in 4 orthogonal directions reorienting the nano-rod via the extended micro-lever labeled with a magnetic bead. (D) Representative tracking of the bead fluctuations in an in-plane external magnetic field oriented in the +y direction with strengths 10 Oe, 20 Oe, 30 Oe, 40 Oe, 50 Oe and 100 Oe (black, blue, green, red, yellow, and cyan). (E) The standard deviation of the in-plane fluctuations of 4 tethered beads decreases as a function of the in-plane external magnetic field. (F) The standard deviation of the out-of-plane fluctuations of the 4 tethered beads decreases as a function of the in-plane external field. For both E and F, each data point indicates the mean fluctuation and standard deviation of the 4 measured orientations for each bead. The orange data points correspond to the tracking shown in D. (G) The in-plane angular distribution of the bead shown in purple in E and F shows greater confinement at 100 Oe (cyan) compared to 10 Oe (purple). (H) The energy landscape assuming Boltzmann weighting was calculated from the probability distributions for the Bead at 10 Oe (purple) and 100 Oe (cyan). (I) The torque on the magnetic bead was calculated for the Bead at 10 Oe (cyan) compared to the bead at 100 Oe (purple) by differentiating the energy landscape.

of four different beads held at the four orthogonal positions were measured as a function of increasing field strengths (Fig. 6.4E-F). The fluctuations in both cases were more confined at higher field strengths. However, the degree of confinement varied from bead to bead, likely due to the differences of the anisotropic magnetic moment of each bead [223]. The standard deviation of the in-plane angular fluctuations for the 4 beads ranged from ± 36° to ± 9° at low fields (10 Oe) (Fig. 6.4E) with out-of-plane fluctuations between ± 11° to ± 4° (Fig. 6.4F). However, at larger fields (100 Oe), the Brownian fluctuations are more suppressed and the standard deviation of in-plane angular fluctuations decreased to lie between ± 15° to ± 4° with out-of-plane fluctuations between ± 7° to ± 3°. Therefore, magnetic actuation allows the lever arm, and ultimately other DNA nanodevices to be confined in-plane, via the lever arm, down to ± 4° and out-of- plane down to ± 3° with a 100 Oe field and hence be controlled to be positioned at ∼45 (=360°/8°) distinct angular orientations where each distinct orientation is two standard deviations apart. This approach provides an advantage over strand binding and displacement approaches [180, 182, 185], which are largely limited to switching between one well-defined conformation and another freely fluctuating state.

The extent of the Brownian fluctuations and spread in confinement angles also enables characterization of the strength of magnetic traps that localize the magnetic beads at a given field strength. For the bead corresponding to the data set shown in purple in Fig. 6.4E-F, the probability distribution was used to calculate the free energy assuming a Boltzmann probability distribution, and the angular variation of the free energy differentiated to determine the corresponding torque that acts to confine the bead (Fig. 6.4G-I) [182]. The spread in the probability distribution of the bead held at 10 Oe is greatly reduced when confined at 100 Oe in Fig. 6.4G. By increasing the magnetic field strength the trap stiffness can be tuned as evident in the narrowing of the potential well (Fig. 6.4H). The larger magnetic field provides a greater torque to confine the beads (Fig. 6.4I).

6.3.2 Actuation of Rotor System

A similar framework was used to actuate the first prototype nanomachine, the nano-rotor. Nano-rotor constructs with the rotor extended by lever arms were immobilized to a glass

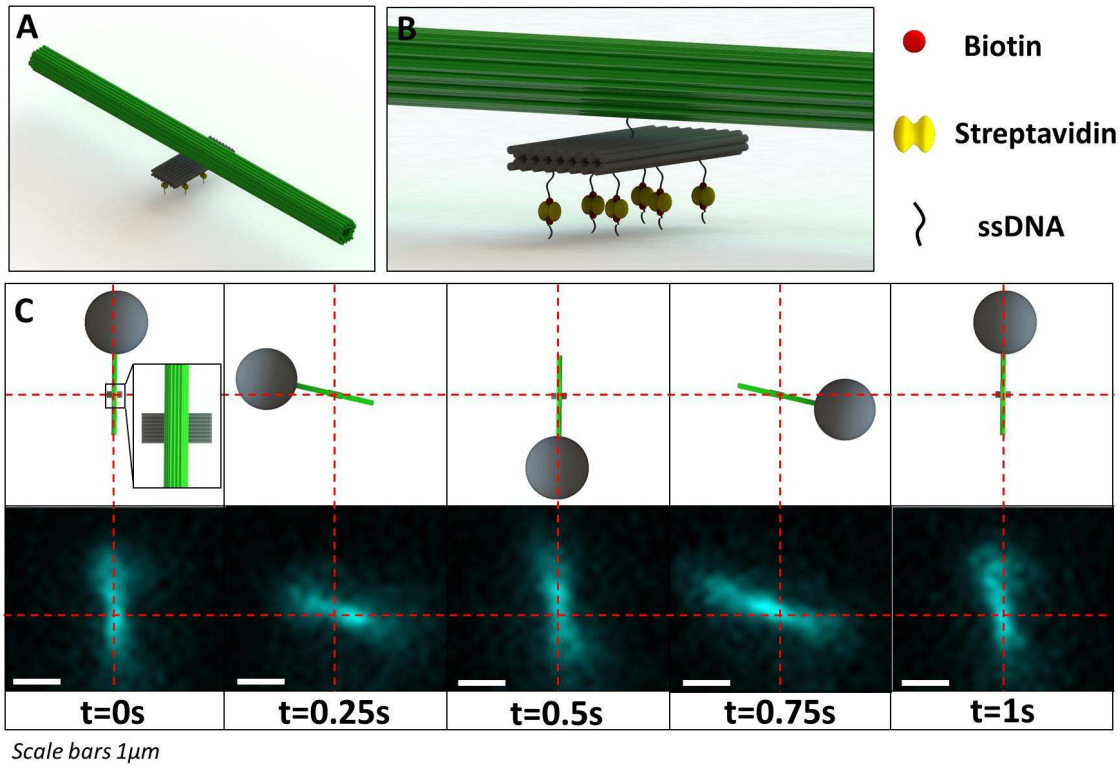

Figure 6.5: Rotation of Nano-rotor . (A) Schematic of nano-rotor (nano-platform (gray) attached to nano-brick (green) with fully extended arms (green). (B) Nano-platform attached to surface via biotin streptavidin.. (C) TIRF images of nano-rotor magnetically actuated in a flow channel using the extension of micro-lever arms attached to micromagnetic beads. Nano-rod is rotated by 360° with a frequency of 1 Hz and rotates by 90° every fourth of a second corresponding to video time frames at 0 s, 0.25 s, 0.5 s, 0.75 s and 1 s.

coverslip via biotin-labeled strands attached to the bottom of the platform (Fig 6.5A-B). Superparamagnetic beads were added to the ends of the lever arm via a digoxigenin-labeled strand at the end of the lever that binds to an anti-digoxigenin coated bead. By applying a weak (40 Oe) in-plane precessing magnetic field, the rotor pivots about the attachment point to the platform and rotates through 360° as illustrated in Fig. 6.5C. The rotor system, similar to the nano-rod, was also actuated at several distinct frequencies up to 2 Hz. The rotor system could, as in the rod system, be held at 45 distinct angular orientations each separated by 8° (two standard deviations apart).

6.3.3 Actuation of Hinge System

To enable actuation of the nano-hinge, the lever arm extension on the bottom arm was attached to a coverslip surface via biotin-labeled ssDNA strands on the side of the fixed arm of nano-hinge so the opening and closing of the hinge occurred parallel to the plane of the coverslip (Fig. 6.6A-B). The fixed lever arm was added to the hinge to allow for easy visualization of the opening and closing of the hinge. The lever arm extension on the mobile hinge arm was functionalized with a magnetic bead to open and close the hinge using in-plane external magnetic fields as shown in Fig. 6.6C. To estimate the torque required to open or close the hinge, the angular distribution of nano-hinges in the absence of a magnetic field were measured from TEM image analysis. The angular conformations range from ∼10° to 165° (Fig. 6.6D). A Gaussian distribution fit to the data suggests the equilibrium angle of the hinge is 74° ± 30° (mean ± standard deviation). The free energy was calculated from the probability distribution assuming a Boltzmann distribution (Fig. 6.6E) and the torque required to open and close the hinge was calculated from the angular variation of the free energy (Fig. 6.6F). These results show that the torque needed to open or close the hinge (e.g. 15 pN·nm/rad) is smaller than the magnetic torque (e.g. 20 pN·nm/rad) supplied by the bead attached to an extended lever arm in a low external field (10 Oe) as shown in Fig. 6.4I. Therefore, the hinge can be actuated with applied magnetic fields as low as 10 Oe. Direct magnetic actuation revealed the hinge can be opened beyond 90° in agreement with the TEM angular distributions (Fig. 6.6D). As in the nano-brick and -rotor systems it was further confirmed that the hinge can be opened and closed at distinct frequencies. From the in-field confinement determined from the fluctuations of a bead linked to a lever, at the high fields of 100 Oe, the nano-hinge could be held ∼20 (=160°/8°) distinct orientations (two standard deviations apart).

6.4 Conclusion and Discussion

This work demonstrates an integrated approach to control DNA nanodevices by combining hierarchical assembly of distinct nanoscale DNA origami constructs into microscale assem-

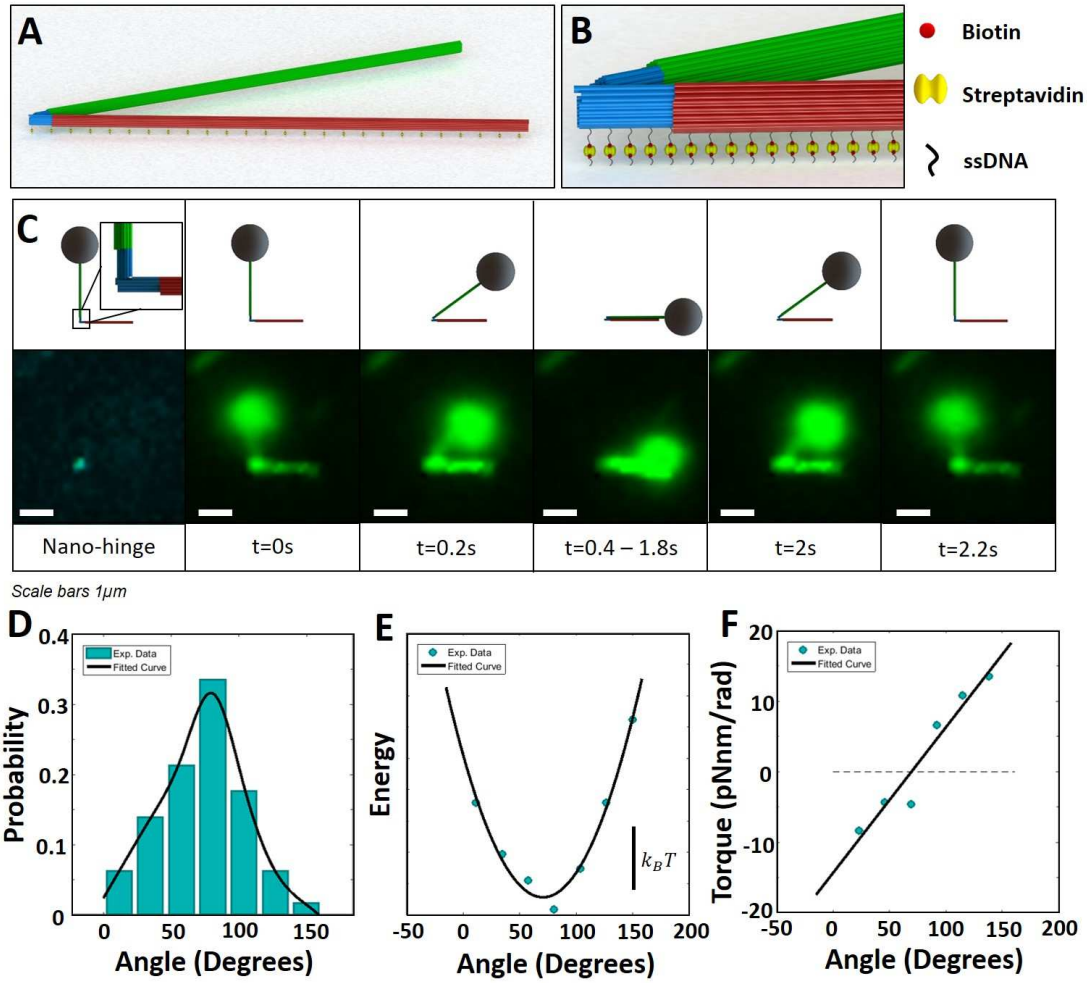

Figure 6.6: Rotation of Nano-hinge. (A) Schematic of nano-hinge (blue) with extended free arm (green) and fixed arm (red) to the surface via biotin and streptavidin. (B) Close up showing surface attachment. (C) TIRF images of nano-hinge magnetically opened and closed in a flow channel using the extension of micro-lever arms attached to micromagnetic beads. Nano-hinge was labeled with Alexa 488 and confirmed at the end of the extended arms labeled with Alexa 555. Video time shots of the hinge closing (0, 0.2, 0.4 seconds) and reopening (2, 2.2 seconds) such that the hinge was left closed from 0.4 s - 1.8 s before being reopened. (D) The angular distribution of static hinges measured from TEM shows a preferred angle of being open at 74° with an ability to open to 165°. (E) The energy landscape assuming Boltzmann weighting was calculated from the probability distributions. (F) The torque required to hold each hinge at a specific angle was calculated by differentiating the from the energy landscape.

blies that can be functionalized with micron-sized magnetic beads for direct manipulation via an externally applied magnetic field. Critical to this approach is the ability to effectively couple the microscale motion of the bead to the nanoscale reconfiguration of the DNA nanodevice. To achieve effective coupling, a highly stiff microscale mechanical lever arm with a persistence length of 22 μm was designed. The lever arm was constructed as a linear array of DNA origami nanostructures so the cross-section can be matched to a DNA origami device. While DNA is generally a flexible polymer, bundling many dsDNA helices into the cross-section yields a filament with bending stiffness comparable to actin, a structural polymer [220].

Here we focused on driving rotational motion which allows relatively large movement of micromagnetic beads to be de-amplified to mobility on the scale of the nanomachines via the mechanical lever arm. For example, with a 1 μm lever arm, which was a typical length for our assemblies, the position of the bead was held within a standard deviation of $\pm 4^{\circ}$. Given the length of the original nano-hinge (Fig. 6.1B) arms of 40 nm, this suggests our current direct manipulation assemblies could control the position of molecules with $\pm$ 5 nm resolution at the ends of the nano-hinge arms, or even more accurately if the molecules were positioned closer to the vertex. This is comparable to the typical position resolution of molecules statically immobilized on DNA origami nanostructures [156]. One recent study demonstrated the ability to position molecules with angstrom-scale resolution using a DNA origami structure, but this structure was static [218]. Here the ability to directly manipulate DNA origami nanodevices with nanometer scale precision with sub-second response times and torques ranging from $\sim 20 - 80$ pN·nm/rad at magnetic fields of $\sim 10 - 100$ Oe has been demonstrated.

In particular, continuous rotational motion of a nano-rotor and oscillating opening and closing of a nano-hinge up to frequencies of 2 Hz was driven by external magnetic fields. For continuous rotation up to 750 radians of rotation was achieved, which corresponds to 750 μm of bead motion for a 1 μm lever arm. The total amount of rotation could easily be increased but was limited in this study just based on the experiment time. The angular rotational space of the rotor is characterized by 45 distinct conformations with little overlap

in the fluctuations (i.e. separated by one standard deviation on either side). The opening and closing of the hinge were characterized by 20 similarly defined distinct conformations. Such well-defined hinge conformations clearly illustrate the advantage of direct manipulation via a magnetic torque relative to previously established approaches that typically actuate between one fixed and one freely fluctuating state [182, 185] or between a few stable states [180]. In addition, previous approaches are typically limited to actuation response times on the scale of minutes or greater [154, 182, 188]. One previous study demonstrated actuation response time of ∼10 seconds based on temperature changes [185], while another quantified inherent conformational dynamics of DNA origami nanodevices at sub-second timescales [224]. This present work is the first demonstration of actuation with direct control over a large range of conformations achieved with sub-second response times.

Given recent advances in DNA origami nanotechnology, the manipulation capabilities established here could be integrated into applications ranging from control of chemical reactions to manipulation of protein complexes. For example, recent studies have used DNA origami hinge or tweezer-like devices to control enzyme function by bringing an enzyme and co-factor together [225], to probe the conformation and stability of nucleosomes [217], or to detect biomolecules in solution via structure closing [176]. The ability to manipulate similar DNA origami devices via magnetic actuation could improve capabilities to control, study, and detect biomolecular interactions in real-time. In addition, our magnetic actuation approach is amenable to control more complex devices [182], which serve as a foundation for nano or microscale robotic systems based on DNA origami assemblies.

Chapter 7

Field-Dependent Strength and Orientation of Superparamagnetic Bead Magnetization

Great advances in nanotechnology have been realized through the ability to finely control the spatial and temporal movement of micro- and nano-actuators using superparamagnetic beads. These actuators have been especially useful in bio and medical technologies where magnetic fields can directly apply femto and picoNewton forces. For example, detection [226] and medical diagnosis and treatments [227–229] have emerged using superparamagnetic microbeads including drug delivery [30] and gene transfection [22]. By studying single rotating beads and chains of beads [230–232], the viscoelastic properties of fluids [233, 234] and intracellular environments have been studied [235, 236]. Cells have also been transported and manipulated through their attachment to micromagnetic beads [11, 12, 96, 237]. Furthermore, magnetic beads have found use in separation and isolation of cells and DNA [7, 15, 238–244]. Advancements have also been made in microfluidic devices such as micropumps that rely on magnetic beads [245–247]. Additionally, even microconstructs and lattices have been assembled and manipulated using magnetic beads [108, 110, 248–257].

Despite these range of applications, the nature of the magnetization of microscopic superparamagnetic beads has not been fully investigated. To quantify the torque on superparamagnetic beads in precessing external magnetic fields, it is important to understand

how the individual magnetic dipoles within a bead respond to the changing magnetic fields. The magnetic moment of a superparamagnetic bead is created by an ensemble of individual dipoles (typically iron oxide nanoparticles) dispersed in the bead. The range of magnetic relaxation times of each individual dipole (permanent and induced) leads, in general, to two distinct responses in the magnetization of the bead. When the magnetic dipole relaxation time (τ_m) is fast relative to the time associated with the frequency (f) of the external magnetic field ($\mathbf{H}$)($\tau_m \gg \frac{1}{f}$), the dipoles reorient rapidly to align with $\mathbf{H}$ leading to a field-dependent induced moment ($\mathbf{m}_i$). However, when τ_m is slow relative to the change in $\mathbf{H}$ ($\tau_m \ll \frac{1}{f}$), the entire bead rotates in order to align the ensemble of dipoles with the magnetic field and thus responds as a permanent moment ($\mathbf{m}_p$) [222, 258–260].

Therefore, in general, the net moment ($\mathbf{m}$) results from the contributions of both the induced moment ($\mathbf{m}_i$) and permanent moment ($\mathbf{m}_p$) ($\mathbf{m} = \mathbf{m}_i + \mathbf{m}_p$). For low fields ($\mathbf{H} <$ 30 Oe), the contribution from $\mathbf{m}_i$ is small, and in this case, the torque is mainly due to $\mathbf{m}_p$. For $\mathbf{H} \sim 150$ Oe when generally $\mathbf{m}_i > \mathbf{m}_p$, the anisotropy from the nanoparticles creates an easy axis which is energetically more favorable to align with the field. The easy axis is ″pi periodic″ [223] such that alignment is favorable along two directions oriented 180° from one another. The results from Ref. [223] showed that $\mathbf{m}_i$ consists of an isotropic contribution ($\mathbf{m}_{ii}$) which is aligned with $\mathbf{H}$ and an anisotropic component ($\mathbf{m}_{ia}$). In contrast to the low field case, at higher fields, while the contribution of $\mathbf{m}_p$ still prevails, $\mathbf{m}_{ia}$ begins to contribute greatly to the torque on the bead. The net torque can also be considered in terms of its anisotropic magnetic moment ($\mathbf{m}_a = \mathbf{m}_p + \mathbf{m}_{ia}$) in a uniform field while its isotropic contribution ($\mathbf{m}_{ii}$) only contributes to the strength of the moment.

Early studies exploring the permanent moment ($\mathbf{m}_p$) [222, 258–260] or anisotropic contribution $\mathbf{m}_{ia}$ [223] have focused on either the low ($<$ 30 Oe) or high ($>$ 150 Oe) field regime where the combined effects of both moments have not been simultaneously observed. Furthermore, due to the difficulty of tracking the rotational orientation of individual spherically symmetric beads, measuring the permanent and induced moments separately is challenging. Therefore, single bead rotation measurements have not been conducted for systems such as MyOne Dynabeads. Although the permanent moment ($\mathbf{m}_p$) may be estimated in experi-

ments on rotating dimers [222], the anisotropic component of the induced moment ($\mathbf{m}_{ia}$) is not easily observed in dimer-based measurements due to the dominance of inter-bead dipole interactions.

In this study, these difficulties are overcome by attaching a single bead to a microscopic lever arm such as a stiff DNA rod and the strength and orientation of both $\mathbf{m}_p$ and $\mathbf{m}_{ia}$ is investigated for individual beads in external fields ($\mathbf{H}$) lying between 10 Oe and 100 Oe. In this case, the character of the dominant moment ($\mathbf{m}_p$ or $\mathbf{m}_{ia}$) is determined as a function of an in-plane external field ($\mathbf{H}_{XY}$) from the response of the DNA rod-tethered bead when $\mathbf{H}_{XY}$ is reversed. The magnitude of the moment is measured from its dynamics in an in-plane rotating field ($\mathbf{H}_{XY}$) while its orientation deduced from the response in a constant $\mathbf{H}_{XY}$. At low fields ($\mathbf{m}_p > \mathbf{m}_{ia}$), the bead will orient along a unique direction with respect to $\mathbf{H}_{XY}$. However as $\mathbf{H}_{XY}$ is increased, the anisotropic component of the induced moment begins to dominate ($\mathbf{m}_{ia} > \mathbf{m}_p$) and the tethered bead remains in the same position for field orientations differing by 180°. Such pi periodicity is thus displayed due to the easy axis of $\mathbf{m}_{ia}$. Furthermore, the magnitude and direction of the net moment are tuned with increasing $\mathbf{H}_{XY}$. These results point to the field-dependent competition between $\mathbf{m}_p$ and $\mathbf{m}_{ia}$ which provides for a previously unreported approach to investigate the field dependence of the magnetization of individual beads.

7.1 Background

7.1.1 Model of Single-Domain Nanoparticles in an External Field

Superparamagnetic beads contain a distribution of non-uniform, single-domain nanoparticles (e.g. iron oxide) embedded in a polystyrene matrix [111]. The effect of the applied field ($\mathbf{H}$) on individual dipoles from the embedded nanoparticles can be described by the Stoner Wohlfarth (SW) model [261]. In the SW model, the magnetization ($\mathbf{m}$) of the dipole for one of these individual nanoparticles does not change magnitude as $\mathbf{H}$ is varied and its orientation is determined by the competition between the energy to align along a preferred direction due to the anisotropy of the particle and the energy to align with $\mathbf{H}$. The free

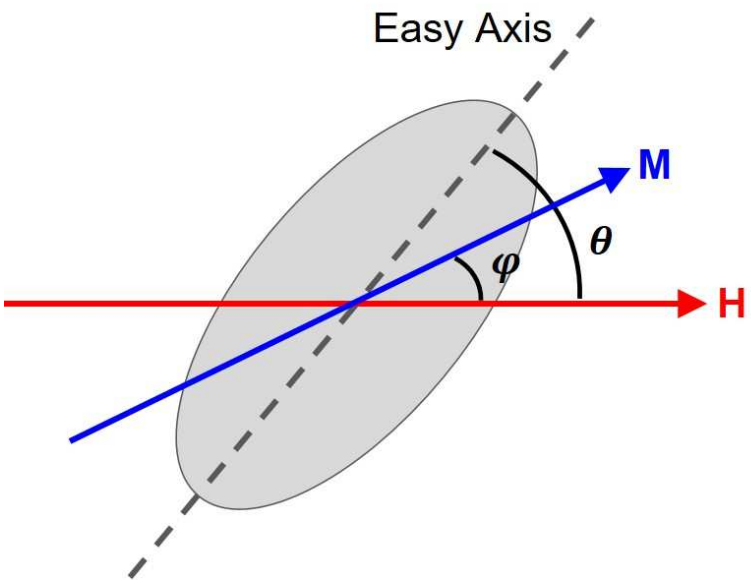

Figure 7.1: A single nanoparticle has an easy axis due to shape anisotropy. Therefore the magnetic moment of the individual nanoparticle will rotate to align with the easy axis and the field depending on the strength of the field and the anisotropy constant.

energy of the nanoparticle is thus:

$$E = KVsin^2(\phi - \theta) - \mathbf{m}\mu_0\mathbf{H}cos(\phi) \tag{7.1}$$

where K is the anisotropy constant, V the nanoparticle volume, ϕ and θ respectively the angle between $\mathbf{m}$ and the easy axis to the field ($\mathbf{H}$) (Fig. 7.1). The first term in the free energy is the penalty for misalignment of the magnetic dipole whereas the second term describes the preference of the moment to align with $\mathbf{H}$. The dipole will orient at the angle which will minimize its free energy.

At low fields ($\mu_0\mathbf{H} \ll KV$), the moment will strongly align with the easy axis ($\phi \simeq \theta$) independent of the direction of the field. In this case, the moment will experience a torque due to the misalignment of $\mathbf{m}$ and $\mathbf{H}$ given by:

$$\tau = \mu_0\mathbf{H}sin(\theta) \tag{7.2}$$

In the high field limit ($\mu_0\mathbf{H} \gg KV$), the moment will align with the field and thus $\mathbf{m}$ will

not experience a torque due to **H** but instead responds to a torque due to its misalignment with the easy axis given by:

$$\tau = KVsin(2\theta) \tag{7.3}$$

Since alignment with the easy axis is uniaxial, the maximum torque would occur at $\theta = 45°$ independent of **H**. Between these low and high field extremes, **m** will align between the field direction and the easy axis at an angle that minimizes the free energy. Its orientation will thus change with field strength and the angle (θ) between **H** and the easy axis.

In this case, a torque is experienced by the dipole due to particle anisotropy. However, dipole-dipole interactions of interacting isotropic nanoparticles within anisotropic clusters would also display an easy axis and cause a torque on the cluster. For example, if two isotropic nanoparticles are in near proximity such that the dipoles interact, an effective anisotropy axis results from the individual moments tending to align with one another.

7.1.2 Magnetization and Magnetic Torque on Superparamagnetic Beads

The vector sum of the individual magnetization from each iron oxide particle within the bead determines the net magnetization of the superparamagnetic bead. In low fields (typically < 100 Oe), the induced magnetization ($\mathbf{m}_i$) is given by:

$$\mathbf{m}_i = \chi V \mathbf{H} \tag{7.4}$$

where χ is the susceptibility and V the volume of the magnetic material in the bead. At higher fields, $\mathbf{m}_i$ will begin to saturate.

The magnetic relaxation time of each individual nanoparticle depends on its size and anisotropy energy barrier (KV). From the characterization of the magnetic anisotropy constant for Fe_2O_3 particles as a function of the particle diameter [112], $KV \approx 1.5$ - $3.5\ k_BT$ at room temperature for particles with diameters between 8 nm to 22 nm. The magnetic dipoles can be categorized as Neel or Brownian dioples depending on their relaxation times: (1) Neel dipoles which have relaxation times longer than the average time between magnetization reversals (i.e. the Neel relaxation time) and (2) Brownian dipoles which have

relaxation times shorter than the Neel relaxation time [260]. The Neel dipoles rapidly reorient due to their relatively fast relaxation time and are best understood by a time average of the magnetic moments due to the stochastic reorientations of each individual dipole. The resulting Neel induced magnetization is field dependent (see equation 7.4). Furthermore, it is frequency-dependent, such that at frequencies > 100 Hz the magnetization is unable to reorient fast enough to align with the field - thus causing the magnetization to have a time delay (lag) with respect to the field. This delay can be accounted for by a complex frequency-dependent susceptibility in which the imaginary part is only significant at frequencies above hundreds of Hz [222, 258–260]. The Brownian dipoles often result from larger nanoparticles or clusters of particles that behave as permanent moments due to their slow relaxation times and are independent of the applied field.

The torque experienced by the bead is given by the vector sum of the torques on the individual nanoparticles or clusters of nanoparticles. Due to their distribution within the bead, large parts of this torque cancel. However, with the anisotropy of a finite number of individual or clusters of nanoparticles, a net torque would result and the bead would have an easy axis or preferred magnetic orientation which would cause the bead to rotate to align with $\mathbf{H}$. The torque is therefore due to a permanent moment ($\mathbf{m}_p$) from a finite number of aligned Brownian dipoles and an anisotropic induced moment ($\mathbf{m}_{ia}$) arising from a finite number of aligned Neel dipoles in an applied field.

7.2 Experimental Details

The principal design of this experiment involved attaching the microbead to a stiff DNA microrod assembled from smaller DNA nanostructures as discussed in Chapter 6. One end of the stiff microrod is fixed to the surface (pivot) and the other end bound to the superparamagnetic bead. In-plane magnetic fields were then applied and the bead monitored as it rotated about the surface pivot site to align with the magnetic field. If untethered to the DNA rod, the bead would simply spin in place with the resulting changes in orientation of the microscopic bead made harder to monitor and track.

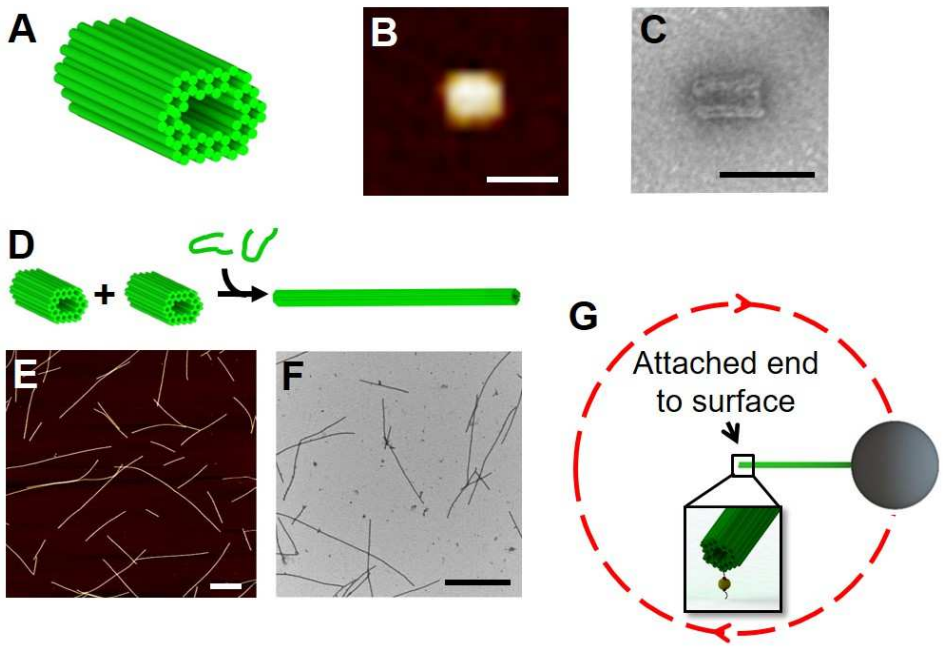

Figure 7.2: (A) The nano-brick (also called the 56hb) is composed of 56 dsDNA bound together in a honeycomb lattice with a central cavity. The AFM (B) and TEM (C) images of the 56hb. Scale Bar 50 nm. (D) The 56hb are attached end to end using 17 ssDNA that bind the right end of the 56hb to the left end of another 56hb to form a long stiff micron length rod. The AFM (E) and TEM (F) images of the polymerized microrod. (G) In the channel one end of the rod is attached to the surface while the other end is attached to the superparamagnetic bead. In a planar precessing field the bead will rotate around the surface attachment site.

7.2.1 Assembly of Stiff DNA Microrod in Channels

The DNA microrod was assembled from the DNA nanostructure (56 helix bundle (hb)) described in Chapter 6 and shown in Fig. 7.2. This structure is composed of 56 dsDNA connected together to form a cylinder with a central cavity. The 56hb is polymerized using 17 ssDNA which bind the right end of the 56hb to the left end of another 56hb. Although the polymerization process can easily be achieved in a tube, the resulting microrods do not readily attach to the surface since it is not as entropically favorable to fix one end of the microrod in place using a single biotin protein. Therefore, the microrod was self-assembled in channels using a surface polymerization process.

An important parameter in achieving a high yield of attachment of microrods to the

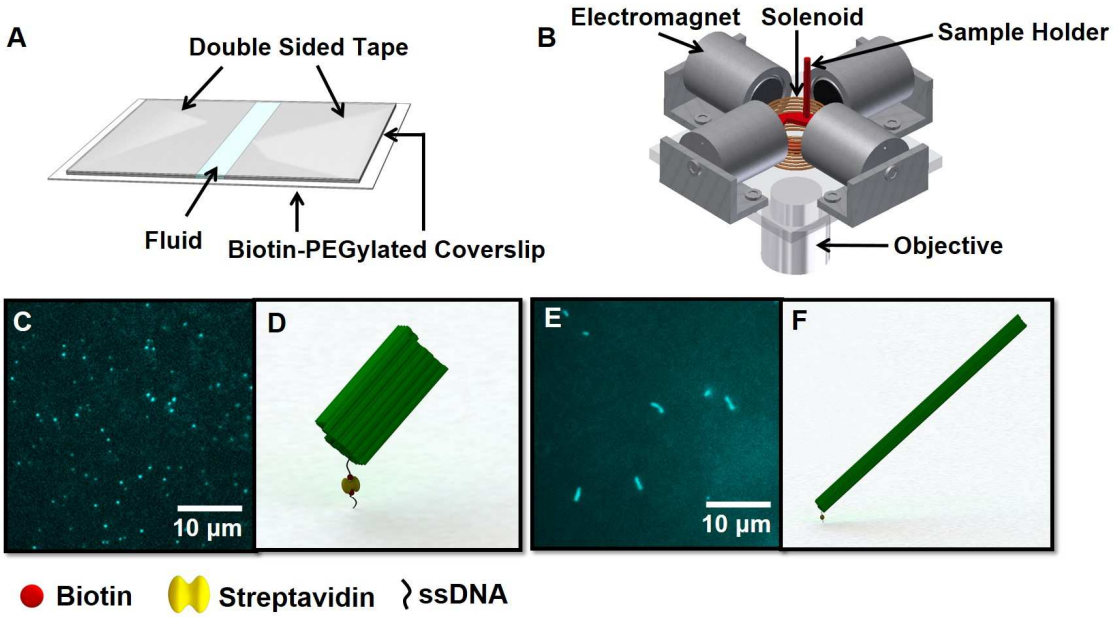

Figure 7.3: (A) Schematic of the channel formed by double sided tape and Biotin-PEGylated coverslips. (B) Schematic showing the magnetic set up for an inverted microscope. ((C-F) Formation of microrods in channel. (C) TIRF Image of fluorescently labeled nano-bricks and (D) schematic of a nano-brick attached to the surface. (E) TIRF image of fluorescently labeled microrods and (F) schematic of microrod attached to the surface.

channel surface was using a treated surface which reduced nonspecific binding. At first, KOH cleaned coverslips were used. However, this treatment method was not always reproducible and led to inconsistent yields in the attachment of structures. Using pegylated biotin slides, nonspecific binding was consistently reduced. The process to make pegylated biotin slides (described in detail in Section 3.4.2) involves initial slide cleaning using piranha, a silanization of the slides and finally pegylation using PEG and bi-functionalized Biotin-PEG.

Two strips of double sided tape formed the channel edges and connected two coverslips to form the top and bottom of the channel (Fig. 7.3A). Free streptavidin at 0.1 mg/mL concentration mixed with 0.1 mg/mL Bovine Serum Albumin (BSA) to further reduce non-specific binding was flowed into the channel and incubated for 5 minutes to allow attachment to the biotin on the surface. The excess streptavidin was washed out of the channel before

the initial 56hb with a single biotin overhang on the end was introduced and incubated for 10 minutes to ensure complete attachment to the streptavidin on the surface (Fig. 7.3C and D). Excess 56hb were washed out of the channel and the surface polymerization mixture flowed in. This mixture is composed of gel purified 56hb with two digoxigenin overhangs on the end (normal concentration 5nM), polymerization and neighbor staples in 5x excess to the structure, 15mM $MgCl_2$ and 0.2% NP40 (a detergent). The channels were placed in sealed containers with a reservoir of double distilled water (ddH_20) to prevent evaporation from the channel and incubated for 18 - 20 hours at 37°C. The microrods that formed using the surface polymerization process (Fig. 7.3E and F) were generally shorter compared to those created by polymerization in the tube.

The microrods were imaged in the channel using Total Internal Reflection Fluorescence (TIRF) (Fig. 7.3E). Each 56hb composing the rod had 5 fluorophore overhangs that could bind to ssDNA with ends functionalized either with Alexa 488, Alexa 555 or Alexa 647 fluorophores. In these experiments, the fluorophores were attached to the structures in the channel by flowing in 10 nM ssDNA functionalized with Alexa 488 fluorophore and incubating 4 minutes. The excess fluorophore strands were then washed out and the channels imaged on the microscope.

After confirming surface polymerization, MyOne superparamagnetic beads functionalized with anti−digoxigenin were attached to the microrods in the channel. To reduce nonspecific binding of the beads to the surface 1 mg/mL of casein (a surface protein blocker discussed in Section 3.4.4) was introduced into the channel and incubated for 10 minutes. The excess casein was removed and the beads flowed in at 50x dilution to stock concentration and incubated for 5 minutes. The excess beads were then washed out. Lastly, the channel was sealed on the ends with nail polish to prohibit evaporation during the experiments.

7.2.2 Magnetic Setup

The magnetic setup for actuation was composed of four electromagnets which provided in-plane magnetic fields and one solenoid which supplied the out-of-plane field (Fig. 7.3B). This setup was designed for an inverted microscope in order to acquire TIRF images of

the DNA rods during actuation. In this setup the sample rested within the solenoid. Due to space limitation on the inverted microscope, small electromagnets (1.25 inches long, 1.25 inches in diameter, OP-1212, Magnetech Corp) were used which limited the magnetic field range that could be reached. Therefore, most experiments were implemented on the upright microscope with larger electromagnets (2.5 inches long, 2 inches in diameter, OP-2025, Magnetech Corp). Confirmation of attachment of beads to the DNA rods could be established through fluorescence as well as by observing the rotation of the beads in bright-field.

7.3 Alignment of Bead Anisotropy Axis with DNA Rod

Prior to exploring the field-dependence of the bead magnetization, the alignment of the bead's magnetic anisotropy axis with respect to the DNA rod and its role in influencing the position of the bead under $\mathbf{H}_{XY}$ must be understood. The anisotropic component of the magnetization ($\mathbf{m}_a = \mathbf{m}_p + \mathbf{m}_{ia}$) rotates the entire bead to align its anisotropy axis with $\mathbf{H}_{XY}$. In cases when this axis and the DNA rod are parallel, the bead relocates in the direction of $\mathbf{H}_{XY}$ and the rod orients to lie parallel to $\mathbf{H}_{XY}$ (Fig. 7.4B). Fig. 7.4A shows the thermal fluctuations of such a bead held at four different positions with $\mathbf{H}_{XY} =$ 100 Oe. Since anti-digoxigenin is uniformly distributed on the bead surface for attachment to the DNA rod, the bead anisotropy axis will not necessarily always lie parallel with the microrod. Therefore, the radial line from the pivot to the position about which the bead fluctuates in the presence of $\mathbf{H}_{XY}$ does not always align with $\mathbf{H}_{XY}$. Fig. 7.4C shows an example of the thermal fluctuations of a different bead when held at four different positions with $\mathbf{H}_{XY} = 100$ Oe. In this case since $\mathbf{m}_a$ is not oriented parallel to the rod, the DNA rod will thus not orient parallel to $\mathbf{H}_{XY}$ but instead rotates to allow $\mathbf{m}_a$ to align with $\mathbf{H}_{XY}$ (Fig. 7.4D). These two examples showcase situations when $\mathbf{m}_a$ and the rod lie both in-plane. Moreover, the anisotropy axis could also lie out-of-plane such that the bead would have to move out-of-plane to align $\mathbf{m}_a$ with $\mathbf{H}_{XY}$.

When analyzing the bead fluctuations, such orientation effects must be taken into ac-

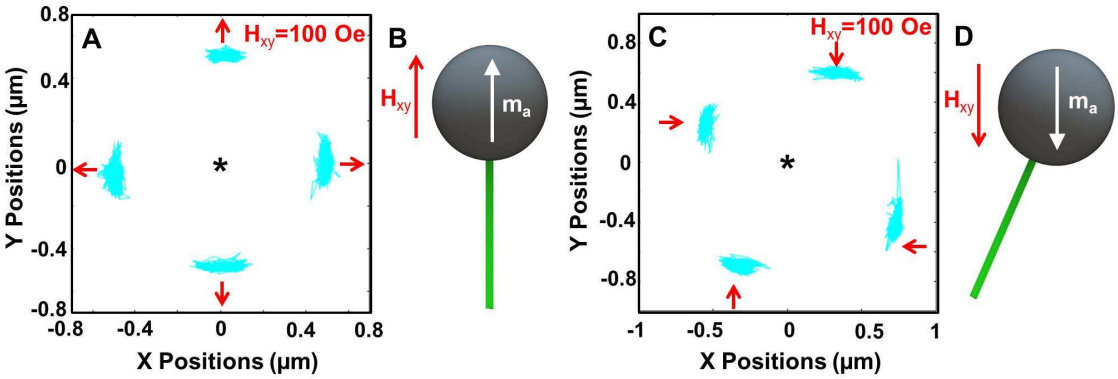

Figure 7.4: (A,B) Anisotropic magnetization ($\mathbf{m}_a = \mathbf{m}_p + \mathbf{m}_{ia}$) along the bead's anisotropy axis is aligned with the DNA rod. (A) Tracking of a single bead held at four different orientations with $\mathbf{H}_{XY} = 100$ Oe (direction indicated by red arrows at each position). The rod-surface attachment site where the bead pivots is marked by the black asterisk. (B) Schematic of a tethered bead attached to DNA rod which lies parallel to $\mathbf{H}_{XY}$ (red) and $\mathbf{m}_a$ (white). (C,D) Anisotropic magnetization ($\mathbf{m}_a$) along the bead's anisotropy axis is not aligned with the DNA rod. (C) Tracking of a single bead held at four different orientations with $\mathbf{H}_{XY} = 100$ Oe (direction indicated by red arrows at each position). The rod-surface attachment site is marked by the black asterix. (D) Schematic of a tethered bead attached to DNA rod which is not parallel with $\mathbf{H}_{XY}$ (red) and $\mathbf{m}_a$ (white).

count. Two possible alternative methods could be implemented to better align the bead anisotropy axis and rod orientation to lie in-plane and thereby reduce the out-of-plane movement of the bead. In the first method, by introducing beads into the channel in the presences of $\mathbf{H}_{XY}$, $\mathbf{m}_a$ would torque the bead to lie parallel to $\mathbf{H}_{XY}$. Thus $\mathbf{m}_a$ will lie in-plane (although not necessarily parallel) to the rod during attachment. However, this method has the potential to create chains of beads in the channel thereby reducing the number of single bead attachments to the rods. The second method would utilize a circumferential ring of ssDNA around the bead (complementary to the overhangs on the DNA microrod) which lie in the same plane as the anisotropy axis (although not necessarily parallel to the rod when it is attached). This step could be implemented by rolling a steptavidinated magnetic bead across a surface treated with ssDNA conjugated with biotin. Due to the biotin-streptavidin affinity, the ssDNA would bind to the bead creating a circumferential ring of ssDNA which would be in the same plane as the anisotropy axis. When the beads are combined with the

DNA rods tethered to the channel surface, the bead attachment would be limited to these specific orientations.

7.4 Field-Dependence of Torque on Magnetic Beads due to Permanent Moment or Anisotropic Induced Moment

In previous works [259, 260], an easy axis from an anisotropic induced moment ($\mathbf{m}_{ia}$) of single MyOne superparamagnetic Dynabeads was observed for fields above 150 Oe by attaching the bead to a bacteria tethered to the surface [260]. Also, a permanent moment($\mathbf{m}_p$) was measured by rotating bead dimers with fields lower than 20 Oe [259]. However, the combined effects of both $\mathbf{m}_{ia}$ and $\mathbf{m}_p$ have not been simultaneously observed. In such rotating dimer experiments, $\mathbf{m}_{ia}$ is not detected due to the dominance of inter-bead dipole interactions. However, single bead rotation experiments, which would enable measurements of both $\mathbf{m}_{ia}$ and $\mathbf{m}_p$, have not yet been implemented due to the challenges of tracking the rotational orientation of individual spherically symmetric beads. By attaching a stiff DNA rod tethered to the surface and a superparamagnetic bead (MyOne Dyabeads), it was possible to study the effects of both $\mathbf{m}_p$ and $\mathbf{m}_{ia}$. In the field range explored 10 Oe to 100 Oe, $\mathbf{m}_p$ initially is the main influence on the torque on the bead and then transitioned to major contributions from $\mathbf{m}_{ia}$ in agreement with the previous work on Dynabeads at low [259] and high fields [260]. This cross-over between $\mathbf{m}_p$ and $\mathbf{m}_{ia}$ can be directly observed by studying the periodicity of the underlying magnetic potential – $\mathbf{m}_p$ displays a single preferred orientation whereas $\mathbf{m}_{ia}$ is pi periodic and thus has two preferred orientations. Furthermore, if $\mathbf{m}_p$ is not parallel with $\mathbf{m}_{ia}$, the bead's orientation will shift as $\mathbf{H}_{XY}$ is increased when $\mathbf{m}_{ia}$ begins to lead.

7.4.1 Field-Dependent Periodicity of Magnetization Orientation

To understand the relative contributions of the different moments at each field strength for a single bead, the periodicity of the underlying magnetic potential was explored. When $\mathbf{m}_p$ is the principal moment, thermal fluctuations are not fast enough to align with an

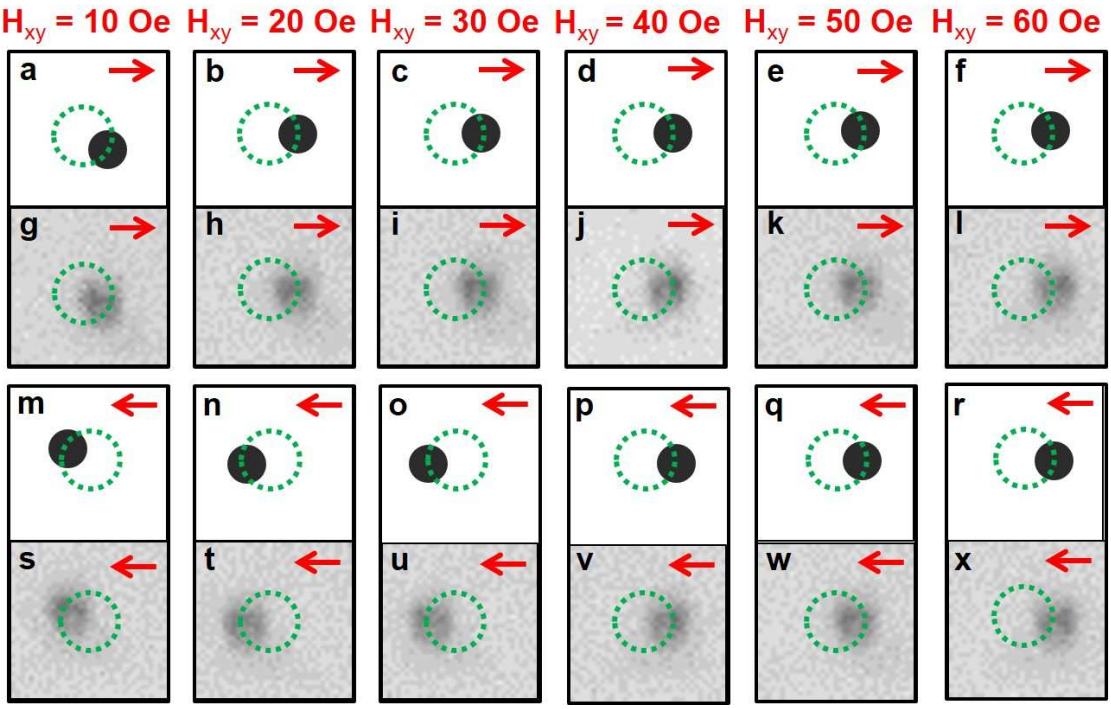

Figure 7.5: A single bead held at $\mathbf{H}_{XY}$ = 10, 20, 30, 40, 50, and 60 Oe for two different field directions 180° from one another (red). (a-f and m-r) Schematics showing the position of the bead relative to the rotation radius of the bead attached to the DNA rod with respect to $\mathbf{H}_{XY}$. The rotational circumference of the bead attached to the rod is shown in green and the bead is shown in gray. (g-l and s-x) Bright field images of the position of the bead with respect to $\mathbf{H}_{XY}$. For $\mathbf{H}_{XY}$ = 10 Oe to $\mathbf{H}_{XY}$ = 30 Oe, the bead changed position but for $\mathbf{H}_{XY}$ = 40 Oe to $\mathbf{H}_{XY}$ = 60 Oe it remained at the starting location.

instantaneous 180° magnetic field direction change in which case $\mathbf{m}_p$ facilitates rotation of the entire bead to align with the new field orientation. However, when $\mathbf{m}_{ia}$ is dominant, reversing $\mathbf{H}_{XY}$ by 180° would cause the Neel dipoles to thermally reorient and align with $\mathbf{H}_{XY}$. Therefore no torque would be applied on the dipoles causing the bead to remain fixed in the same location without any rotational changes; the magnetic potential, in this case, will display pi periodicity.

Reorienting $\mathbf{H}_{XY}$ by 180° and monitoring the bead orientation (which reflects the response of the magnetization) was implemented on several DNA rod-linked beads at 10 different field strengths ranging between 10 Oe and 100 Oe. Fig. 7.5 shows the orientation of such a single bead at two field orientations 180° from each other for six field strengths.

Increasing $\mathbf{H}_{XY}$ from 10 Oe to $\mathbf{H}_{XY}$ = 30 Oe (Fig. 7.5, right columns 1-3), the bead changed locations when $\mathbf{H}_{XY}$ was reversed. Their responses confirm that $\mathbf{m}_p > \mathbf{m}_{ia}$ in this field range. Between $\mathbf{H}_{XY}$ = 40 Oe to $\mathbf{H}_{XY}$ = 60 Oe (Fig. 7.5, right columns 3-6), the bead orientation remained unchanged when the field direction was reversed showing that $\mathbf{m}_{ia} > \mathbf{m}_p$ and is under a pi periodic potential in this field range. The field at which transitions between these distinct behaviors occur varied from bead to bead due to the variance in the permanent moment and susceptibility. In order to understand the variance from bead to bead, the same experiment of reversing $\mathbf{H}_{XY}$ and monitoring the bead orientation with respect to the tethered DNA pivot was conducted for 52 tethered beads. By determining the field strength at which the bead begins to remain in the same position when the field is reversed, the field range for which $\mathbf{m}_p$ or $\mathbf{m}_{ia}$ is the principle contributor was determined for each bead. The percentage of beads with $\mathbf{m}_p$ or $\mathbf{m}_{ia}$ dominating was found as a function of the field (Fig 7.6). As evident, 90% of the beads were characterized by strong $\mathbf{m}_p$ at 10 Oe thus displaying $\mathbf{m}_p$ as the primary component to torque the bead. However, as the field was increased to 100 Oe, only 31% of dominating $\mathbf{m}_p$ component beads were identified. This method of field reversal allows determining the specific field regimes for which $\mathbf{m}_p$ and $\mathbf{m}_{ia}$ will be the primary contributor to the magnetic torque on the bead.

7.4.2 Anisotropic Magnetization Calculation from Critical Frequency

The anisotropic magnetization ($\mathbf{m}_a$) which includes the permanent($\mathbf{m}_p$) and anisotropic induced ($\mathbf{m}_{ia}$) moments of the bead can be approximated from the rotational dynamics and frequency of the bead as a function of the $\mathbf{H}_{XY}$ rotational frequency. In previous studies [222, 258–260], at low fields (< 30 Oe) the anisotropic magnetization is generally identified to be due to $\mathbf{m}_p$. The magnetic torque on the bead orients $\mathbf{m}_a$ to align with $\mathbf{H}_{XY}$ and precess in the rotating $\mathbf{H}_{XY}$. However, beyond a critical field frequency (f_c), the bead is unable to keep up with $\mathbf{H}_{XY}$ due to drag forces. Below f_c, the rotation of the bead and the field are synchronized (Fig. 7.7) where f_c = 4.4 Hz. The bead rotation slows down as the frequency of the field is increased beyond f_c due to a phase lag between $\mathbf{H}_{XY}$ and $\mathbf{m}_a$. The equation of motion in which inertial forces are negligible relates the magnetic and drag

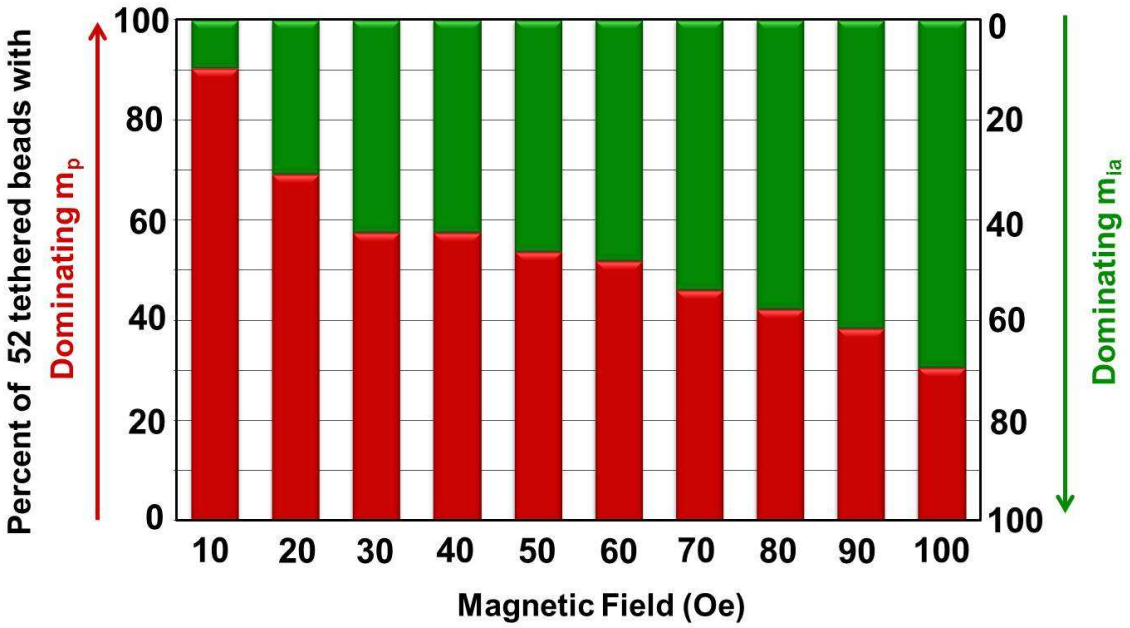

Figure 7.6: Percentage of 52 beads with principal $\mathbf{m}_p$ (red) or $\mathbf{m}_{ia}$ (green) magnetization components as a function of the field measured by reversing $\mathbf{H}_{XY}$ = 10, 20, 30, 40, 50, 60, 70, 80, 90 and 100 Oe and monitoring the change in the tethered beads orientation with respect to the DNA rod pivot. At 10 Oe, 90% of the beads were controlled by $\mathbf{m}_p$ but as the field increased to 100 Oe the beads responses were dominated by the presence of $\mathbf{m}_{ia}$.

torques:

$$\mathbf{m}_a \mu_0 H sin(\omega_H t - \phi_B) = \gamma \frac{d\phi_B}{dt} \tag{7.5}$$

where $\mathbf{m}_a$ is the anisotropic magnetization, μ_0 is the permeability of free space, ω_H is the angular rotation frequency of the field (H), ϕ_B the angle between the line formed from the pivot to the position of the tethered bead and the positive x-axis and γ is the hydrodynamic drag constant. The bead experiences a rotational and translational torque where the hydrodynamic drag constants are each given by [262, 263]:

$$\gamma_r = 8\pi\eta r^3 \tag{7.6}$$

$$\gamma_t = 6\pi\eta r \tag{7.7}$$

where η and r are the dynamic viscosity of the fluid and the bead radius respectively. The rotational and translational drag torques around the circumference of radius l are respectively:

$$\tau_{rot.drag} = \gamma_r \frac{d\phi_B}{dt} \tag{7.8}$$

$$\tau_{trans.drag} = F_{drag} l = \gamma_t v l = \gamma_t l^2 \frac{d\phi_B}{dt} \tag{7.9}$$

where F_{drag} is the drag force on the bead, l the rotation radius of the bead (length from the center of the bead to the surface attachment site of the DNA rod), v and $\frac{d\phi_B}{dt}$ the tangential and angular velocity of the bead. The net torque due to drag is therefore given by

$$\tau_{drag} = (\gamma_r + \gamma_t l^2)\frac{d\phi_B}{dt} = (8\pi\eta r^3 + 6\pi\eta r l^2)\frac{d\phi_B}{dt} \tag{7.10}$$

The equation of motion given by equation 7.5 can be rewritten with the given hydrodynamic torque (equation 7.10) as:

$$\mathbf{m}_a \mu_0 H sin(\omega_H t - \phi_B) = (8\pi\eta r^3 + 6\pi\eta r l^2)\frac{d\phi_B}{dt} \tag{7.11}$$

At the critical frequency, the torque on the anisotropic moment ($\mathbf{m}_a$) will be maximum such that $sin(\omega_H t - \phi_B) = 1$. By solving equation 7.11 at the critical frequency ($\omega_H = \frac{d\phi_B}{dt}$) for $\mathbf{m}_a$, the anisotropic moment is determined:

$$\mathbf{m}_a = \frac{2\pi\eta(4r^3 + 3rl^2)\omega_c}{\mu_0 H} \tag{7.12}$$

where $\omega_c (= 2\pi f_c)$ is the critical angular frequency. For the bead in Fig. 7.7 whose critical frequency (f_c) is 4.4 Hz, $\mathbf{m}_a$ was calculated to be 5.7 $\times$ 10^{-17} Am^2 at 20 Oe which is comparable to 1.50 $\times$ 10^{-16} Am^2 (the permanent moment calculated in dimmer rotation experiments[222]).

7.4.3 Field-Dependent Magnetization Strength

By measuring the critical frequencies (Section 7.4.2) for the same bead at multiple field strengths, the total anisotropic moment ($\mathbf{m}_a$) can be calculated as a function of the external

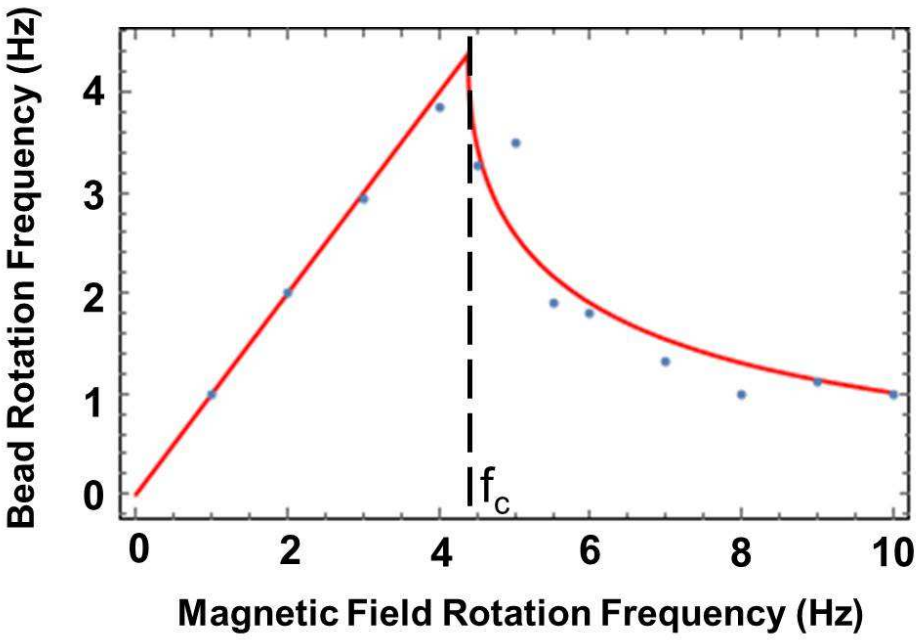

Figure 7.7: A single bead fixed to a DNA rod attached the surface was precessed in $\mathbf{H}_{XY}$ = 20 Oe precessing at frequencies between 1 Hz to 10 Hz. At frequencies below, 4.4 Hz, the critical frequency (f_c), the bead rotated synchronously with $\mathbf{H}_{XY}$. At frequencies above f_c, the bead lagged to the field.

field. Since $\mathbf{m}_a$ is the sum of the permanent($\mathbf{m}_p$) and induced anisotropic ($\mathbf{m}_{ia}$)moments, both will contribute. $\mathbf{m}_{ia}$ is linearly dependent on the field with zero remanence. Therefore $\mathbf{m}_a$ will be also linearly field dependent. However, due to the contribution from $\mathbf{m}_p$ which is independent of the field, $\mathbf{m}_a$ will have some remnant magnetization in the absence of an external field.

In Fig. 7.8A, $\mathbf{m}_a$ for a single bead is calculated for $\mathbf{H}_{XY}$ = 35, 50, 65, 80 Oe by determining the critical frequency (f_c) at each field and using equation 7.12. At low fields ($\leq$ 65 Oe), $\mathbf{m}_a$ increases linearly with the field as shown by the linear fit (black dash line). At high fields ($\geq$ 80 Oe) $\mathbf{m}_a$ begins to saturate which is a lower saturation point than the total moment that includes the isotropic induced moment. $\mathbf{m}_p$ is determined from the y-intercept of the fit which for this bead is 0.6 $\times$ 10^{-17} Am^2 and is plotted as the red dotted line. Since $\mathbf{m}_{ia}$ does not have any remnant magnetization but is the sole contributor to

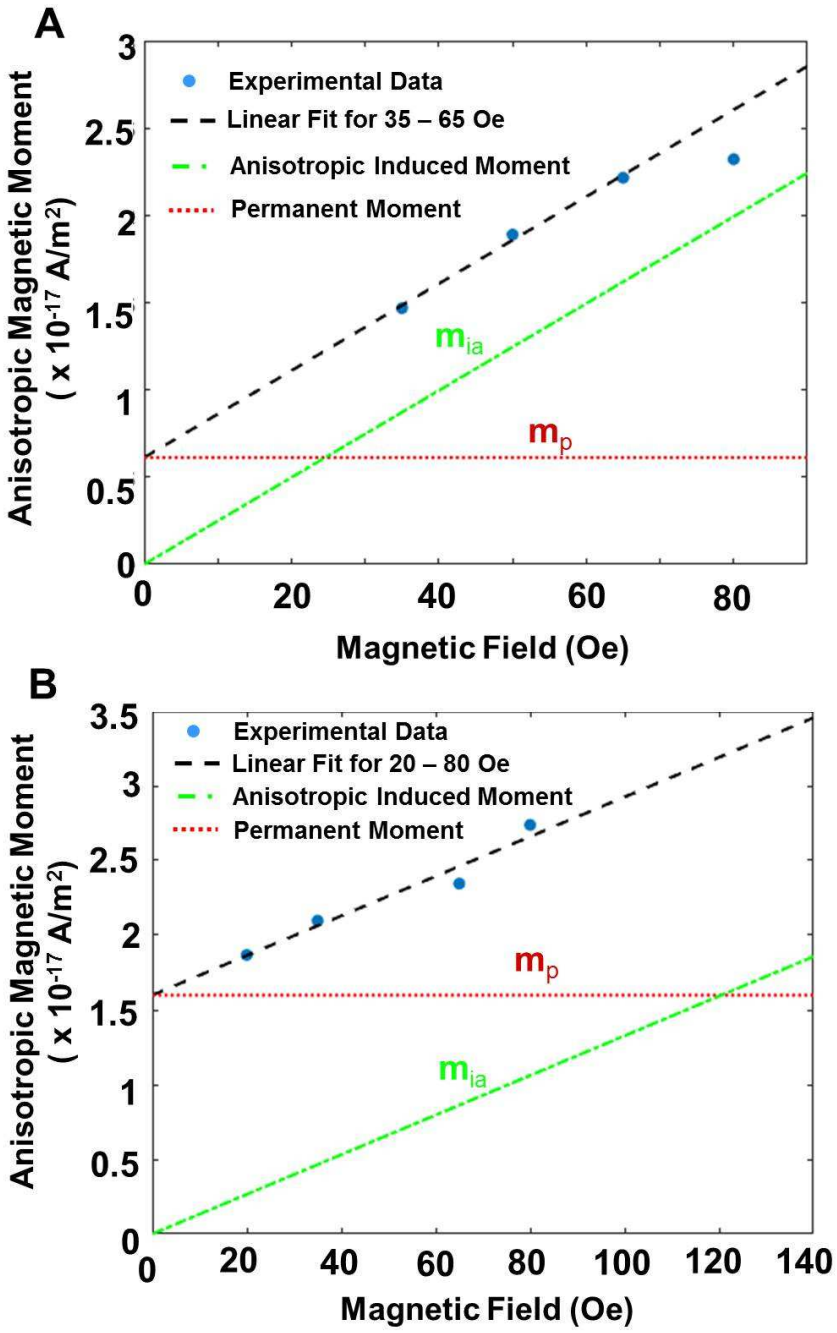

Figure 7.8: Field-dependent anisotropic magnetization ($\mathbf{m}_a$) was calculated for two beads (A) for $\mathbf{H}_{XY} = 35$, 50, 65, and 80 Oe and (B) for $\mathbf{H}_{XY} = 20$, 35, 65 and 80 Oe. Experimental measurements are plotted as blue dots and fit linearly (black dashed line). The permanent moment ($\mathbf{m}_p$) (red dotted line) was calculated from the y-intercept and the anisotropic induced moment ($\mathbf{m}_{ia}$) (green dot-dashed line) from the slope. The crossover frequency for which $\mathbf{m}_{ia} > \mathbf{m}_p$ changes from 25 Oe in A to 120 Oe in B.

the linear increase in $\mathbf{m}_a$, $\mathbf{m}_{ia}$ varies with the same slope deduced from the fit with a y-intercept at the origin indicated by the green dot-dashed line in Fig. 7.8. The field strength at which the dot-dashed green and dotted red lines intersect is the crossover field in which $\mathbf{m}_{ia}$ begins to lead over $\mathbf{m}_p$. The change from $\mathbf{m}_p$ to $\mathbf{m}_{ia}$ dominating was observed (Fig. 7.5) and discussed in Section 7.4.1. The change in the field-dependence of the moments was observed by the difference in the response of the tethered bead when $\mathbf{H}_{XY}$ was reversed by 180°. When $\mathbf{m}_p > \mathbf{m}_{ia}$, the bead rotated 180° around the pivot to align with the field. However, when $\mathbf{m}_{ia} > \mathbf{m}_p$, the bead remained in the same position with no rotational change. The field at which this change in the bead response occurred is indicated by the crossover field shown in 7.8A at ∼25 Oe.

As expended, this crossover field varied from bead to bead with some beads having a permanent moment ($\mathbf{m}_p$) that continues to be the primary contributor ($\mathbf{m}_p > \mathbf{m}_{ia}$) at 100 Oe. In Fig. 7.8B, a bead with a larger $\mathbf{m}_p$ was studied to determine $\mathbf{m}_a$ at $\mathbf{H}_{XY}$ = 20, 35, 65, 80 Oe. The response as $\mathbf{H}_{XY}$ approaches zero (y-intercept) provides for $\mathbf{m}_p$ and was 1.6×10^{-17} Am^2 (2.7 times larger than the bead in Fig. 7.8A). From $\mathbf{m}_{ia}$ determined from the slope of the fit for this particular bead, the crossover field is determined to be $\mathbf{H}_{XY}$ = 120 Oe. This higher crossover field agrees with Fig. 7.6 showing that some beads were reversing positions even up to 100 Oe (the highest field measured).

7.4.4 Field-Dependent Magnetization Orientation

The direction of the net anisotropic magnetization ($\mathbf{m}_a$) of the bead is given by the vector sum of $\mathbf{m}_p$ and $\mathbf{m}_{ia}$ ($\mathbf{m} = \mathbf{m}_p + \mathbf{m}_{ia}$) in which the isotropic induced moment ($\mathbf{m}_{ii}$) increases the net magnetization but does torque the bead. At low fields ($\mathbf{m}_p \gg \mathbf{m}_{ia}$), $\mathbf{m}_a$ will be mostly aligned with $\mathbf{m}_p$. However, at high fields when $\mathbf{m}_{ia} \gg \mathbf{m}_p$, $\mathbf{m}_a$ will be more aligned along $\mathbf{m}_{ia}$. As long as $\mathbf{m}_p$ and $\mathbf{m}_{ia}$ lie in the same direction, $\mathbf{m}_a$ will not change directions as $\mathbf{H}_{XY}$ is increased as illustrated in Figs. 7.9A-C. Fig. 7.9A and B show a schematic of the alignment of the moments at low and high fields respectively when $\mathbf{m}_p$ and $\mathbf{m}_{ia}$ are aligned. In this case, due to alignment of $\mathbf{m}_p$ and $\mathbf{m}_{ia}$, thermal fluctuations of the bead under $\mathbf{H}_{XY}$ = 10, 20, 30, 40, 50 and 100 Oe for four orthogonal directions are all centered

around the same position (Fig. 7.9C).

If, however, the orientations of $\mathbf{m}_p$ and $\mathbf{m}_{ia}$ are different, the angular position of the bead will shift as $\mathbf{H}_{XY}$ is changed. The shift would not be greater than 45° due to the pi periodicity of the easy axis arising from $\mathbf{m}_{ia}$. When held at four orientations at $\mathbf{H}_{XY}$ = 10, 20, 30, 40, 50 and 100 Oe, a field-dependent shift of the bead was often observed at each location. The shift varied from bead to bead but consistently showed similar modifications for the same bead at all four orientations. Figs. 7.9D-F illustrates a case where $\mathbf{m}_p$ or $\mathbf{m}_{ia}$ are in-plane but offset by some angle. Fig. 7.9D and E show a schematic of how the bead has to rotate to more closely align with $\mathbf{m}_p$ or $\mathbf{m}_{ia}$ as the field is increased. The thermal fluctuations of the bead with respect to $\mathbf{H}_{XY}$ = 10, 20, 30, 40, 50 and 100 Oe for four orthogonal directions shown in Fig. 7.9F all shift in-plane in the clockwise direction as $\mathbf{H}_{XY}$ is increased since $\mathbf{m}_p$ and $\mathbf{m}_{ia}$ are not aligned (Fig. 7.9F).

Apparent radial shifts in the location of beads were also observed for some beads as $\mathbf{H}_{XY}$ increased. Since the rod is stiff with a persistence length of ~20 μm (for the low associated pN forces), these shifts are likely due to out-of-plane bead movements which, when viewed from above, appears to reflect a radial change of the radius of rotation. Figs. 7.9G-I illustrate a case where $\mathbf{m}_p$ and $\mathbf{m}_{ia}$ lie out-of-plane from one another. A schematic of how the bead has to rotate from an out-of-plane to an in-plane position to align with $\mathbf{m}_p$ or $\mathbf{m}_{ia}$ as the field is increased is shown in Fig. 7.9H and G. The thermal fluctuations of a bead with respect to $\mathbf{H}_{XY}$ = 10, 20, 30, 40, 50 and 100 Oe for four orthogonal directions all shift radially from projected positions closer to the pivot to further away displaying a shift from the out-of-plane direction to an in-plane orientation as $\mathbf{H}_{XY}$ is increased (Fig. 7.9I). Furthermore, in this case, the anisotropy axis does not lie parallel with the rod and therefore, this axis is not aligned with $\mathbf{H}$ as discussed in Section 7.3.

7.4.5 Conclusions

The anisotropic magnetizations ($\mathbf{m}_a$) of superparamagnetic beads were studied in single bead experiments by exploiting stiff DNA levers to detect the bead orientation. Previous studies have focused on either the permanent moment ($\mathbf{m}_p$) at low field (< 30 Oe) or the

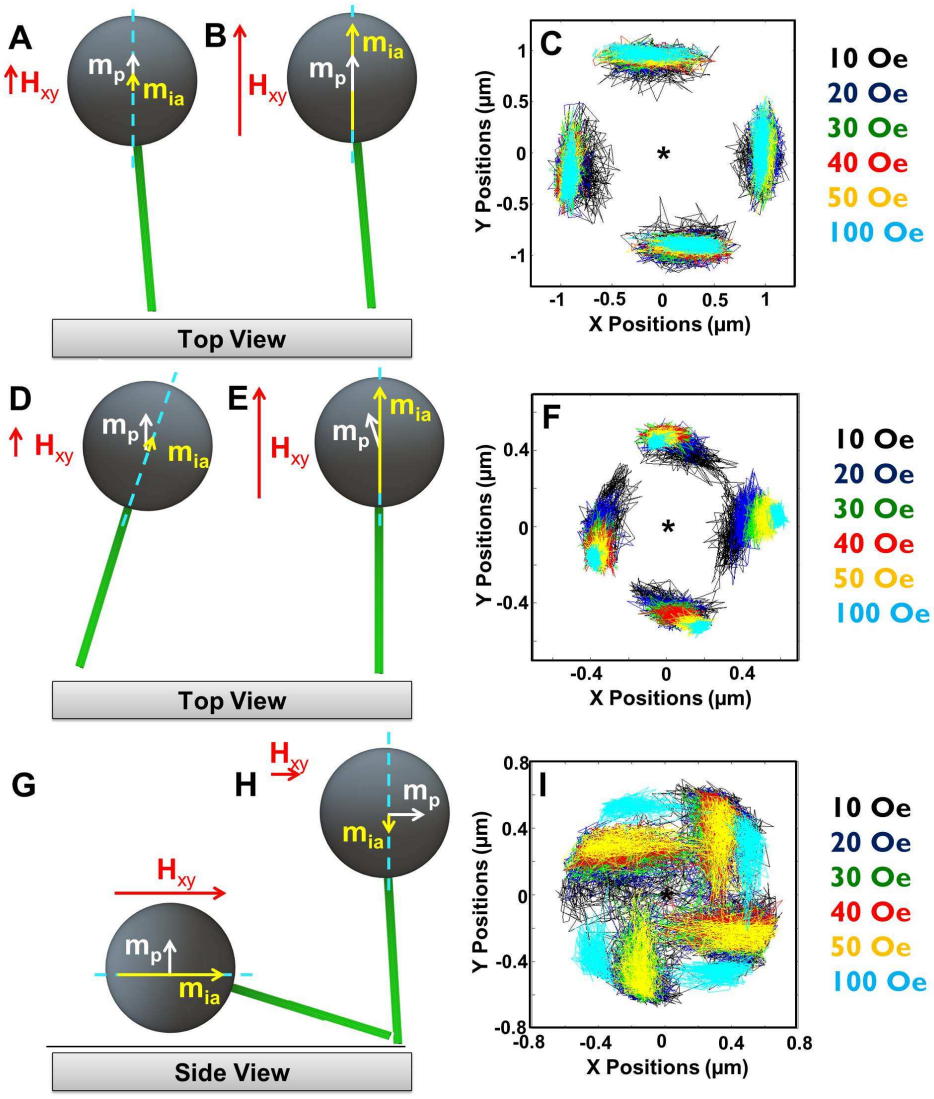

Figure 7.9: (A-C)$\mathbf{m}_p$ and $\mathbf{m}_{ia}$ are aligned – therefore the position of the bead does not change with $\mathbf{H}_{XY}$. (D-F) $\mathbf{m}_p$ and $\mathbf{m}_{ia}$ are in-plane but with some angular difference – therefore the position of the bead changes in-plane with $\mathbf{H}_{XY}$. (G-I) $\mathbf{m}_p$ and $\mathbf{m}_{ia}$ have some out-of-plane angular difference – thus the position of the bead changes with $\mathbf{H}_{XY}$ in out-of-plane direction as displayed from the projection as a radial change. (A,D,H) At low $\mathbf{H}_{XY}$, $\mathbf{m}_p$ (white) will dominate and will torque the bead to line up with $\mathbf{H}_{XY}$ (red). (B,E,G) At high $\mathbf{H}_{XY}$, $\mathbf{m}_{ia}$ (yellow) will dominate and will torque the bead to align along the easy axis (cyan dashed line). (C,F,I) The tracking of a single bead held at 4 different orientations with $\mathbf{H}_{XY}$ = 10, 20, 30, 40, 50, 100 Oe – black, blue, green, red, yellow, cyan respectively. The rod-surface attachment site where the bead pivots is marked by the black asterisk.

anisotropic induced moment ($\mathbf{m}_{ia}$) manifested as an easy axis at high fields ($>$ 150 Oe) and therefore, the combined effects of both moments were not simultaneously investigated. Due to the challenge of tracking the orientation of spherically symmetric beads, measuring $\mathbf{m}_p$ and $\mathbf{m}_{ia}$ separately is difficult. Therefore, single bead rotation experiments had not previously been conducted for MyOne Dynabeads and other smaller beads. While dimers are often used instead to approximate $\mathbf{m}_p$, $\mathbf{m}_{ia}$ cannot be observed in these cases due to inter-bead dipole interactions. This study has overcome these challenges by attaching stiff DNA levers tethered to the surface and by providing a direct measure of $\mathbf{m}_a$ as a function of the field in which the contributions of both $\mathbf{m}_p$ and $\mathbf{m}_{ia}$ were observed.

The field regime determining which component of the moment dominates was determined by reversing an in-plane external field ($\mathbf{H}_{XY}$) and observing the change in the position of the bead. When $\mathbf{m}_p$ is the primary component, upon field reversal the bead would rotate 180°. However, when $\mathbf{m}_{ia}$ is the significant component, it would remain in the same position since $\mathbf{m}_{ia}$ would internally reverse directions synchronously with the field and in effect act as an easy axis. The crossover field at which $\mathbf{m}_{ia}$ begins to be the primary contributor was tested by reversing the field for $\mathbf{H}_{XY}$ lying between 10 to 100 Oe. The beads displayed a wide range of crossover fields from 10 Oe to over 100 Oe since some beads were still rotating 180° with respect to the pivot at 100 Oe.

The strength of $\mathbf{m}_a$ was calculated from the critical frequency (f_c)(frequency at which the bead cannot synchronously rotate with a precessing $\mathbf{H}_{XY}$). From the equation of motion, $\mathbf{m}_a$ was determined by measuring the f_c at a specific $\mathbf{H}_{XY}$. As the field was increased, $\mathbf{m}_a$ increased linearly and then began to saturate. The linear increase in $\mathbf{m}_a$ with the field is solely due to $\mathbf{m}_{ia}$. From fitting the linear regime of $\mathbf{m}_a$, $\mathbf{m}_p$ was deduced (y-intercept) which was consistent with $\mathbf{m}_a$ having some magnetic remanence. The $\mathbf{m}_p$ of two beads varied from 0.6×10^{-17} to 1.6×10^{-17} Am^2. Differences in $\mathbf{m}_p$ and $\mathbf{m}_{ia}$ lead to different crossover fields that ranged from 25 Oe to 120 Oe for the two beads studied (Fig. 7.8). This behavior illustrates variations from bead to bead with the dominating moment varying largely in the field region for 10 Oe to 100 Oe (Fig. 7.6). Finally, the orientation of $\mathbf{m}_a$ was also observed to be field dependent since the position of the bead occasionally

changed with the field strength. This is due to the difference in orientations of the $\mathbf{m}_p$ and $\mathbf{m}_{ia}$ and changes in their strengths.

Chapter 8

Preliminary Study of Magnetic Actuation of *Escherichia coli* for Protein Patterning

Technologies that control matter at the nano and microscale are crucial towards developing new engineered materials and devices. Specifically, patterning surfaces into bio-adhesion and non-adhesion regions have attracted interest in devices ranging from the spatial control of cellular organization to engineering cell-based sensors [264, 265]. While these more traditional approaches often depend on lithographic fabrication, they can be expanded upon by taking advantage of the biological systems within a living cell which also operates on the nano and microscale. In this study, a system to functionalize a targeted location on the surface of a chip with the protein AmCyan from transformed *Escherichia coli* cells is being developed in collaboration with Profs. Steven and Brian Lower at The Ohio State University. Using established methods in molecular biology where a plasmid with the amcyan gene sequence is inserted into the cell, *E. coli* are engineered to express the AmCyan protein on their outer surface. In order to transport the cells to a targeted location, the transformed *E. coli* are labeled with superparamagnetic microbeads which exert directed forces on the cells in an external field. This system overcomes multiple challenges of alternative lithographic methods which will be discussed in this chapter and presents potentially new abilities to pattern proteins dynamically during different time points of an experiment. Primary results of protein expression by *E. coli*, the transport of the cell with weak magnetic fields to targeted locations and detachment of the protein from the cell are presented in this chapter.

8.1 Methods to Pattern Proteins on a Surface

8.1.1 Photolithography

There are two traditional ways to pattern proteins on a surface. The first method utilizes photolithography [266, 267] which was used to pattern the thin film structures discussed in Chapter 2 and 3. In this method, a layer of photoresist is initially spun onto a substrate and cured (Fig. 8.1A). A mask is used to block UV light from exposing certain regions of the photoresist to form the designed pattern (Fig. 8.1B). Next, the exposed photoresist is removed by gently agitating the chip in a developer solution after which the proteins are deposited on the substrate coating the regions directly in contact with the substrate and regions with existing photoresist (Fig. 8.1C). Subsequently, the excess proteins are removed using a lift-off resist that removes the remaining photoresist leaving behind the patterned proteins that were initially on the substrate (Fig. 8.1D). Although biotin, a small protein, has been shown to be patternable using this method [266, 267], not all proteins are able to be patterned with this photolithographic approach. In the final step, the system is exposed to chemicals that can often lead to denaturing of the protein which thus limits the choice of available proteins.

8.1.2 Soft Lithography

An alternative method which does not expose the protein to harmful chemicals utilizes polymers to physically stamp the proteins on the surface (Fig. 8.2A-C) or to block specific regions where proteins do not bind (Fig. 8.2D-F) [264, 265, 268]. In the case of the stamp, the polymer, polydimethylsiloxane (PDMS), which is most commonly used, is initially formed into a stamp with elevated areas shaped with the design pattern. Proteins are deposited across the PDMS surface (Fig. 8.2A). The PDMS stamp coated with proteins is pressed against the surface (Fig. 8.2B) and removed leaving behind only the proteins in contact with the surface (Fig. 8.2C). Alternatively, PDMS can be used to physically block regions of the surface such that only the segments where proteins are desired remain uncovered (Fig. 8.2D). Proteins are then deposited onto the device (Fig. 8.2E) and the

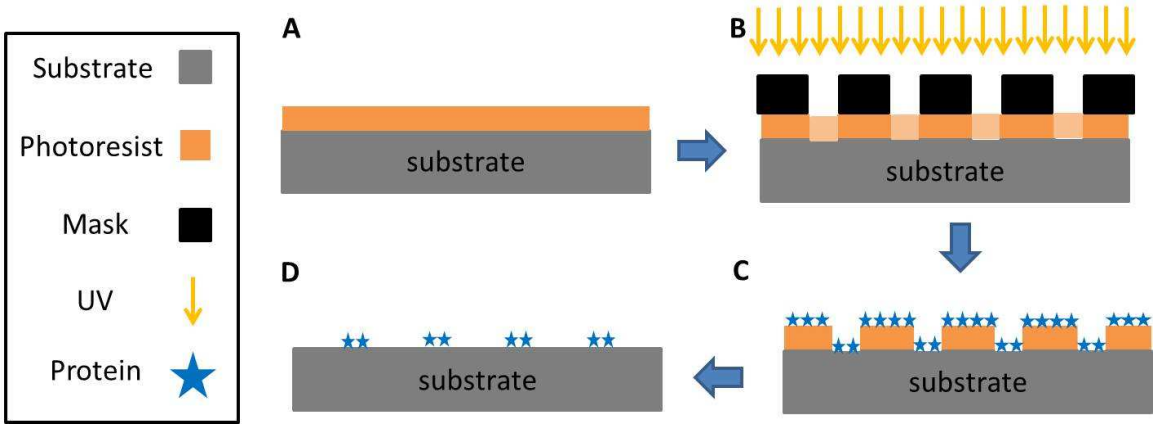

Figure 8.1: Protein Patterning Using Photolithography. (A) Photoresist is spun and curried on the substrate. (B) A patterned region of the photoresist is exposed to UV light using a mask to block specific regions. (C) The exposed photoresist is removed using a developer and the protein is deposited on the surface. (D) The remaining photoresist is removed using lift-off resist leaving behind the pattern proteins on the substrate.

PDMS removed leaving behind a patterned region of proteins (Fig. 8.2F). Although in this method, any protein may be used, the alignment of the proteins with specific locations on the device is very challenging.

8.1.3 *E. coli* Microlithography

These challenges are not only overcome by utilizing labeled *E. coli* for microlithography but it also potentially enables dynamic labeling of surfaces such that during an experiment new protein locations can be patterned. Using transformed *E. coli* to produce desired proteins, the *E. coli* essentially act as a factory to create and secrete proteins. Magnetic beads are then attached to the bacterial surface and, using thin magnetic patterns and weak external fields, the *E. coli* are transported to a targeted location where the protein is detached from the microorganism and is absorbed onto the substrate (Fig. 8.3).

8.2 Engineering the AmCyan Factory

The ″protein factory″ is engineered, in collaboration with the Lower groups at The Ohio State University, by transforming a bacteria to overexpress the desired protein. AmCyan,

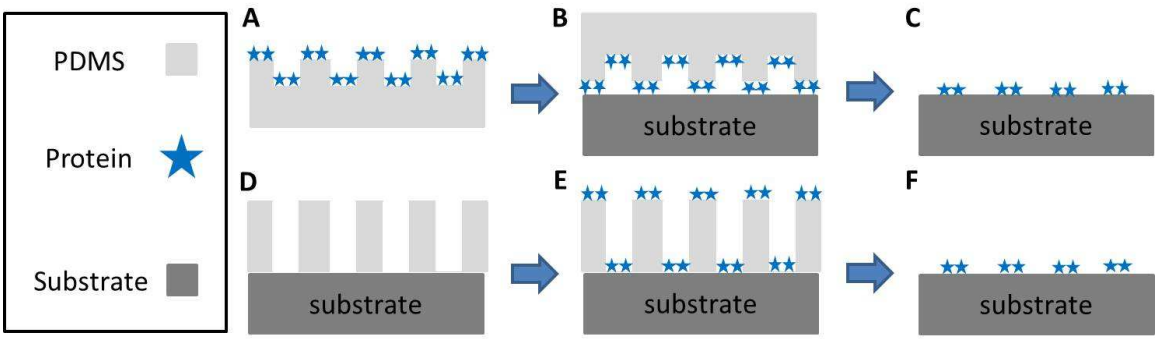

Figure 8.2: Patterning Proteins using Soft Lithography using a stamp method (A-C) and blocking method (D-F). (A) PDMS stamp is coated with protein. (B) PDMS is pressed against the surface and (C) removed leaving behind a substrate with patterned proteins. (D)PDMS is placed on the surface to block specific regions of the substrate. (E)The proteins are deposited on the device and (F) then the PDMS is removed leaving behind a substrate with patterned proteins.

a 108 kDa fluorescent protein, was selected to enable easy confirmation of transformation of the bacteria. AmCyan has a maximum excitation peak of 457 nm and a maximum absorption peak of 491 nm. Previously, Brian H. Lower et al [269] genetically engineered *E. coli* to express AmCyan on the outer surface using a plasmid which is a circular loop of double-stranded DNA encoding the information needed to synthesize AmCyan and export this protein to the outer membrane (Fig. 8.4A). The plasmid sequence consists of: (1) LPP protein (targets protein to outer membrane), (2) OmpA protein (anchors protein in the outer membrane), (3) linker amino acid sequence (connected the OmpA protein to the AmCyan protein) and (4) AmCyan (fluorescent protein used for patterning). Additionally, the ampicillin resistant gene is also included in the plasmid to ensure that the plasmid is not lost during cell division, i.e., apply selective pressure on dividing cells through growth in the presence of the antibiotic, ampicillin. The plasmid is incubated in solution with *E. coli* in which the outer membrane becomes permeable and the plasmid is taken into the cell. The cells were grown in Luria-Bertani (LB) medium containing ampicillin at 37°C on an environmental shaker at 225 rpm. Isopropyl$-\beta-$D$-$thiogalactopyranoside (IPTG) which is used as an inducer of the gene expression was incubated with a subculture of cells the last 4 hours of growth. Following this protocol, the *E. coli* were successfully transformed

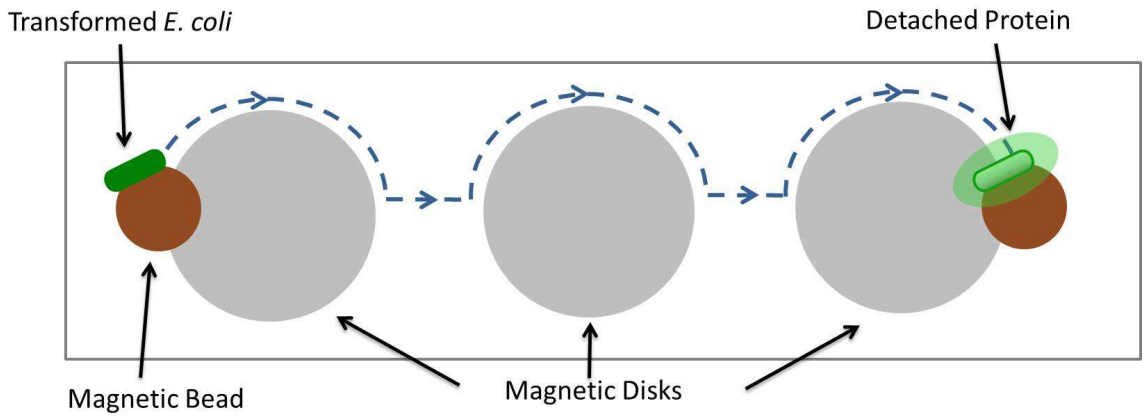

Figure 8.3: Magnetically labeled transformed *E. coli* are transported to desired location utilizing thin permalloy disks and external fields where the protein is detached from the cell and absorbed on the surface.

as seen in the bright-field image and correspond fluorescence image (Fig. 8.4B and C).

8.3 Transport of AmCyan Factory

The transformed *E. coli* were then attached to superparamagnetic beads for magnetic actuation. Since AmCyan has a theoretical isoelectric point of 6.29, it will have a negative charge when suspended in solutions with pH greater than 6.29. Other studies have shown that amino-coated beads which are slightly positive can be used to attach *E. coli* [270]. However, the commercially purchased amino-coated beads (Spherotech AM-40-10 and AM-80-10), which have shorter linker arms than polylysine used to coat the beads in Ref [270], were found to have insufficient electrostatic forces to solely hold the bacteria fixed to the bead. Instead, older cells were discovered to attach more effectively to both amino-coated and carboxyl-coated beads than more recently cultured cells. Since mature cells have had more time to synthesize extracellular polymeric substances (EPS) from lipids, sugars and proteins on the cell membrane compared to younger cells, the older cells tend to be ″stickier″.

The attachment efficiency of bacteria to the beads, therefore, varied from batch to batch even when the same protocol. *E. coli* were added in excess to the beads and were attached in small volumes. The final protocol consisted of mixing 5 μL of *E. coli* in solution with 1

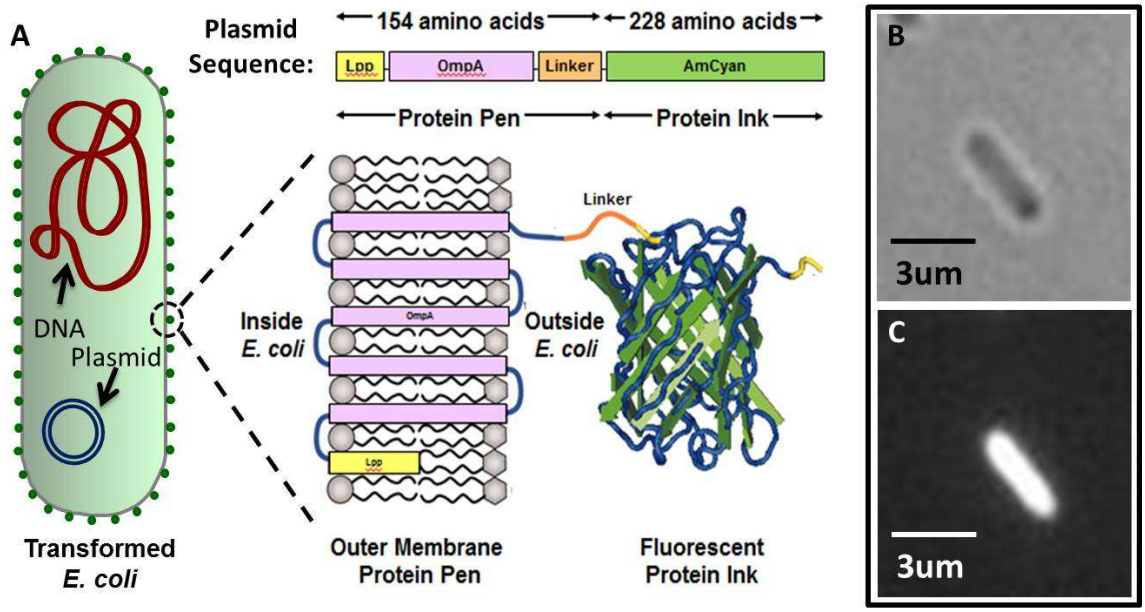

Figure 8.4: Fig. 4 Transformed *E. coli* engineered to express the fluorescent protein AmCyan. (A) Schematic of *E. coli* with plasmid expressing the AmCyan protein on the outer membrane. The plasmid sequence includes the Lpp and OmpA (embedded in the outer membrane) and the linker connecting to the AmCyan protein. The Lpp, OmpA and linker acts as a protein pen holding the fluorescent protein Ink, AmCyan. Image curtsy of Dr. Brian and Steven Lower at The Ohio State University (OSU)(B) Bright-field and (C) florescent image of transformed bacteria which fluorescence due to the expression of the AmCyan protein.

μL of beads diluted 50x from the original stock concentration. The mixture was centrifuged for 2 minutes at a maximum speed of 13,000 rpm and then rotated and centrifuged for an additional 2 minutes to form a pellet of beads and cells. The sample was vortexed until the pellet was broken up and the solution appeared homogeneous. Often in cases when the attachment was higher, the pellet took a longer time to break apart. These steps were repeated two additional times to provide more consistent attachment result. In the final step, the pellet was incubated at room temperature up to 20 minutes before breaking up and diluting with 10 - 20 μL of Phosphate-Buffered Saline (PBS). Using this protocol, cells were attached to both amino-coated beads and carboxyl-coated beads with sizes from 4 μm to 20 μm. The fluorescent images in Fig. 8.5 demonstrate *E. coli* (bright dots) attachment to

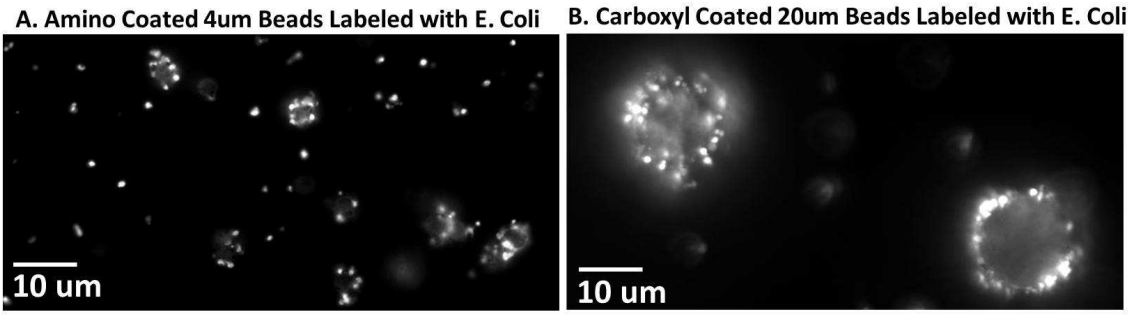

Figure 8.5: Fluorescent images of magnetically labeled transformed *E. coli*. (A) 4 μm amino-coated bead circumferentially surrounded by fluorescing *E. coli*. (B) 20 μm carboxyl-coated beads circumferentially surrounded by fluorescing *E. coli*.

4 μm amino coated beads (Spherotech, AM-40-10) (Fig. 8.5A) and 20 μm carboxyl coated beads (Spherotech, CM-200-10) (Fig. 8.5B) indicated by the bright dots circumferentially surrounding the beads.

Next, the magnetically labeled transformed *E. coli* were transported to the desired location using thin film permalloy disks (discussed in Chapter 2, 3 and 4) and external magnetic fields provided by the magnetic setup (discussed in Chapter 3). As shown in Chapter 4, permalloy disks can be magnetized using weak magnetic fields ($<$ 100 Oe) such that superparamagnetic beads magnetized in the same weak field will be trapped at the edge of the disk. In Fig. 8.6, the energy landscapes of the permalloy disk (5μm in diameter) are shown for four different field configurations with the corresponding schematic showing the bead placement on the disk [12]. Initially, the bead is trapped at position A using an in-plane field ($\mathbf{H}_{XY}$ = 50 Oe) in the positive x direction and the out-of-plane field ($\mathbf{H}_Z$ = 50 Oe) in the positive z direction (Fig. 8.6A). By rotating the field, the trap along with the magnetic bead is moved around the perimeter of the disk passing through points B and C. In order to apply a force on the bead to trap it at an adjacent disk, $\mathbf{H}_Z$ is reversed such that the initial energy minimum becomes a maximum and the bead is repelled to the closest energy minimum on the adjacent disk at location D. Using this sequence of field changes, the magnetic bead and its attached *E. coli* can be transported to any location along the edge of a disk.

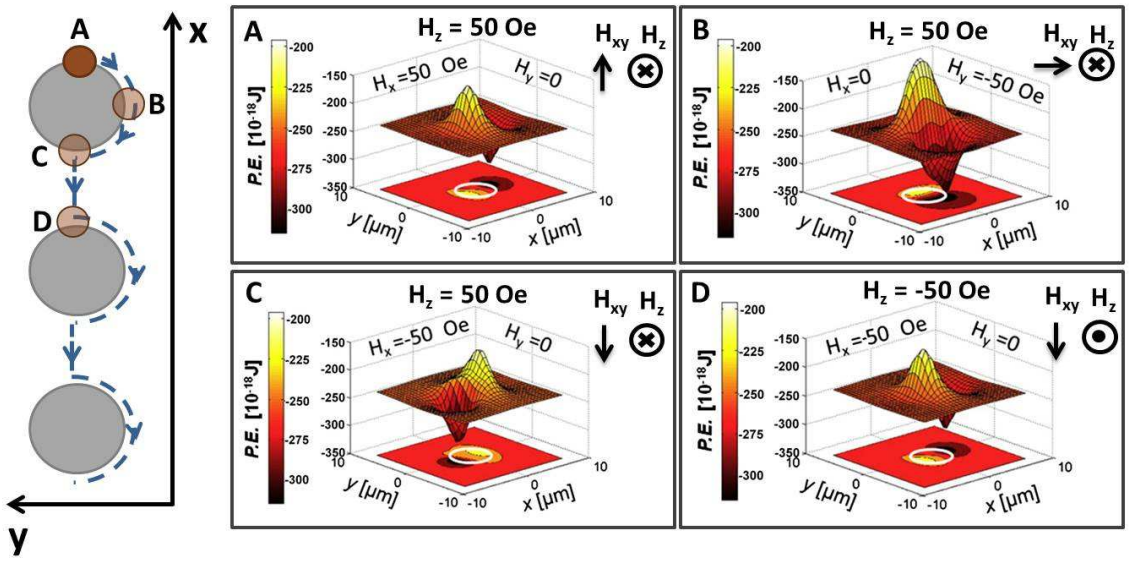

Figure 8.6: Transport of magnetic beads on permalloy disks. (A-D) Energy landscape showing the energy minimum [12] where the bead is trapped on the disk at the corresponding location. Rotating in-plane field ($\mathbf{H}_{XY}$) rotates the bead around the disks from location A through C. By reversing the out-of-plane field ($\mathbf{H}_Z$) the bead is repelled from location C to the new energy minimum at the neighboring disks at location D.

To actuate the magnetically labeled bacteria, the surface with permalloy disks was initially treated with PEG to reduce nonspecific binding of the beads and bacteria before each experiment using the method discussed in Chapter 3. Fig. 8.7 demonstrates the transport of a cell attached to a 4μm superparamagnetic bead (Spherotech, AM-40-10) which is displaced 5 disks in 8.4 seconds shown in the fluorescent images from the video time stamps.

8.4 Detachment of AmCyan

To pattern the AmCyan protein on the surface at the desired location, the AmCyan was detached from the cell. This was accomplished using the enzyme, lysozyme which breaks down the glycosidic bonds in the outer-cell membrane. In essence, it ″cuts up″ the cell membrane. The disadvantage to using lysozyme is thus, in the process of detaching Am-Cyan, the cells producing Amcyan are killed. Therefore, the linker could be redesigned so

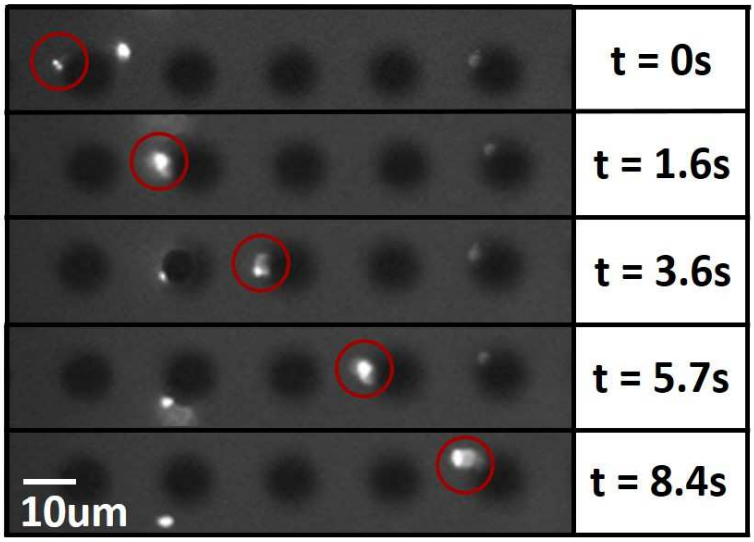

Figure 8.7: Transport of transformed *E. coli* on permalloy disks. Fluorescent images of magnetically labeled *E. coli* (circled in red) transported to a permalloy disk 5 neighboring disks over. It hops to the neighboring disk at time shots shown at 0, 1.6, 3.6, 5.7 and 8.4 seconds

that a select enzyme would target to cut the linker sequence and detach AmCyan while leaving the cell viable. Utilizing lysozyme enabled some of the AmCyan proteins to be released from the membrane and become free to be absorbed on the surface. The optimal ratio of lysozyme (10 mg/mL) to the solution of cells in PBS was found to be 1:4. To test detachment of AmCyan, *E. coli* were pelleted and resuspended in PBS since their growth media auto-fluoresce in the same region as AmCyan. Next, lysozyme was added and incubated for 30 minutes at 25°C or at 37°C. No significant difference was found in detachment at these two different temperature incubations. Finally, the cells were pelleted and the supernatant was imaged under fluorescence microscopy to confirm detachment of AmCyan (Fig. 8.8B, inset). Additionally, the excitation emission of the supernatant from the lysed *E. coli* measured using a fluorometer (Fig. 8.8B) further confirmed detachment of AmCyan specifically since the excitation emission compared well to the standard excitation emission curves of AmCyan from BD Bioscience (Fig. 8.8A).

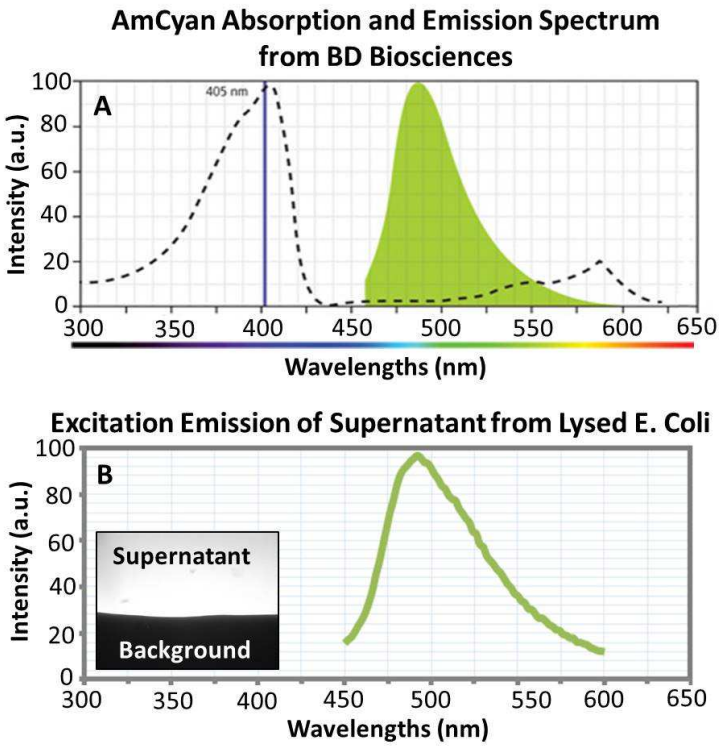

Figure 8.8: (A) Standard spectrum from BD Bioscience of the AmCyan absorption shown by the dashed line and excitation emission shown by the green area. (B) Experimental spectrum using a fluorometer showing the excitation emission of the supernatant from the lysed *E. coli* which compare well with the standard AmCyan excitation emission showing that lysozyme detached the AmCyan protein from the *E. Coli* outer membrane. Inset: Fluorescent microscopy image of the edge of supernatant on a glass slide showing the supernatant fluorescing due to the AmCyan protein in solution.

8.5 Conclusions and Future Work

The preliminary results show the potential to dynamically pattern proteins on the surface using magnetically labeled *E. coli* transformed to express the desired protein. *E. coli* were genetically engineered to express the fluorescent protein AmCyan and magnetically labeled for transport to desired location for patterning. Detachment of AmCyan from the cell was achieved using the enzyme lysozyme which breaks down the cell membrane.

Since initial tests of the absorption efficiency of AmCyan on the surface showed low attachment, other proteins such as biotin could be used in replace of AmCyan or in addition

to AmCyan due to its high surface absorption efficiency. Initially, a plasmid would be redesigned to enable the cell to express biotin or AmCyan conjugated with biotin on its outer cell membrane. Furthermore, the linker which connects the OmpA protein to the AmCyan protein (Fig. 8.4) could be engineered such that a specific enzyme targets the linker sequence to enable a higher specificity and greater detachment of AmCyan. This step would also enable cell viability after AmCyan detachment to continue the production of the protein for further patterning. Additionally, the ability to magnetically label bacteria and finely manipulate labeled cells could potentially enable future work in separating targeted bacteria from a culture containing a community of many different species of microbes.

Chapter 9
Conclusion and Future Work

In the previous chapters, the ability to remotely control superparamagnetic beads using thin-film based magnetic traps and weak external magnetic fields has been demonstrated. Such control was shown to be effective in nanoscale actuation of DNA nanomachines and microscale actuation of bacterial systems developed for protein patterning. The direct real-time control demonstrated in these systems through magnetic actuation are important steps that will enable significant advancements in biomedical devices and nanotechnology in general.

Studying the tunable magnetic traps and the magnetization of superparamagnetic beads are useful in quantifying the forces and torques that the system can apply when manipulating biological entities. The energy landscape for both soft (NiFe) and harder (CoFe) thin film magnetic patterns were calculated and experimentally confirmed (Chapter 4). The forces on 2.8 μm and 8 - 11 μm diameter beads were measured to lie in the picoNewton regime when the bead was displaced from the magnetic traps. These measurements demonstrate that the magnetic actuation platform can produce the typical forces necessary for actuation of biological organisms and present a viable method to actuate such systems in real-time without harming the targeted object.

This micromagnetic control approach was applied to DNA nanostructures which offer a broad range of applications spanning from the creation of nanoscale devices, motors and nanoparticle templates to the development of precise drug delivery systems. Advances in DNA nanotechnology such as fabrication of dynamic devices with programmable confor-

mational changes and tunable mechanical responses present great potential in development of nanomachines and molecular robots. However, fine control of these nanodevices under different configurations in real-time remain challenging using current methods which are limited to actuating a few pre-programmed states generally on time scales of minutes. These challenges were overcome in this dissertation by exploiting the microscale control of superparamagnetic beads to directly manipulate multiple DNA nanomachines with precise spatial resolution, sub-second response times, and tunable applied forces (Chapter 6). To effectively couple the motion of microbeads to control DNA nanostructures with nanometer precision, a stiff mechanical micro-lever (persistence length $\sim$20 μm) assembled from DNA nanostructures was designed to overcome the large mismatch in length scales to connect microbeads to the nanodevices. Two prototype DNA nanomachines (rotor and hinge) were magnetically actuated such that the nano-rotors exhibited a continuous range of motion and the nano-hinges were magnetically actuated over a finite range of angular motion. The nanoconstructs were finely controlled within an angular conformation with resolution of $\pm 4^{\circ}$ which allows for 45 distinct states for the rotor and 20 distinct states for the hinge. This is a significant improvement over previous actuation methods which were limited to a few (< 5) pre-programmed states. Additionally, the continuous range of motions at frequencies ranging up to 2 Hz provide another major advancement. The present study has thus demonstrated that real-time manipulation of DNA nanomachines can be achieved by integration of dynamic DNA origami devices, microscale stiff lever arms, and superparamagnetic beads to open up new possibilities in actuating and controlling nanomachines and nanorobotics.

By utilizing stiff DNA lever arms, single bead experiments (MyOne Dynabeads) were conducted to evaluate the different contributions to the magnetic response of superparamagnetic beads. Such studies had not been previously fully investigated due to the challenge of tracking the rotational orientation of individual, spherically symmetric, beads (Chapter 7). In superparamagnetic beads, anistropic contributions, that included a permanent moment and an anisotropic component of the induced moment, were observed and further analyzed in single bead experiments for MyOne Dynabeads. At lower fields (< 30 Oe), the

field independent permanent moment remained the main contributor to the torque on the bead. However, as the applied field increased the anisotropic contribution to the induced moment, that manifests as an easy axis and whose strength increased linearly with the field, additionally renders a torque on the bead. Since the permanent and anisotropic induced moments are not always aligned, the direction of total magnetization was also field dependent. Understanding the field dependency of the magnitude and direction of the anisotropic magnetization of superparamagnetic beads are essential in quantifying the torque that can be applied to manipulate microscopic and nanoscale biological systems.

In developing molecular and nanodevices, proteins are often utilized for bio-adhesion at targeted surface locations. Alternative methods to patterning proteins on the surface such as photolithography and soft lithography (discussed in Section 8.1) have limitations in the choice of protein and precision of pattern relative to other sites on the surface. Solutions to these challenges were sought out by utilizing magnetically labeled *E. coli* that were genetically transformed to express the fluorescent protein, AmCyan. If successful, this approach can further enhance flexibility in that proteins can be patterned dynamically during an experiment. Preliminary results have demonstrated that *E. coli* can be (1) engineered to express the fluorescent protein, AmCyan, (2) labeled with a variety of sizes of superparamagnetic beads, (3) transported to targeted location using thin-film based magnetic traps and weak external magnetic fields and (4) activated to release AmCyan through utilizing the enzyme, lysozyme (Chapter 8). Further development of the system would require increasing the efficiency of surface absorption of the released AmCyan on the platform. By engineering the plasmid to include a protein, such as Biotin, with a higher surface attachment efficiency, the absorption of AmCyan to the substrate could be increased. Additionally, a higher yield of AmCyan could be produced by redesigning the linker, which attaches AmCyan to the membrane anchor proteins, such that a select enzyme would target that sequence and detach the AmCyan without harming the cell membrane. This non-lethal approach would also further enable the magnetically labeled, transformed *E. coli* to continue producing AmCyan to pattern the surface after initial release of AmCyan.

Future work involving the DNA nanomachines could entail further optimization and

advancement of the magnetic actuation approach for manipulation and development of new nanomachines and their utilization as tools in studying other systems such as molecular machines and superparamagnetic beads. In order to better control the microbead (e.g. to maintain the bead in the same plane with applied magnetic fields), it could be specifically labeled in a circumferential ring that would be parallel with the anisotropic magnetization as discussed in Section 7.3. Furthermore, even greater confinement of the nanostructures, as well as the applied forces, could be established by utilizing the thin-film magnetic traps. Presently, the torque on the bead is due to its anisotropic magnetization component. However, in utilizing the magnetic traps, the total magnetization of the bead including the isotropic component will contribute to the force on the bead due to the gradient of the non-uniform field produced by the stray fields from the magnetic thin films. New patterned designs such as the ″invisible″ zigzag wires (shown in Section 3.1.1) could allow for easy visualization of the nanoscopic structures under an inverted microscope which is often utilized for TIRF microscopy. Further tests should be conducted to establish the smallest beads that could function as the force transmitting link to the DNA constructs. Although reducing the size of the beads diminishes its magnetic moment and therefore limits the applied torque, only a small fraction of the total moment (anisotropic component) renders the torque on the bead in a constant field. Since this component varies largely from bead to bead, some smaller beads could possibly have large enough moments to produce the required torque. Additionally, ferromagnetic beads which have higher anisotropic moments could be used. Although ferromagnetic beads are more likely to coalesce and form clumps due to their stronger permanent moments, use of detergents reduces nonspecific binding, and low concentrations could reduce or overcome this difficulty. Additionally, studies could be implemented using the mechanical lever arm connected to smaller sized superparamagnetic beads (e.g. nanobeads) to study their magnetization which is even more challenging to characterize. Yet, understanding the magnetization components of these smaller beads is valuable to realize in order to fully grasp and quantify the beads response in external magnetic fields.

Since machines are composed of joints that display many degrees of freedom connected

by relatively stiff links, it is important to first characterize each joint's magnetic actuation prior to designing more complex machines. While the initial work has been established for the rotor and the hinge, other constructs such as a slider joint and ball bearing joint can be tested.

These nanomachines can furthermore be employed as a tool to study other systems such as molecular machines. Understanding molecular forces is important to comprehend many of the underlying properties of molecular machines and biological processes. Therefore, the DNA hinge can be used to study these properties by attaching molecules or biological entities, such as enzymes and co-factors, proteins and nucleosomes, to hinge arms and applying forces on the molecules through actuation of the hinge. The ability to manipulate these DNA origami devices via magnetic actuation could improve capabilities to control, study, and detect biomolecular interactions in real-time. While current methods to apply molecular forces such as atomic force microscopy or optical tweezers are generally limited to single molecules, using the magnetic actuation method, multiple structures can be simultaneously studied and readily repeated. This multiplex approach allows for significant statistical analysis in the molecular force measurements.

Bibliography

[1] Terence Strick, Jean-François Allemand, Vincent Croquette, and David Bensimon. The Manipulation of Single Biomolecules. *Phys. Today*, 54(10):46–51, 2001.

[2] Jean-François Allemand, Gilles Charvin, Vincent Croquette, Giuseppe Lia, and David Bensimon. The manipulation of single biomolecules. *Interdiscip. Sci. Rev.*, 32(2):149–161, 2007.

[3] K.C. Neuman, T. Lionnet, and J.-F. Allemand. Single-Molecule Micromanipulation Techniques. *Annu. Rev. Mater. Res.*, 37(1):33–67, 2007.

[4] Keir C Neuman and Attila Nagy. Single-molecule force spectroscopy: optical tweezers, magnetic tweezers and atomic force microscopy. *Nat. Methods*, 5(6):491–505, 2008.

[5] Euan R. Kay, David A. Leigh, and Francesco Zerbetto. Synthetic Molecular Motors and Mechanical Machines. *Angew. Chemie Int. Ed.*, 46(1-2):72–191, 2007.

[6] George D. Bachand, Nathan F. Bouxsein, Virginia VanDelinder, and Marlene Bachand. Biomolecular motors in nanoscale materials, devices, and systems. *Wiley Interdiscip. Rev. Nanomedicine Nanobiotechnology*, 6(2):163–177, 2014.

[7] I Safarík and M Safaríková. Use of magnetic techniques for the isolation of cells. *J. Chromatogr. B. Biomed. Sci. Appl.*, 722(1-2):33–53, 1999.

[8] Mihrimah Ozkan, Mark Wang, Cengiz Ozkan, Richard Flynn, and Sadik Esener. Optical Manipulation of Objects and Biological Cells in Microfluidic Devices. *Biomed. Microdevices*, 5(1):61–67, 2003.

[9] Jaydev P Desai, Anand Pillarisetti, and Ari D Brooks. Engineering Approaches to Biomanipulation. *Annu. Rev. Biomed. Eng.*, 9(1):35–53, 2007.

[10] Benjamin B Yellen, Randall M Erb, Hui S Son, Rodward Hewlin, Jr., Hao Shang, and Gil U Lee. Traveling wave magnetophoresis for high resolution chip based separations. *Lab Chip*, 7(12):1681, 2007.

[11] G. Vieira, T. Henighan, A. Chen, A. J. Hauser, F. Y. Yang, J. J. Chalmers, and R. Sooryakumar. Magnetic Wire Traps and Programmable Manipulation of Biological Cells. *Phys. Rev. Lett.*, 103(12):128101, 2009.

[12] T. Henighan, A. Chen, G. Vieira, A.J. Hauser, F.Y. Yang, J.J. Chalmers, and R. Sooryakumar. Manipulation of Magnetically Labeled and Unlabeled Cells with Mobile Magnetic Traps. *Biophys. J.*, 98(3):412–417, 2010.

[13] Matthew T. Bryan, Katherine H. Smith, Maria E. Real, M. A. Bashir, Paul W. Fry, Peter Fischer, Mi-Young Im, Thomas Schrefl, Dan A. Allwood, and John W. Haycock. Switchable Cell Trapping Using Superparamagnetic Beads. *IEEE Magn. Lett.*, 1:1500104–1500104, 2010.

[14] M Donolato, A Torti, N Kostesha, M Deryabina, E Sogne, P Vavassori, M F Hansen, and R Bertacco. Magnetic domain wall conduits for single cell applications. *Lab Chip*, 11(17):2976, 2011.

[15] Aaron Chen, Tom Byvank, Woo-Jin Chang, Atul Bharde, Greg Vieira, Brandon L Miller, Jeffrey J Chalmers, Rashid Bashir, and Ratnasingham Sooryakumar. On-chip magnetic separation and encapsulation of cells in droplets. *Lab Chip*, 13(6):1172, 2013.

[16] R. Venu, B. Lim, X. H. Hu, I. Jeong, T. S. Ramulu, and C. G. Kim. On-chip manipulation and trapping of microorganisms using a patterned magnetic pathway. *Microfluid. Nanofluidics*, 14(1-2):277–285, 2013.

[17] Byeonghwa Lim, Venu Reddy, XingHao Hu, KunWoo Kim, Mital Jadhav, Roozbeh Abedini-Nassab, Young-Woock Noh, Yong Taik Lim, Benjamin B Yellen, and CheolGi Kim. Magnetophoretic circuits for digital control of single particles and cells. *Nat. Commun.*, 5(May):3846, 2014.

[18] Parikha Mehrotra. Biosensors and their applications A review. *J. Oral Biol. Craniofacial Res.*, 6(2):153–159, 2016.

[19] S Vigneshvar, C C Sudhakumari, Balasubramanian Senthilkumaran, and Hridayesh Prakash. Recent Advances in Biosensor Technology for Potential Applications An Overview. *Front. Bioeng. Biotechnol.*, 4(February):11, 2016.

[20] Pouyan E Boukany, Andrew Morss, Wei-Ching Liao, Brian Henslee, Hyunchul Jung, Xulang Zhang, Bo Yu, Xinmei Wang, Yun Wu, Lei Li, Keliang Gao, Xin Hu, Xi Zhao, O Hemminger, Wu Lu, Gregory P Lafyatis, and L James Lee. Nanochannel electroporation delivers precise amounts of biomolecules into living cells. *Nat. Nanotechnol.*, 6(11):747–754, 2011.

[21] Nima Jokilaakso, Eric Salm, Aaron Chen, Larry Millet, Carlos Duarte Guevara, Brian Dorvel, Bobby Reddy, Amelie Eriksson Karlstrom, Yu Chen, Hongmiao Ji, Yu Chen, Ratnasingham Sooryakumar, and Rashid Bashir. Ultra-localized single cell electroporation using silicon nanowires. *Lab Chip*, 13(3):336–339, 2013.

[22] Lingqian Chang, Marci Howdyshell, Wei-Ching Liao, Chi-Ling Chiang, Daniel Gallego-Perez, Zhaogang Yang, Wu Lu, John C. Byrd, Natarajan Muthusamy, L. James Lee, and Ratnasingham Sooryakumar. Magnetic Tweezers-Based 3D Microchannel Electroporation for High-Throughput Gene Transfection in Living Cells. *Small*, 11(15):1818–1828, 2015.

[23] Lingqian Chang, Paul Bertani, Daniel Gallego-Perez, Zhaogang Yang, Feng Chen, Chiling Chiang, Veysi Malkoc, Tairong Kuang, Keliang Gao, L James Lee, and Wu Lu. 3D nanochannel electroporation for high-throughput cell transfection with high uniformity and dosage control. *Nanoscale*, 8(1):243–252, 2016.

[24] Ashutosh Chilkoti, Matthew R. Dreher, Dan E. Meyer, and Drazen Raucher. Targeted drug delivery by thermally responsive polymers. *Adv. Drug Deliv. Rev.*, 54(5):613–30, 2002.

[25] Amanda R. Lowery, André M. Gobin, Emily S. Day, Naomi J. Halas, and Jennifer L. West. Immunonanoshells for targeted photothermal ablation of tumor cells. *Int. J. Nanomedicine*, 1(2):149–154, 2006.

[26] Damon Sutton, Norased Nasongkla, Elvin Blanco, and Jinming Gao. Functionalized Micellar Systems for Cancer Targeted Drug Delivery. *Pharm. Res.*, 24(6):1029–1046, 2007.

[27] Natalya Rapoport, Zhonggao Gao, and Anne Kennedy. Multifunctional Nanoparticles for Combining Ultrasonic Tumor Imaging and Targeted Chemotherapy. *JNCI J. Natl. Cancer Inst.*, 99(14):1095–1106, 2007.

[28] Kun Fu, Jiantang Sun, Lissett R Bickford, Alex W H Lin, Naomi J Halas, Tse-Kuan Yu, and Rebekah a Drezek. Measurement of immunotargeted plasmonic nanoparticles' cellular binding: a key factor in optimizing diagnostic efficacy. *Nanotechnology*, 19(4):045103, 2008.

[29] Yuanzhe Piao, Jaeyun Kim, Hyon Bin Na, Dokyoon Kim, Ji Seon Baek, Mi Kyeong Ko, Jung Hee Lee, Mohammadreza Shokouhimehr, and Taeghwan Hyeon. Wrap-bake-peel process for nanostructural transformation from beta-FeOOH nanorods to biocompatible iron oxide nanocapsules. *Nat. Mater.*, 7(3):242–7, 2008.

[30] Omid Veiseh, Jonathan W. Gunn, and Miqin Zhang. Design and fabrication of magnetic nanoparticles for targeted drug delivery and imaging. *Adv. Drug Deliv. Rev.*, 62(3):284–304, 2010.

[31] Mehmet V. Yigit, Anna Moore, and Zdravka Medarova. Magnetic Nanoparticles for Cancer Diagnosis and Therapy. *Pharm. Res.*, 29(5):1180–1188, 2012.

[32] M. Prabaharan. Chitosan-based nanoparticles for tumor-targeted drug delivery. *Int. J. Biol. Macromol.*, 72:1313–1322, 2015.

[33] A. Ashkin. Acceleration and Trapping of Particles by Radiation Pressure. *Phys. Rev. Lett.*, 24(4):156–159, 1970.

[34] A Ashkin, J M Dziedzic, J E Bjorkholm, and S Chu. Observation of a single-beam gradient force optical trap for dielectric particles. *Opt. Lett.*, 11(5):288, 1986.

[35] A. Ashkin, J. M. Dziedzic, and T. Yamane. Optical trapping and manipulation of single cells using infrared laser beams. *Nature*, 330(6150):769–71, 1987.

[36] David G Grier. A revolution in optical manipulation. *Nature*, 424(6950):810–816, 2003.

[37] Keir C Neuman and Steven M Block. Optical trapping. *Rev. Sci. Instrum.*, 75(9):2787–2809, 2004.

[38] Ke Xiao and David G. Grier. Multidimensional Optical Fractionation of Colloidal Particles with Holographic Verification. *Phys. Rev. Lett.*, 104(2):028302, 2010.

[39] Z Shao, J Yang, and A P Somlyo. Biological atomic force microscopy: from microns to nanometers and beyond. *Annu. Rev. Cell Dev. Biol.*, 11:241–65, 1995.

[40] C Bustamante, C Rivetti, and D J Keller. Scanning force microscopy under aqueous solutions. *Curr. Opin. Struct. Biol.*, 7(5):709–16, 1997.

[41] Jordanka Zlatanova, S M Lindsay, and S H Leuba. Single molecule force spectroscopy in biology using the atomic force microscope. *Prog. Biophys. Mol. Biol.*, 74(1-2):37–61, 2000.

[42] Chih-Kung Lee, Yu-Ming Wang, Long-Sun Huang, and Shiming Lin. Atomic force microscopy: Determination of unbinding force, off rate and energy barrier for protein-ligand interaction. *Micron*, 38(5):446–461, 2007.

[43] Filomena A. Carvalho and Nuno C. Santos. Atomic force microscopy-based force spectroscopy - biological and biomedical applications. *IUBMB Life*, 64(6):465–472, 2012.

[44] T Junno, K. Deppert, L. Montelius, and L. Samuelson. Controlled manipulation of nanoparticles with an atomic force microscope. *Appl. Phys. Lett.*, 66(26):3627–3629, 1995.

[45] K Luby-Phelps. Physical properties of cytoplasm. *Curr. Opin. Cell Biol.*, 6(1):3–9, 1994.

[46] Steven B Smith, Laura Finzi, and Carlos Bustamante. Direct mechanical measurements of the elasticity of single DNA molecules by using magnetic beads. *Science*, 258(5085):1122–6, 1992.

[47] Charlie Gosse and Vincent Croquette. Magnetic tweezers: micromanipulation and force measurement at the molecular level. *Biophys. J.*, 82(6):3314–29, 2002.

[48] Monica Tanase, Nicolas Biais, and Michael Sheetz. Magnetic Tweezers in Cell Biology. In *Methods Cell Biol.*, volume 83, pages 473–493. 2007.

[49] Iwijn De Vlaminck and Cees Dekker. Recent Advances in Magnetic Tweezers. *Annu. Rev. Biophys.*, 41(1):453–472, 2012.

[50] Timothée Lionnet, J.-F. Allemand, Andrey Revyakin, Terence R. Strick, Omar A. Saleh, David Bensimon, and Vincent Croquette. Single-Molecule Studies Using Magnetic Traps. *Cold Spring Harb. Protoc.*, 2012(1):pdb.top067488–pdb.top067488, 2012.

[51] Iwijn De Vlaminck, Thomas Henighan, Marijn T.J. van Loenhout, Indriati Pfeiffer, Julius Huijts, Jacob W J Kerssemakers, Allard J. Katan, Anja van Langen-Suurling, Emile van der Drift, Claire Wyman, and Cees Dekker. Highly Parallel Magnetic Tweezers by Targeted DNA Tethering. *Nano Lett.*, 11(12):5489–5493, 2011.

[52] Anton Kuzyk. Dielectrophoresis at the nanoscale. *Electrophoresis*, 32(17):n/a–n/a, 2011.

[53] J Rousselet, L Salome, A Ajdari, and J Prost. Directional motion of brownian particles induced by a periodic asymmetric potential. *Nature*, 370(6489):446–8, 1994.

[54] M S Talary, J P H Burt, J A Tame, and R Pethig. Electromanipulation and separation of cells using travelling electric fields. *J. Phys. D. Appl. Phys.*, 29(8):2198–2203, 1996.

[55] N. G. Green, H. Morgan, and Joel J. Milner. Manipulation and trapping of sub-micron bioparticles using dielectrophoresis. *J. Biochem. Biophys. Methods*, 35(2):89–102, 1997.

[56] J Yang, Y Huang, X B Wang, F F Becker, and P R Gascoyne. Cell separation on microfabricated electrodes using dielectrophoretic/gravitational field-flow fractionation. *Anal. Chem.*, 71(5):911–8, 1999.

[57] Michael P Hughes. Strategies for dielectrophoretic separation in laboratory-on-a-chip systems. *Electrophoresis*, 23(16):2569–82, 2002.

[58] Leopold Kremser, Dieter Blaas, and Ernst Kenndler. Capillary electrophoresis of biological particles: Viruses, bacteria, and eukaryotic cells. *Electrophoresis*, 25(14):2282–2291, 2004.

[59] Blanca H. Lapizco-Encinas, Rafael V. Davalos, Blake A. Simmons, Eric B. Cummings, and Yolanda Fintschenko. An insulator-based (electrodeless) dielectrophoretic concentrator for microbes in water. *J. Microbiol. Methods*, 62(3):317–326, 2005.

[60] Brian Edwards, Nader Engheta, and Stephane Evoy. Electric tweezers: Experimental study of positive dielectrophoresis-based positioning and orientation of a nanorod. *J. Appl. Phys.*, 102(2):024913, 2007.

[61] Pei Yu Chiou, Aaron T Ohta, and Ming C Wu. Massively parallel manipulation of single cells and microparticles using optical images. *Nature*, 436(7049):370–372, 2005.

[62] H. M. Hertz. Standingwave acoustic trap for nonintrusive positioning of microparticles. *J. Appl. Phys.*, 78(8):4845–4849, 1995.

[63] Afroja T. Islam, Ariful H. Siddique, T. S. Ramulu, Venu Reddy, Young-Jae Eu, Seung Hyun Cho, and Cheolgi Kim. Ultrasonic alignment of bio-functionalized magnetic beads and live cells in PDMS micro-fluidic channel. *Biomed. Microdevices*, 14(6):1077–1084, 2012.

[64] Lu Gao, C. Wyatt Shields, Leah M. Johnson, Steven W. Graves, Benjamin B. Yellen, and Gabriel P. López. Two-dimensional spatial manipulation of microparticles in continuous flows in acoustofluidic systems. *Biomicrofluidics*, 9(1):014105, 2015.

[65] George M Whitesides. The origins and the future of microfluidics. *Nature*, 442(7101):368–373, 2006.

[66] Jakub Novotný and František Foret. Fluid manipulation on the micro-scale: Basics of fluid behavior in microfluidics. *J. Sep. Sci.*, 40(1):383–394, 2017.

[67] Narayan Sundararajan, M.S. Pio, L.P. Lee, and A.A. Berlin. Three-Dimensional Hydrodynamic Focusing in Polydimethylsiloxane (PDMS) Microchannels. *J. Microelectromechanical Syst.*, 13(4):559–567, 2004.

[68] B. Ladoux and P. S. Doyle. Stretching tethered DNA chains in shear flow. *Europhys. Lett.*, 52(5):511–517, 2000.

[69] Guihua Yu, Amit Kushwaha, Jungkyu K. Lee, Eric S G Shaqfeh, and Zhenan Bao. The Shear Flow Processing of Controlled DNA Tethering and Stretching for Organic Molecular Electronics. *ACS Nano*, 5(1):275–282, 2011.

[70] Hakho Lee, Alfreda M. Purdon, Vincent Chu, and Robert M. Westervelt. Controlled Assembly of Magnetic Nanoparticles from Magnetotactic Bacteria Using Microelectromagnets Arrays. *Nano Lett.*, 4(5):995–998, 2004.

[71] H. Lee, A. M. Purdon, and R. M. Westervelt. Manipulation of biological cells using a microelectromagnet matrix. *Appl. Phys. Lett.*, 85(6):1063–1065, 2004.

[72] S. Rampini, P. Li, and G. U. Lee. Micromagnet arrays enable precise manipulation

of individual biological analytesuperparamagnetic bead complexes for separation and sensing. *Lab Chip*, 16(19):3645–3663, 2016.

[73] L. E. Helseth, T. M. Fischer, and T. H. Johansen. Domain Wall Tip for Manipulation of Magnetic Particles. *Phys. Rev. Lett.*, 91(20):208302, 2003.

[74] L. E. Helseth, T. M. Fischer, and T. H. Johansen. Paramagnetic beads surfing on domain walls. *Phys. Rev. E*, 67(4):042401, 2003.

[75] Elizabeth Mirowski, John Moreland, Stephen E. Russek, and Michael J. Donahue. Integrated microfluidic isolation platform for magnetic particle manipulation in biological systems. *Appl. Phys. Lett.*, 84(10):1786–1788, 2004.

[76] L. E. Helseth, T. M. Fischer, R. W. Hansen, and T. H. Johansen. Microscopic magnetic squeezer. *Appl. Phys. Lett.*, 85(13):2556–2558, 2004.

[77] Elizabeth Mirowski, John Moreland, Arthur Zhang, Stephen E. Russek, and Michael J. Donahue. Manipulation and sorting of magnetic particles by a magnetic force microscope on a microfluidic magnetic trap platform. *Appl. Phys. Lett.*, 86(24):243901, 2005.

[78] Klas Gunnarsson, Pierre E. Roy, Solveig Felton, Johan Pihl, Peter Svedlindh, Simon Berner, Hans Lidbaum, and Sven Oscarsson. Programmable Motion and Separation of Single Magnetic Particles on Patterned Magnetic Surfaces. *Adv. Mater.*, 17(14):1730–1734, 2005.

[79] Pietro Tierno, Tom H. Johansen, and Thomas M. Fischer. Localized and Delocalized Motion of Colloidal Particles on a Magnetic Bubble Lattice. *Phys. Rev. Lett.*, 99(3):038303, 2007.

[80] Pietro Tierno, Sathavaram V. Reddy, Jing Yuan, Tom H. Johansen, and Thomas M. Fischer. Transport of Loaded and Unloaded Microcarriers in a Colloidal Magnetic Shift Register. *J. Phys. Chem. B*, 111(48):13479–13482, 2007.

[81] Richard S. Conroy, Gary Zabow, John Moreland, and Alan P. Koretsky. Controlled transport of magnetic particles using soft magnetic patterns. *Appl. Phys. Lett.*, 93(20):203901, 2008.

[82] Pietro Tierno, Alejandro Soba, Tom H. Johansen, and Francesc Sagués. Dynamic colloidal sorting on a magnetic bubble lattice. *Appl. Phys. Lett.*, 93(21):214102, 2008.

[83] Pietro Tierno, Tom H. Johansen, and Francesc Sagués. Dynamical regimes of a paramagnetic particle circulating a magnetic bubble domain. *Phys. Rev. E*, 80(5):052401, 2009.

[84] Benjamin B. Yellen and Lawrence N. Virgin. Nonlinear dynamics of superparamagnetic beads in a traveling magnetic-field wave. *Phys. Rev. E*, 80(1):011402, 2009.

[85] Marco Donolato, Paolo Vavassori, Marco Gobbi, Maria Deryabina, Mikkel F. Hansen, Vitali Metlushko, Bojan Ilic, Matteo Cantoni, Daniela Petti, Stefano Brivio, and Riccardo Bertacco. On-Chip Manipulation of Protein-Coated Magnetic Beads via Domain-Wall Conduits. *Adv. Mater.*, 22(24):2706–2710, 2010.

[86] Matthew T. Bryan, Julian Dean, Thomas Schrefl, Faye E. Thompson, John Haycock, and Dan A. Allwood. The effect of trapping superparamagnetic beads on domain wall motion. *Appl. Phys. Lett.*, 96(19):192503, 2010.

[87] Lu Gao, Norman J. Gottron III, Lawrence N Virgin, and Benjamin B Yellen. The synchronization of superparamagnetic beads driven by a micro-magnetic ratchet. *Lab Chip*, 10(16):2108, 2010.

[88] S. Anandakumar, V. Sudha Rani, Sunjong Oh, B.L. Sinha, Migaku Takahashi, and CheolGi Kim. Translocation of bio-functionalized magnetic beads using smart magnetophoresis. *Biosens. Bioelectron.*, 26(4):1755–1758, 2010.

[89] A. Chen, G. Vieira, T. Henighan, M. Howdyshell, J. A. North, A. J. Hauser, F. Y. Yang, M. G. Poirier, C. Jayaprakash, and R. Sooryakumar. Regulating Brownian Fluc-

tuations with Tunable Microscopic Magnetic Traps. *Phys. Rev. Lett.*, 107(8):087206, 2011.

[90] Mukarram A. Tahir, Lu Gao, Lawrence N. Virgin, and Benjamin B. Yellen. Transport of superparamagnetic beads through a two-dimensional potential energy landscape. *Phys. Rev. E*, 84(1):011403, 2011.

[91] G. Vieira, A. Chen, T. Henighan, J. Lucy, F. Y. Yang, and R. Sooryakumar. Transport of magnetic microparticles via tunable stationary magnetic traps in patterned wires. *Phys. Rev. B*, 85(17):174440, 2012.

[92] Elizabeth Rapoport and Geoffrey S D Beach. Dynamics of superparamagnetic microbead transport along magnetic nanotracks by magnetic domain walls. *Appl. Phys. Lett.*, 100(8):082401, 2012.

[93] E Rapoport, D Montana, and G S D Beach. Integrated capture, transport, and magneto-mechanical resonant sensing of superparamagnetic microbeads using magnetic domain walls. *Lab Chip*, 12(21):4433, 2012.

[94] Elizabeth Rapoport and Geoffrey S D Beach. Magneto-mechanical resonance of a single superparamagnetic microbead trapped by a magnetic domain wall. *J. Appl. Phys.*, 111(7):07B310, 2012.

[95] Aaron Chen, Tom Byvank, Gregory B. Vieira, and R. Sooryakumar. Magnetic Microstructures for Control of Brownian Motion and Microparticle Transport. *IEEE Trans. Magn.*, 49(1):300–308, 2013.

[96] Marci L. Howdyshell, Michael Prikockis, Stephanie Lauback, Gregory B. Vieira, Kalpesh Mahajan, Jessica Winter, and Ratnasingham Sooryakumar. Deterministic and Stochastic Trajectories of Magnetic Particles: Mapping Energy Landscapes for Technology And Biology. *IEEE Trans. Magn.*, 50(11):1–7, 2014.

[97] N M Dempsey, D. Le Roy, H. Marelli-Mathevon, Gorky Shaw, A Dias, R B G Kramer, Le Viet Cuong, M. Kustov, L F Zanini, C Villard, K Hasselbach, C Tomba, and

F. Dumas-Bouchiat. Micro-magnetic imprinting of high field gradient magnetic flux sources. *Appl. Phys. Lett.*, 104(26):262401, 2014.

[98] Xinghao Hu, Roozbeh Abedini-Nassab, Byeonghwa Lim, Ye Yang, Marci Howdyshell, Ratnasingham Sooryakumar, Benjamin B. Yellen, and CheolGi Kim. Dynamic trajectory analysis of superparamagnetic beads driven by on-chip micromagnets. *J. Appl. Phys.*, 118(20):203904, 2015.

[99] Marci L. Howdyshell. *Micro-magnetic Structures for Biological Applications*. Ph.d. thesis, The Ohio State University, 2014.

[100] Gang Ruan, Greg Vieira, Thomas Henighan, Aaron Chen, Dhananjay Thakur, R. Sooryakumar, and Jessica O. Winter. Simultaneous Magnetic Manipulation and Fluorescent Tracking of Multiple Individual Hybrid Nanostructures. *Nano Lett.*, 10(6):2220–2224, 2010.

[101] Kalpesh D Mahajan, Gregory B Vieira, Gang Ruan, Brandon L Miller, Maryam B Lustberg, Jeffrey J Chalmers, Ratnasingham Sooryakumar, and Jessica O Winter. A MagDot-Nanoconveyor Assay Detects and Isolates Molecular Biomarkers. *Chem. Eng. Prog.*, 108(12):41–46, 2012.

[102] K D Mahajan, G Ruan, C. J. Dorcéna, G Vieira, G Nabar, N F Bouxsein, J J Chalmers, G D Bachand, R Sooryakumar, and J O Winter. Steering microtubule shuttle transport with dynamically controlled magnetic fields. *Nanoscale*, 8(16):8641–8649, 2016.

[103] Andrii B. Golovin and Oleg D. Lavrentovich. Electrically reconfigurable optical metamaterial based on colloidal dispersion of metal nanorods in dielectric fluid. *Appl. Phys. Lett.*, 95(25):254104, 2009.

[104] T. Taniyama, I. Nakatani, T. Namikawa, and Y. Yamazaki. Resistivity due to Domain Walls in Co Zigzag Wires. *Phys. Rev. Lett.*, 82(13):2780–2783, 1999.

[105] L. A. Rodríguez, C. Magén, E. Snoeck, L. Serrano-Ramón, C. Gatel, R. Córdoba, E. Martínez-Vecino, L. Torres, J. M. De Teresa, and M. R. Ibarra. Optimized cobalt nanowires for domain wall manipulation imaged by in situ Lorentz microscopy. *Appl. Phys. Lett.*, 102(2):022418, 2013.

[106] Madalina Negoita, Thomas J. Hayward, James A. Miller, and Dan A. Allwood. Domain walls in ring-shaped nanowires under rotating applied fields. *J. Appl. Phys.*, 114(1):013904, 2013.

[107] B. B. Yellen, D. S. Halverson, and G. Friedman. Arranging Matter by Magnetic Nanoparticle Assembly. In *INTERMAG 2006 - IEEE Int. Magn. Conf.*, number Track II, pages 246–246. IEEE, 2006.

[108] Aaron Chen and Ratnasingham Sooryakumar. Patterned time-orbiting potentials for the confinement and assembly of magnetic dipoles. *Sci. Rep.*, 3(1):3124, 2013.

[109] Michael Prikockis, Aaron Chen, Tom Byvank, Gregory B. Vieira, Brian Peters, Fengyuan Yang, and Ratnasingham Sooryakumar. Programmable Self-Assembly, Disassembly, Transport, and Reconstruction of Ordered Planar Magnetic Micro-Constructs. *IEEE Trans. Magn.*, 50(5):1–6, 2014.

[110] M. Prikockis, H. Wijesinghe, A. Chen, J. VanCourt, D. Roderick, and R. Sooryakumar. An on-chip colloidal magneto-optical grating. *Appl. Phys. Lett.*, 108(16):161106, 2016.

[111] Geir Fonnum, Christer Johansson, Astrid Molteberg, Steen Mørup, and Elin Aksnes. Characterisation of Dynabeads® by magnetization measurements and Mössbauer spectroscopy. *J. Magn. Magn. Mater.*, 293(1):41–47, 2005.

[112] S Mørup, M.F. Hansen, and C. Frandsen. Magnetic Nanoparticles. In *Compr. Nanosci. Technol.*, volume 1, pages 437–491. Elsevier, 2011.

[113] An-Hui Lu, E. L. Salabas, and Ferdi Schüth. Magnetic Nanoparticles: Synthesis,

Protection, Functionalization, and Application. *Angew. Chemie Int. Ed.*, 46(8):1222–1244, 2007.

[114] M Knobel, W C Nunes, L M Socolovsky, E De Biasi, J M Vargas, and J C Denardin. Superparamagnetism and other magnetic features in granular materials: a review on ideal and real systems. *J. Nanosci. Nanotechnol.*, 8(6):2836–57, 2008.

[115] Daniel Esmarch Madsen, Mikkel Fougt Hansen, and Steen Mørup. The correlation between superparamagnetic blocking temperatures and peak temperatures obtained from ac magnetization measurements. *J. Phys. Condens. Matter*, 20(34):345209, 2008.

[116] J. D. Jackson. *Classical Electrodynamics*. John Wiley & Sons, New Jersey, 3rd ed. edition, 1999.

[117] M. J. Donahue and D. G. Porter. OOMMF User's Guide, Version 1.0, 1999.

[118] Gregory B. Vieira. *Patterned Magnetic Structures for Micro-/Nanoparticle and Cell Ma- nipulation*. Ph.d. thesis, The Ohio State University, 2012.

[119] Judy Gibbs. Effective Blocking Procedures. *ELISA Tech. Bull. Corning Inc. Life Sci. Kennebunk, ME*, 1(3):1–6, 2001.

[120] Evi Stahl, Thomas G. Martin, Florian Praetorius, and Hendrik Dietz. Facile and Scalable Preparation of Pure and Dense DNA Origami Solutions. *Angew. Chemie Int. Ed.*, 53(47):12735–12740, 2014.

[121] www.lifetechnologies.com.

[122] J D Watson and F H Crick. Molecular structure of nucleic acids: a structure for deoxyribose nucleic acid. J.D. *Nature*, 171(4356):737–738, 1953.

[123] Nadrian C. Seeman. Nucleic acid junctions and lattices. *J. Theor. Biol.*, 99(2):237–47, 1982.

[124] N C Seeman and N R Kallenbach. Design of immobile nucleic acid junctions. *Biophys. J.*, 44(2):201–9, 1983.

[125] Xing Wang and Nadrian C. Seeman. Assembly and Characterization of 8-Arm and 12-Arm DNA Branched Junctions. *J. Am. Chem. Soc.*, 129(26):8169–8176, 2007.

[126] E Winfree, F Liu, L A Wenzler, and N C Seeman. Design and self-assembly of two-dimensional DNA crystals. *Nature*, 394(6693):539–44, 1998.

[127] Chengde Mao, Weiqiong Sun, and Nadrian C. Seeman. Designed Two-Dimensional DNA Holliday Junction Arrays Visualized by Atomic Force Microscopy. *J. Am. Chem. Soc.*, 121(23):5437–5443, 1999.

[128] Thomas H. LaBean, Hao Yan, Jens Kopatsch, Furong Liu, Erik Winfree, John H. Reif, and Nadrian C. Seeman. Construction, Analysis, Ligation, and Self-Assembly of DNA Triple Crossover Complexes. *J. Am. Chem. Soc.*, 122(9):1848–1860, 2000.

[129] Hao Yan. DNA-Templated Self-Assembly of Protein Arrays and Highly Conductive Nanowires. *Science (80-.).*, 301(5641):1882–1884, 2003.

[130] Dage Liu, Mingsheng Wang, Zhaoxiang Deng, Richard Walulu, and Chengde Mao. Tensegrity: Construction of Rigid DNA Triangles with Flexible Four-Arm DNA Junctions. *J. Am. Chem. Soc.*, 126(8):2324–2325, 2004.

[131] Jonathan Malo, James C. Mitchell, Catherine Vénien-Bryan, J. Robin Harris, Holger Wille, David J. Sherratt, and Andrew J. Turberfield. Engineering a 2D Protein-DNA Crystal. *Angew. Chemie Int. Ed.*, 44(20):3057–3061, 2005.

[132] Yu He, Yi Chen, Haipeng Liu, Alexander E. Ribbe, and Chengde Mao. Self-Assembly of Hexagonal DNA Two-Dimensional (2D) Arrays. *J. Am. Chem. Soc.*, 127(35):12202–12203, 2005.

[133] Faisal A. Aldaye and Hanadi F. Sleiman. Guest-Mediated Access to a Single DNA Nanostructure from a Library of Multiple Assemblies. *J. Am. Chem. Soc.*, 129(33):10070–10071, 2007.

[134] Jianping Zheng, Jens J Birktoft, Yi Chen, Tong Wang, Ruojie Sha, Pamela E Constantinou, Stephan L Ginell, Chengde Mao, and Nadrian C Seeman. From molecular

to macroscopic via the rational design of a self-assembled 3D DNA crystal. *Nature*, 461(7260):74–77, 2009.

[135] Alexey Y. Koyfman, Sergei N. Magonov, and Norbert O. Reich. Self-Assembly of DNA Arrays into Multilayer Stacks. *Langmuir*, 25(2):1091–1096, 2009.

[136] Urmi Majumder, Abhijit Rangnekar, Kurt V. Gothelf, John H. Reif, and Thomas H. LaBean. Design and Construction of Double-Decker Tile as a Route to Three-Dimensional Periodic Assembly of DNA. *J. Am. Chem. Soc.*, 133(11):3843–3845, 2011.

[137] Paul W K Rothemund, Axel Ekani-Nkodo, Nick Papadakis, Ashish Kumar, Deborah Kuchnir Fygenson, and Erik Winfree. Design and Characterization of Programmable DNA Nanotubes. *J. Am. Chem. Soc.*, 126(50):16344–16352, 2004.

[138] Dage Liu, Sung Ha Park, John H Reif, and Thomas H LaBean. DNA nanotubes self-assembled from triple-crossover tiles as templates for conductive nanowires. *Proc. Natl. Acad. Sci.*, 101(3):717–722, 2004.

[139] James C. Mitchell, J. Robin Harris, Jonathan Malo, Jonathan Bath, and Andrew J. Turberfield. Self-Assembly of Chiral DNA Nanotubes. *J. Am. Chem. Soc.*, 126(50):16342–16343, 2004.

[140] Patrick O'Neill, Paul W K Rothemund, Ashish Kumar, and D. K. Fygenson. Sturdier DNA Nanotubes via Ligation. *Nano Lett.*, 6(7):1379–1383, 2006.

[141] J H Chen and Nadrian C Seeman. Synthesis from DNA of a molecule with the connectivity of a cube. *Nature*, 350(6319):631–3, 1991.

[142] Yuwen Zhang and Nadrian C Seeman. Construction of a DNA-Truncated Octahedron. *J. Am. Chem. Soc.*, 116(5):1661–1669, 1994.

[143] William M. Shih, Joel D. Quispe, and Gerald F. Joyce. A 1.7-kilobase single-stranded DNA that folds into a nanoscale octahedron. *Nature*, 427(6975):618–21, 2004.

[144] R. P. Goodman. Rapid Chiral Assembly of Rigid DNA Building Blocks for Molecular Nanofabrication. *Science (80-.).*, 310(5754):1661–1665, 2005.

[145] Christoph M Erben, Russell P Goodman, and Andrew J Turberfield. A Self-Assembled DNA Bipyramid. *J. Am. Chem. Soc.*, 129(22):6992–6993, 2007.

[146] Yu He, Tao Ye, Min Su, Chuan Zhang, Alexander E Ribbe, Wen Jiang, and Chengde Mao. Hierarchical self-assembly of DNA into symmetric supramolecular polyhedra. *Nature*, 452(7184):198–201, 2008.

[147] Bryan Wei, Mingjie Dai, and Peng Yin. Complex shapes self-assembled from single-stranded DNA tiles. *Nature*, 485(7400):623–626, 2012.

[148] Yonggang Ke, Luvena L Ong, William M Shih, and Peng Yin. Three-Dimensional Structures Self-Assembled from DNA Bricks. *Science (80-.).*, 338(6111):1177–1183, 2012.

[149] D. Han, S. Pal, Y. Yang, S. Jiang, J. Nangreave, Y. Liu, and H. Yan. DNA Gridiron Nanostructures Based on Four-Arm Junctions. *Science (80-.).*, 339(6126):1412–1415, 2013.

[150] Paul W K Rothemund. Folding DNA to create nanoscale shapes and patterns. *Nature*, 440(7082):297–302, 2006.

[151] Andre V Pinheiro, Dongran Han, William M Shih, and Hao Yan. Challenges and opportunities for structural DNA nanotechnology. *Nat. Nanotechnol.*, 6(12):763–772, 2011.

[152] Masayuki Endo, Kumi Hidaka, Takayuki Kato, Keiichi Namba, and Hiroshi Sugiyama. DNA Prism Structures Constructed by Folding of Multiple Rectangular Arms. *J. Am. Chem. Soc.*, 131(43):15570–15571, 2009.

[153] Yonggang Ke, Jaswinder Sharma, Minghui Liu, Kasper Jahn, Yan Liu, and Hao Yan. Scaffolded DNA Origami of a DNA Tetrahedron Molecular Container. *Nano Lett.*, 9(6):2445–2447, 2009.

[154] Ebbe S Andersen, Mingdong Dong, Morten M Nielsen, Kasper Jahn, Ramesh Subramani, Wael Mamdouh, Monika M Golas, Bjoern Sander, Holger Stark, Cristiano L P Oliveira, Jan Skov Pedersen, Victoria Birkedal, Flemming Besenbacher, Kurt V Gothelf, and Jørgen Kjems. Self-assembly of a nanoscale DNA box with a controllable lid. *Nature*, 459(7243):73–76, 2009.

[155] Shawn M. Douglas, Hendrik Dietz, Tim Liedl, Björn Högberg, Franziska Graf, and William M. Shih. Self-assembly of DNA into nanoscale three-dimensional shapes. *Nature*, 459(7245):414–418, 2009.

[156] X.-c. Bai, Thomas G Martin, Sjors H W Scheres, and Hendrik Dietz. Cryo-EM structure of a 3D DNA-origami object. *Proc. Natl. Acad. Sci.*, 109(49):20012–20017, 2012.

[157] Shawn M Douglas, James J Chou, and William M Shih. DNA-nanotube-induced alignment of membrane proteins for NMR structure determination. *Proc. Natl. Acad. Sci.*, 104(16):6644–6648, 2007.

[158] Dominik J. Kauert, Thomas Kurth, Tim Liedl, and Ralf Seidel. Direct Mechanical Measurements Reveal the Material Properties of 3D DNA-Origami. *Biophys. J.*, 102(3):421a, 2012.

[159] Daniel Schiffels, Tim Liedl, and Deborah K. Fygenson. Nanoscale Structure and Microscale Stiffness of DNA Nanotubes. *ACS Nano*, 7(8):6700–6710, 2013.

[160] Yonggang Ke, Shawn M. Douglas, Minghui Liu, Jaswinder Sharma, Anchi Cheng, Albert Leung, Yan Liu, William M. Shih, and Hao Yan. Multilayer DNA Origami Packed on a Square Lattice. *J. Am. Chem. Soc.*, 131(43):15903–15908, 2009.

[161] Shawn M. Douglas, Adam H. Marblestone, Surat Teerapittayanon, Alejandro Vazquez, George M. Church, and William M. Shih. Rapid prototyping of 3D DNA-origami shapes with caDNAno. *Nucleic Acids Res.*, 37(15):5001–5006, 2009.

[162] Yonggang Ke, Niels V. Voigt, Kurt V. Gothelf, and William M. Shih. Multilayer DNA Origami Packed on Hexagonal and Hybrid Lattices. *J. Am. Chem. Soc.*, 134(3):1770–1774, 2012.

[163] Thomas G. Martin and Hendrik Dietz. Magnesium-free self-assembly of multi-layer DNA objects. *Nat. Commun.*, 3:1103, 2012.

[164] Hendrik Dietz, Shawn M Douglas, and William M Shih. Folding DNA into Twisted and Curved Nanoscale Shapes. *Science (80-.).*, 325(5941):725–730, 2009.

[165] Dongran Han, Suchetan Pal, Jeanette Nangreave, Zhengtao Deng, Yan Liu, and Hao Yan. DNA Origami with Complex Curvatures in Three-Dimensional Space. *Science (80-.).*, 332(6027):342–346, 2011.

[166] Tim Liedl, Björn Högberg, Jessica Tytell, Donald E Ingber, and William M Shih. Self-assembly of three-dimensional prestressed tensegrity structures from DNA. *Nat. Nanotechnol.*, 5(7):520–524, 2010.

[167] Lifeng Zhou, Alexander E Marras, Hai-jun Su, and Carlos E Castro. DNA Origami Compliant Nanostructures with Tunable Mechanical Properties. *ACS Nano*, 8(1):27–34, 2014.

[168] Wenyan Liu, Hong Zhong, Risheng Wang, and Nadrian C. Seeman. Crystalline Two-Dimensional DNA-Origami Arrays. *Angew. Chemie Int. Ed.*, 50(1):264–267, 2011.

[169] Zhao Zhao, Yan Liu, and Hao Yan. Organizing DNA Origami Tiles into Larger Structures Using Preformed Scaffold Frames. *Nano Lett.*, 11(7):2997–3002, 2011.

[170] Yangyang Yang, Masayuki Endo, Kumi Hidaka, and Hiroshi Sugiyama. Photo-Controllable DNA Origami Nanostructures Assembling into Predesigned Multiorientational Patterns. *J. Am. Chem. Soc.*, 134(51):20645–20653, 2012.

[171] Ralf Jungmann, Max Scheible, Anton Kuzyk, Günther Pardatscher, Carlos E Castro, and Friedrich C Simmel. DNA origami-based nanoribbons: assembly, length distribution, and twist. *Nanotechnology*, 22(27):275301, 2011.

[172] Sungwook Woo and Paul W K Rothemund. Programmable molecular recognition based on the geometry of DNA nanostructures. *Nat. Chem.*, 3(8):620–627, 2011.

[173] Thomas Tigges, Thomas Heuser, Rahul Tiwari, and Andreas Walther. 3D DNA Origami Cuboids as Monodisperse Patchy Nanoparticles for Switchable Hierarchical Self-Assembly. *Nano Lett.*, 16(12):7870–7874, 2016.

[174] Yusuke Yonamine, Keitel Cervantes-Salguero, Kosuke Minami, Ibuki Kawamata, Waka Nakanishi, Jonathan P Hill, Satoshi Murata, and Katsuhiko Ariga. Supramolecular 1-D polymerization of DNA origami through a dynamic process at the 2-dimensionally confined airwater interface. *Phys. Chem. Chem. Phys.*, 18(18):12576–12581, 2016.

[175] Dongran Han, Suchetan Pal, Yan Liu, and Hao Yan. Folding and cutting DNA into reconfigurable topological nanostructures. *Nat. Nanotechnol.*, 5(10):712–717, 2010.

[176] Akinori Kuzuya, Yusuke Sakai, Takahiro Yamazaki, Yan Xu, and Makoto Komiyama. Nanomechanical DNA origami 'single-molecule beacons' directly imaged by atomic force microscopy. *Nat. Commun.*, 2:449, 2011.

[177] Reza M. Zadegan, Mette D E Jepsen, Karen E. Thomsen, Anders H. Okholm, David H. Schaffert, Ebbe S. Andersen, Victoria Birkedal, and Jørgen Kjems. Construction of a 4 Zeptoliters Switchable 3D DNA Box Origami. *ACS Nano*, 6(11):10050–10053, 2012.

[178] Shawn M Douglas, Ido Bachelet, and G. M. Church. A Logic-Gated Nanorobot for Targeted Transport of Molecular Payloads. *Science (80-.).*, 335(6070):831–834, 2012.

[179] Carlos E Castro, Hai-Jun Su, Alexander E Marras, Lifeng Zhou, and Joshua Johnson. Mechanical design of DNA nanostructures. *Nanoscale*, 7(14):5913–5921, 2015.

[180] Lifeng Zhou, Alexander E. Marras, Hai-Jun Su, and Carlos E. Castro. Direct Design of an Energy Landscape with Bistable DNA Origami Mechanisms. *Nano Lett.*, 15(3):1815–1821, 2015.

[181] Lifeng Zhou, Alexander E. Marras, Carlos E. Castro, and Hai-Jun Su. Pseudorigid-Body Models of Compliant DNA Origami Mechanisms. *J. Mech. Robot.*, 8(5):051013, 2016.

[182] Alexander E Marras, Lifeng Zhou, Hai-Jun Su, and Carlos E Castro. Programmable motion of DNA origami mechanisms. *Proc. Natl. Acad. Sci.*, 112(3):713–718, 2015.

[183] A. E. Marras, L. Zhou, V. Kolliopoulos, H.-J. Su, and C. E. Castro. Directing folding pathways for multi-component DNA origami nanostructures with complex topology. *New J. Phys.*, 18(5):055005, 2016.

[184] P. Ketterer, E. M. Willner, and H. Dietz. Nanoscale rotary apparatus formed from tight-fitting 3D DNA components. *Sci. Adv.*, 2(2):e1501209–e1501209, 2016.

[185] Thomas Gerling, Klaus F. Wagenbauer, Andrea M. Neuner, and Hendrik Dietz. Dynamic DNA devices and assemblies formed by shape-complementary, non-base pairing 3D components. *Science (80-.).*, 347(6229):1446–1452, 2015.

[186] Gabriel J. Lavella, Amol D. Jadhav, and Michel M. Maharbiz. A Synthetic Chemomechanical Machine Driven by LigandReceptor Bonding. *Nano Lett.*, 12(9):4983–4987, 2012.

[187] Jonathan List, Michael Weber, and Friedrich C. Simmel. Hydrophobic Actuation of a DNA Origami Bilayer Structure. *Angew. Chemie Int. Ed.*, 53(16):4236–4239, 2014.

[188] Anton Kuzyk, Robert Schreiber, Hui Zhang, Alexander O Govorov, Tim Liedl, and Na Liu. Reconfigurable 3D plasmonic metamolecules. *Nat. Mater.*, 13(9):862–866, 2014.

[189] Veikko Linko and Hendrik Dietz. The enabled state of DNA nanotechnology. *Curr. Opin. Biotechnol.*, 24(4):555–561, aug 2013.

[190] Fei Zhang, Jeanette Nangreave, Yan Liu, and Hao Yan. Structural DNA Nanotechnology: State of the Art and Future Perspective. *J. Am. Chem. Soc.*, 136(32):11198–11211, 2014.

[191] Donglu Shi, Zizheng Guo, and Nicholas Bedford. DNA Nanotechnology. In *Nanomater. Devices*, pages 317–337. Elsevier, Massachusetts, 2015.

[192] R. Phillips, J. Kondev, J. Theriot, and H. G. Garcia. *Physical Biology of the Cell*. Garland Science, New York, 2013.

[193] B. Alberts, D. Bray, K. Hopkin, A. Johnson, J. Lewis, M. Raff, K. Roberts, and P. Walter. *Essential Cell Biology*. Garland Science, New York, 2004.

[194] M. Spencer. The stereochemistry of deoxyribonucleic acid. I. Covalent bond lengths and angles. *Acta Crystallogr.*, 12(1):59–65, 1959.

[195] Carlos Ernesto Castro, Fabian Kilchherr, Do-Nyun Kim, Enrique Lin Shiao, Tobias Wauer, Philipp Wortmann, Mark Bathe, and Hendrik Dietz. A primer to scaffolded DNA origami. *Nat. Methods*, 8(3):221–229, 2011.

[196] Eric T. Kool. Hydrogen bonding, base stacking, and steric effects in dna replication. *Annu. Rev. Biophys. Biomol. Struct.*, 30(1):1–22, 2001.

[197] J.-P. J. Sobczak, Thomas G. Martin, Thomas Gerling, and Hendrik Dietz. Rapid Folding of DNA into Nanoscale Shapes at Constant Temperature. *Science (80-.).*, 338(6113):1458–1461, 2012.

[198] Peter Yakovchuk. Base-stacking and base-pairing contributions into thermal stability of the DNA double helix. *Nucleic Acids Res.*, 34(2):564–574, 2006.

[199] M.C. Murphy, Ivan Rasnik, Wei Cheng, Timothy M Lohman, and Taekjip Ha. Probing Single-Stranded DNA Conformational Flexibility Using Fluorescence Spectroscopy. *Biophys. J.*, 86(4):2530–2537, 2004.

[200] M D Wang, H Yin, R Landick, J Gelles, and S M Block. Stretching DNA with optical tweezers. *Biophys. J.*, 72(3):1335–46, 1997.

[201] Alex E. Marras, Haijun J. Su, and Carlos E. Castro. Design of DNA Origami Machines

and Mechanisms. In *Vol. 9 Micro- Nano-Systems Eng. Packag. Parts A B*, volume 11, page 301. ASME, 2012.

[202] Remi Veneziano, Sakul Ratanalert, K. Zhang, Fei Zhang, Hao Yan, Wah Chiu, and Mark Bathe. Designer nanoscale DNA assemblies programmed from the top down. *Science (80-.).*, 352(6293):1534–1534, 2016.

[203] Cathal J. Kearney, Christopher R. Lucas, Fergal J. O'Brien, and Carlos E. Castro. DNA Origami: Folded DNA-Nanodevices That Can Direct and Interpret Cell Behavior. *Adv. Mater.*, 28(27):5509–5524, 2016.

[204] Tae-Gon Cha, Jing Pan, Haorong Chen, Janette Salgado, Xiang Li, Chengde Mao, and Jong Hyun Choi. A synthetic DNA motor that transports nanoparticles along carbon nanotubes. *Nat. Nanotechnol.*, 9(1):39–43, 2013.

[205] Yann Astier, Hagan Bayley, and Stefan Howorka. Protein components for nanodevices. *Curr. Opin. Chem. Biol.*, 9(6):576–584, 2005.

[206] John B. Matson, R. Helen Zha, and Samuel I. Stupp. Peptide self-assembly for crafting functional biological materials. *Curr. Opin. Solid State Mater. Sci.*, 15(6):225–235, 2011.

[207] Po-Ssu Huang, Scott E. Boyken, and David Baker. The coming of age of de novo protein design. *Nature*, 537(7620):320–327, 2016.

[208] S Sacanna, W T M Irvine, P M Chaikin, and D J Pine. Lock and key colloids. *Nature*, 464(7288):575–578, 2010.

[209] Daniel Ortiz, Kevin L. Kohlstedt, Trung Dac Nguyen, and Sharon C. Glotzer. Self-assembly of reconfigurable colloidal molecules. *Soft Matter*, 10(20):3541, 2014.

[210] Carl P Goodrich and Michael P Brenner. Using active colloids as machines to weave and braid on the micrometer scale. *Proc. Natl. Acad. Sci.*, 114(2):257–262, 2017.

[211] Yugang Zhang, Suchetan Pal, Babji Srinivasan, Thi Vo, Sanat Kumar, and Oleg Gang. Selective transformations between nanoparticle superlattices via the reprogramming of DNA-mediated interactions. *Nat. Mater.*, 14(8):840–847, 2015.

[212] Anna Klinkova, Rachelle M Choueiri, and Eugenia Kumacheva. Self-assembled plasmonic nanostructures. *Chem. Soc. Rev.*, 43(11):3976, 2014.

[213] Kwanoh Kim, Jianhe Guo, Xiaobin Xu, and D. L. Fan. Recent Progress on Man-Made Inorganic Nanomachines. *Small*, 11(33):4037–4057, 2015.

[214] Jonathan List, Elisabeth Falgenhauer, Enzo Kopperger, Günther Pardatscher, and Friedrich C. Simmel. Long-range movement of large mechanically interlocked DNA nanostructures. *Nat. Commun.*, 7:12414, 2016.

[215] Anton Kuzyk, Yangyang Yang, Xiaoyang Duan, Simon Stoll, Alexander O Govorov, Hiroshi Sugiyama, Masayuki Endo, and Na Liu. A light-driven three-dimensional plasmonic nanosystem that translates molecular motion into reversible chiroptical function. *Nat. Commun.*, 7:10591, 2016.

[216] Haitian Xu, Steven Jones, Byoung-Chul Choi, and Reuven Gordon. Characterization of Individual Magnetic Nanoparticles in Solution by Double Nanohole Optical Tweezers. *Nano Lett.*, 16(4):2639–2643, 2016.

[217] Jenny V. Le, Yi Luo, Michael A. Darcy, Christopher R. Lucas, Michelle F. Goodwin, Michael G. Poirier, and Carlos E. Castro. Probing Nucleosome Stability with a DNA Origami Nanocaliper. *ACS Nano*, 10(7):7073–7084, 2016.

[218] Jonas J. Funke and Hendrik Dietz. Placing molecules with Bohr radius resolution using DNA origami. *Nat. Nanotechnol.*, 11(1):47–52, 2016.

[219] H Isambert, P Venier, A C Maggs, A Fattoum, R Kassab, D Pantaloni, and M F Carlier. Flexibility of actin filaments derived from thermal fluctuations. Effect of bound nucleotide, phalloidin, and muscle regulatory proteins. *J. Biol. Chem.*, 270(19):11437–44, may 1995.

[220] F. Gittes, B. Mickey, J. Nettleton, and J. Howard. Flexural rigidity of microtubules and actin filaments measured from thermal fluctuations in shape. *J. Cell Biol.*, 120(4):923–34, 1993.

[221] Carlos E. Castro, Jijun Dong, Mary C. Boyce, Susan Lindquist, and Matthew J. Lang. Physical Properties of Polymorphic Yeast Prion Amyloid Fibers. *Biophys. J.*, 101(2):439–448, 2011.

[222] Andrea Ranzoni, Xander J. A. Janssen, Mikhail Ovsyanko, Leo J. van IJzendoorn, and Menno W. J. Prins. Magnetically controlled rotation and torque of uniaxial microactuators for lab-on-a-chip applications. *Lab Chip*, 10(2):179–188, 2010.

[223] Maarten M van Oene, Laura E. Dickinson, Francesco Pedaci, Mariana Köber, David Dulin, Jan Lipfert, and Nynke H. Dekker. Biological Magnetometry: Torque on Superparamagnetic Beads in Magnetic Fields. *Phys. Rev. Lett.*, 114(21):218301, 2015.

[224] Fabian Kilchherr, Christian Wachauf, Benjamin Pelz, Matthias Rief, Martin Zacharias, and Hendrik Dietz. Single-molecule dissection of stacking forces in DNA. *Science (80-.).*, 353(6304):aaf5508–aaf5508, 2016.

[225] Minghui Liu, Jinglin Fu, Christian Hejesen, Yuhe Yang, Neal W Woodbury, Kurt Gothelf, Yan Liu, and Hao Yan. A DNA tweezer-actuated enzyme nanoreactor. *Nat. Commun.*, 4:2127, 2013.

[226] Jin-Woo Choi, Kwang W. Oh, Jennifer H. Thomas, William R. Heineman, H. Brian Halsall, Joseph H. Nevin, Arthur J. Helmicki, H. Thurman Henderson, and Chong H. Ahn. An integrated microfluidic biochemical detection system for protein analysis with magnetic bead-based sampling capabilities. *Lab Chip*, 2(1):27–30, 2002.

[227] Stephane Mornet, Sebastien Vasseur, Fabien Grasset, and Etienne Duguet. Magnetic nanoparticle design for medical diagnosis and therapy. *J. Mater. Chem.*, 14(14):2161, 2004.

[228] Akira Ito, Masashige Shinkai, Hiroyuki Honda, and Takeshi Kobayashi. Medical application of functionalized magnetic nanoparticles. *J. Biosci. Bioeng.*, 100(1):1–11, 2005.

[229] Martin A M Gijs. Magnetic bead handling on-chip: new opportunities for analytical applications. *Microfluid. Nanofluidics*, 1(1):22–40, 2004.

[230] Ioannis Petousis, Erik Homburg, Roy Derks, and Andreas Dietzel. Transient behaviour of magnetic micro-bead chains rotating in a fluid by external fields. *Lab Chip*, 7(12):1746, 2007.

[231] S. Krishnamurthy, A. Yadav, P. E. Phelan, R. Calhoun, A. K. Vuppu, A. A. Garcia, and M. A. Hayes. Dynamics of rotating paramagnetic particle chains simulated by particle dynamics, Stokesian dynamics and lattice Boltzmann methods. *Microfluid. Nanofluidics*, 5(1):33–41, 2008.

[232] Y. Gao, M. A. Hulsen, T. G. Kang, and J. M. J. den Toonder. Numerical and experimental study of a rotating magnetic particle chain in a viscous fluid. *Phys. Rev. E*, 86(4):041503, 2012.

[233] Sonia Melle, Gerald G. Fuller, and Miguel A. Rubio. Structure and dynamics of magnetorheological fluids in rotating magnetic fields. *Phys. Rev. E*, 61(4):4111–4117, 2000.

[234] Juan de Vicente, Daniel J. Klingenberg, and Roque Hidalgo-Alvarez. Magnetorheological fluids: a review. *Soft Matter*, 7(8):3701, 2011.

[235] N Wang, J P Butler, and D E Ingber. Mechanotransduction across the cell surface and through the cytoskeleton. *Science*, 260(5111):1124–7, 1993.

[236] Claire Wilhelm. Out-of-Equilibrium Microrheology inside Living Cells. *Phys. Rev. Lett.*, 101(2):028101, 2008.

[237] H. Lee, A. M. Purdon, and R. M. Westervelt. Manipulation of biological cells using a microelectromagnet matrix. *Appl. Phys. Lett.*, 85(6):1063–1065, 2004.

[238] Vasile I. Furdui, James K Kariuki, and Jed D Harrison. Microfabricated electrolysis pump system for isolating rare cells in blood. *J. Micromechanics Microengineering*, 13(4):S164–S170, 2003.

[239] David W. Inglis, R. Riehn, R. H. Austin, and J. C. Sturm. Continuous microfluidic immunomagnetic cell separation. *Appl. Phys. Lett.*, 85(21):5093–5095, 2004.

[240] Nan Xia, Tom P. Hunt, Brian T. Mayers, Eben Alsberg, George M. Whitesides, Robert M. Westervelt, and Donald E. Ingber. Combined microfluidic-micromagnetic separation of living cells in continuous flow. *Biomed. Microdevices*, 8(4):299–308, 2006.

[241] Jonathan D. Adams and H. Tom Soh. Perspectives on Utilizing Unique Features of Microfluidics Technology for Particle and Cell Sorting. *J. Assoc. Lab. Autom.*, 14(6):331–340, 2009.

[242] Hongbo Peng and Xinsheng Sean Ling. Reverse DNA translocation through a solid-state nanopore by magnetic tweezers. *Nanotechnology*, 20(18):185101, 2009.

[243] C. Hale and J. Darabi. Magnetophoretic-based microfluidic device for DNA isolation. *Biomicrofluidics*, 8(4):044118, 2014.

[244] C. Wyatt Shields IV, Catherine D Reyes, and Gabriel P López. Microfluidic cell sorting: a review of the advances in the separation of cells from debulking to rare cell isolation. *Lab Chip*, 15(5):1230–1249, 2015.

[245] S. Bleil, D. W M Marr, and C. Bechinger. Field-mediated self-assembly and actuation of highly parallel microfluidic devices. *Appl. Phys. Lett.*, 88(26):263515, 2006.

[246] Nicole Pamme. Magnetism and microfluidics. *Lab Chip*, 6(1):24–38, 2006.

[247] T. Henighan, D. Giglio, A. Chen, G. Vieira, and R. Sooryakumar. Patterned magnetic traps for magnetophoretic assembly and actuation of microrotor pumps. *Appl. Phys. Lett.*, 98(10):103505, 2011.

[248] Sonia Melle, Oscar G Calderón, Gerald G Fuller, and Miguel a Rubio. Polarizable particle aggregation under rotating magnetic fields using scattering dichroism. *J. Colloid Interface Sci.*, 247(1):200–9, 2002.

[249] Alexander Weddemann, Frank Wittbracht, Bernhard Eickenberg, and Andreas Hutten. Magnetic Field Induced Assembly of Highly Ordered Two-Dimensional Particle Arrays. *Langmuir*, 26(24):19225–19229, 2010.

[250] Sang Yoon Park, Hiroshi Handa, and Adarsh Sandhu. Magneto-Optical Biosensing Platform Based on Light Scattering from Self-Assembled Chains of Functionalized Rotating Magnetic Beads. *Nano Lett.*, 10(2):446–451, 2010.

[251] Charles E Sing, Lothar Schmid, Matthias F Schneider, Thomas Franke, and Alfredo Alexander-Katz. Controlled surface-induced flows from the motion of self-assembled colloidal walkers. *Proc. Natl. Acad. Sci.*, 107(2):535–540, 2010.

[252] Jing Yan, Moses Bloom, Sung Chul Bae, Erik Luijten, and Steve Granick. Linking synchronization to self-assembly using magnetic Janus colloids. *Nature*, 491(7425):578–581, 2012.

[253] James W. Swan, Paula A. Vasquez, Peggy A. Whitson, E. Michael Fincke, Koichi Wakata, Sandra H. Magnus, Frank De Winne, Michael R. Barratt, Juan H. Agui, Robert D. Green, Nancy R. Hall, Donna Y. Bohman, Charles T. Bunnell, Alice P. Gast, and Eric M. Furst. Multi-scale kinetics of a field-directed colloidal phase transition. *Proc. Natl. Acad. Sci.*, 109(40):16023–16028, 2012.

[254] Di Du, Dichuan Li, Madhuri Thakur, and Sibani Lisa Biswal. Generating an in situ tunable interaction potential for probing 2-D colloidal phase behavior. *Soft Matter*, 9(29):6867, 2013.

[255] James E Martin and Alexey Snezhko. Driving self-assembly and emergent dynamics in colloidal suspensions by time-dependent magnetic fields. *Reports Prog. Phys.*, 76(12):126601, 2013.

[256] Jure Dobnikar, Alexey Snezhko, and Anand Yethiraj. Emergent colloidal dynamics in electromagnetic fields. *Soft Matter*, 9(14):3693, 2013.

[257] J Yan, S C Bae, and S Granick. Rotating crystals of magnetic Janus colloids. *Soft Matter*, 00:1–7, 2014.

[258] Ben H. Erné, Maria Claesson, Stefano Sacanna, Mark Klokkenburg, Emile Bakelaar, and Bonny W.M. Kuipers. Low-frequency complex magnetic susceptibility of magnetic composite microspheres in colloidal dispersion. *J. Magn. Magn. Mater.*, 311(1):145–149, 2007.

[259] X.J.A. Janssen, A.J. Schellekens, K. van Ommering, L.J. van IJzendoorn, and M.W.J. Prins. Controlled torque on superparamagnetic beads for functional biosensors. *Biosens. Bioelectron.*, 24(7):1937–1941, 2009.

[260] Anna C H Coughlan and Michael A. Bevan. Rotating colloids in rotating magnetic fields: Dipolar relaxation and hydrodynamic coupling. *Phys. Rev. E*, 94(4):042613, 2016.

[261] E.C. Stoner and E.P. Wohlfarth. A mechanism of magnetic hysteresis in heterogeneous alloys. *IEEE Trans. Magn.*, 27(4):3475–3518, 1991.

[262] L.D Landau and E.M. Lifshitz. *Fluid Mechanics*. ButterworthHeinemann, Oxford, 2nd ed. edition, 1987.

[263] G. K. Batchelor. *An Introduction to Fluid Dynamics*. Cambridge University Press, Cambridge, 1967.

[264] Albert Folch and Mehmet Toner. Microengineering of Cellular Interactions. *Annu. Rev. Biomed. Eng.*, 2(1):227–256, 2000.

[265] George M Whitesides, Emanuele Ostuni, Shuichi Takayama, Xingyu Jiang, and Donald E Ingber. Soft Lithography in Biology and Biochemistry. *Annu. Rev. Biomed. Eng.*, 3(1):335–373, 2001.

[266] Didier Falconnet, Andrea Koenig, Fabiano Assi, and Marcus Textor. A Combined Photolithographic and Molecular-Assembly Approach to Produce Functional Micropatterns for Applications in the Biosciences. *Adv. Funct. Mater.*, 14(8):749–756, 2004.

[267] Didier Falconnet, Daniela Pasqui, Sunggook Park, Rolf Eckert, Helmut Schift, Jens Gobrecht, Rolando Barbucci, and Marcus Textor. A Novel Approach to Produce Protein Nanopatterns by Combining Nanoimprint Lithography and Molecular Self-Assembly. *Nano Lett.*, 4(10):1909–1914, 2004.

[268] Ravi S. Kane, Shuichi Takayama, Emanuele Ostuni, Donald E. Ingber, and George M. Whitesides. Patterning proteins and cells using soft lithography. *Biomaterials*, 20(23-24):2363–76, 1999.

[269] Brian H Lower, Ruchirej Yongsunthon, F. Paul Vellano, and Steven K Lower. Simultaneous force and fluorescence measurements of a protein that forms a bond between a living bacterium and a solid surface. *J. Bacteriol.*, 187(6):2127–37, 2005.

[270] Steven K. Lower, Christopher J. Tadanier, and Michael F. Hochella. Measuring interfacial and adhesion forces between bacteria and mineral surfaces with biological force microscopy. *Geochim. Cosmochim. Acta*, 64(18):3133–3139, 2000.

Appendix A
DNA Origami Nanomachines Materials and Methods

A.1 Design and Fabrication of Nanoconstructs

The nanoconstructs are formed using the method of DNA origami in which a known long loop of ssDNA, i.e., scaffold, folds into a precise compact geometry using hundreds of designed short ssDNA, i.e., staples, via programmed molecular self-assembly [179]. The staples are piecewise complementary to segments of the scaffold strand. The DNA nanostructures self-assemble when the scaffold, staples, salt and buffer solutions are combined together and subjected to thermal annealing[179]. The 56hb (also referred to as the nano-brick) has 56 dsDNA helices connected together in a honeycomb lattice formation creating a cylindrical construct that is about 40 nm in length with a cross-section of 24 nm (Fig. A.1A-E). Several different modification overhangs can be incorporated into the nano-brick to customize its use. A single ssDNA overhang conjugated with biotin is incorporated on the end (Fig. A.1F) for surface attachment of the lever arm. Five ssDNA overhang which are complementary to ssDNA conjugated with biotin are integrated into the side (Fig. A.1G) to fix one of the hinge lever arms to the surface. One ssDNA overhang complementary to a ssDNA overhang on the nano-platform is assimilated into the side of the nano-brick (Fig. A.1H) for assembly of the nano-rotor. Last, two ssDNA overhang conjugated with digoxigenin are incorporated on the opposite end of the biotin overhang (Fig. A.1I) for bead attachment. Additionally, five ssDNA overhangs which are complementary to ssDNA conjugated with a

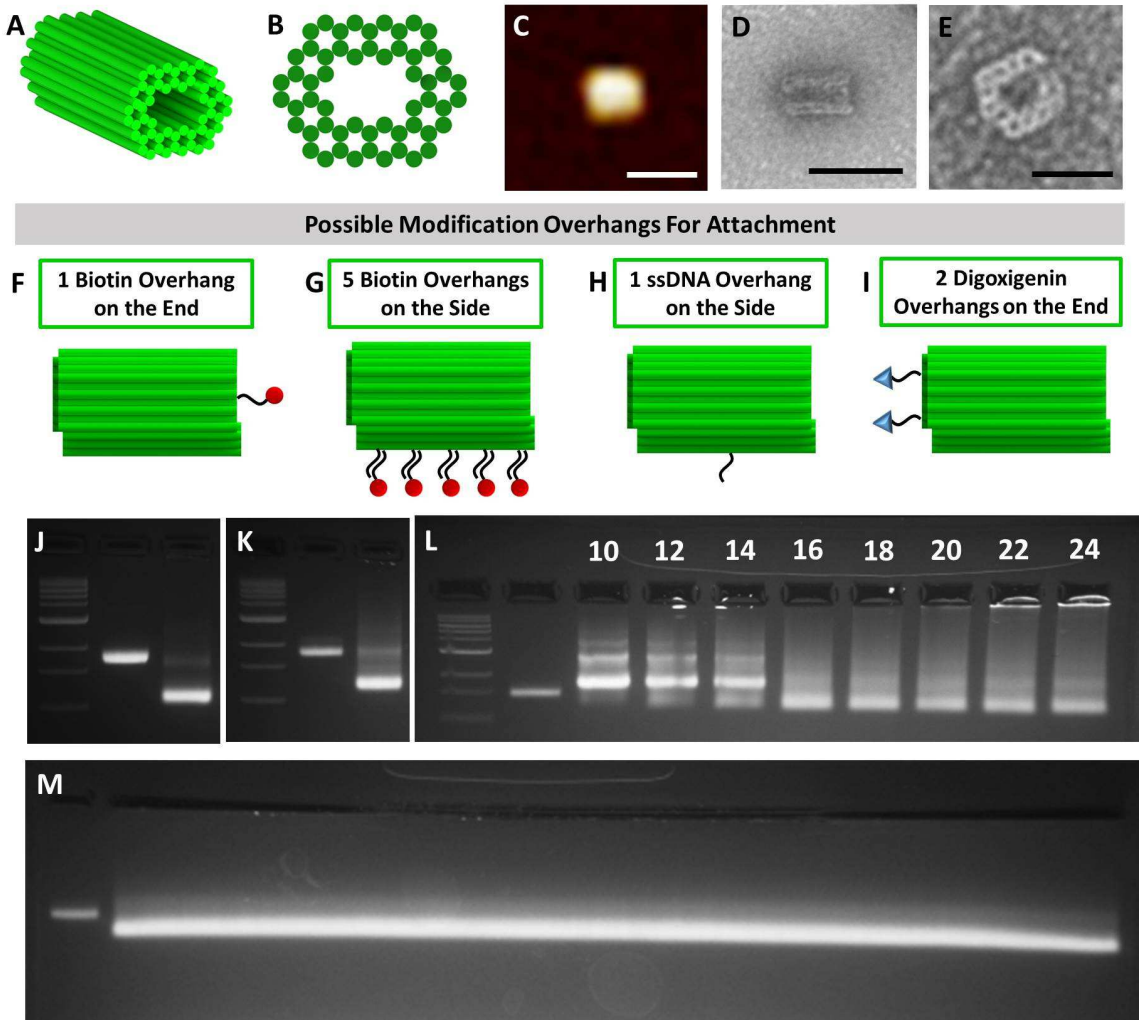

Figure A.1: Nano-Brick Structure. (A) Cylinder model and (B) cross-section of the 56hb nano-brick. (C) AFM and (D) TEM images of side view of nano-brick. Scale bar, 50 nm. (E) TEM image of the cross-section of the nano-brick. Scale bar, 20 nm. Modifications can be made to the nano-brick for different protein and overhang attachments. Nano-brick with (F) one biotin overhang on the end (for lever arm surface attachment), (G) five biotin overhangs on the side (for surface attachment of lever arm on nano-hinge), (H) one ssDNA overhang on the side (for attachment to nano-platform in forming nano-rotor), (I) two digoxigenin overhangs on the end (for bead attachment). The fluorophore overhang attachment sites are not shown. Gel purification of (J) Nano-brick version one and (K) Nano-brick version two (scaffold shift by 30 bases) in 0.5x TAE with 4mM $MgCl_2$. Gel order: One Kilobase DNA Ladder, 7249 Scaffold, Nano-brick. (L) Salt screen of nano-brick version two with $MgCl_2$ salt screen from 10 mM to 24 mM $MgCl_2$. Gel Order: One Kilobase DNA Ladder, 7249 Scaffold, Nano-brick Salt Screen (last 8 wells). (M) Purification of nano-brick version one using a large well. Gel Order: 7249 Scaffold, Nano-brick (large well).

fluorophore are also folded with the structure for visualization under TIRF. Most versions of the nano-brick were folded with 1x FoB (Folding Buffer: 1 mM EDTA, 5 mM NaCl, 5 mM Tris), 18 mM $MgCl_2$ (determined from salt screen (Fig. A.1L), 200 nM Working Stock and 40 nM 7249 Scaffold. However, the nano-brick with the ssDNA overhang for the nano-rotor fabrication is folded with 22 mM $MgCl_2$. Structures were folded in an annealing ramp where it was initially heated to 65°C for 15 minutes, followed by a constant incubation at 52°C, 51°C and 50°C for 4 hours each and then finally cooled to 4°C. Two versions of the nano-brick were assembled which have the same structure design, however, the scaffold was shifted by 30 bases in order to create a distinguishable set of polymerization staples for the second version. Both nano-brick version one (Fig. A.1J) and version two (Fig. A.1K) were gel purified on 0.4x TAE with 4 mM $MgCl_2$ in which the low salt concentration helped to reduce any structure aggregation and increase the concentration of the nano-brick in later attachment recipes. Gel purified structures were used to polymerize the lever arm since PEG-purified structures did not form the lever arm as readily. In order to gel purify 400 μL of nano-bricks in one gel, a large gel with a single large well was utilized as shown in Fig. A.1M.

The base nano-platform used in the assembly of the nano-rotor is composed of 32 dsDNA helices arranged into a two layer honeycomb lattice formation with a rectangular shape of dimensions 60 nm by 27 nm by 6 nm (Fig. A.2A-D). A single ssDNA overhang was incorporated on the top of the platform for attachment to the nano-brick to form the nano-platform (Fig. A.2E) and 22 ssDNA overhangs were included on the bottom which could bind to either a ssDNA conjugated to a Cy3 fluorophore or biotin protein (Fig. A.2F). The nano-platform was folded with 1x FoB (Folding Buffer: 1 mM EDTA, 5 mM NaCl, 5 mM Tris), 18 mM $MgCl_2$, 200 nM Working Stock, 20 nM 7560 Scaffold. Structures were folded in a 2.5 half day annealing ramp such that it is initially heated to 65°C and slowly cooled from 65°C - 62°C at 1°C/1hour, 61°C - 59°C at 1°C/2hours, 58°C - 46°C at 1°C/3hours, 45°C - 40°C at 1°C/1hour, 39°C - 25°C at 1°C/30minutes and 24°C-4°C at °C/1minute. The structures were gel purified in 0.5x TAE with 4 mM $MgCl_2$ (Fig. A.2G)

The nano-hinge has 72 dsDNA helices forming two 36hb honeycomb lattice bundles

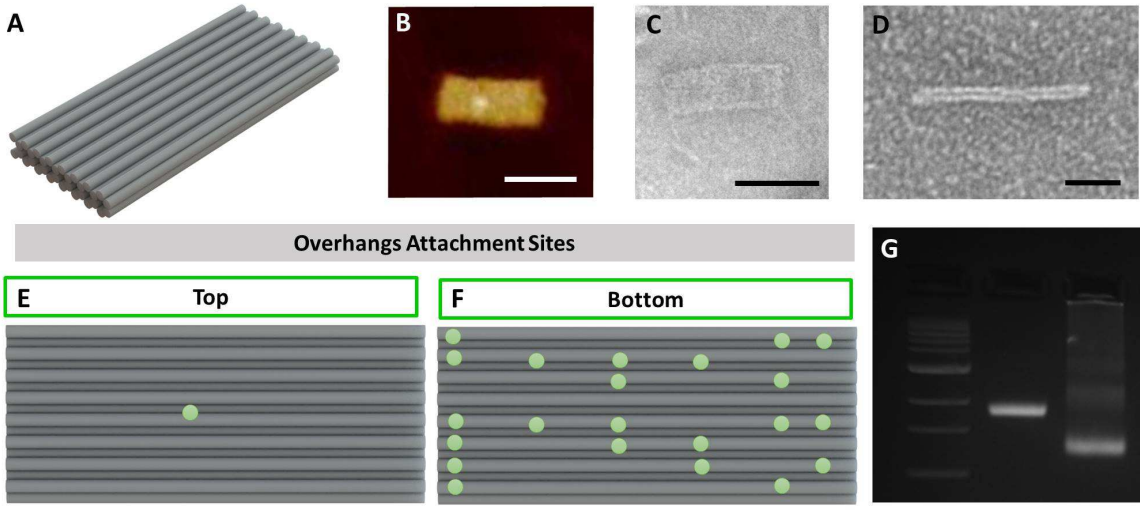

Figure A.2: Nano-Platform Structure. (A) Cylinder model and (B) cross-section of the nano-platform. (C) AFM and (D) TEM images of top view of nano-platform. In AFM image nano-platform has streptavidin attached to top overhang shown in E. Scale bar, 50 nm. (E) TEM image of the side of the nano-brick. Scale bar, 20 nm. Overhang attachment sites for the nano-platform on (E) top (for attachment to nano-rotor) and on (F) bottom (for surface and fluorophore attachment). (G) Gel purification of nano-platform at 0.5x TAE with 4 mM $MgCl_2$. Gel order: One Kilobase Ladder, 7560 Scaffold, Nano-platform.

which are connected to each other through 8 ssDNA from the scaffold strand to create 40 nm long hinge arms (Fig. A.3A-D). On the bottom arm of the hinge, six ssDNA overhangs are incorporated which bind to ssDNA conjugated to biotin for surface attachment. Additionally, eleven ssDNA overhangs which bind to ssDNA conjugated to an Alexa 488 fluorophore were integrated into the structure for visualization under TIRF. Due to the relatively large areal cross-section of the nano-brick and the nano-hinge, staples near the ends (neighbor staples - Fig. A.4A) of the structures were left out of the folding reaction leaving long scaffold loops which, in turn, reduce base stacking between structures. In the salt screen of the nano-hinge, more aggregation appeared in the wells when the nano-hinge was folded with the neighbor staples (Fig. A.3E) compared to when it was folded without the neighbor staples (Fig. A.3F). Additionally, when the nano-hinge was folded at a 40 nM concentration, it would aggregate over time (Fig. A.4C-D). However, when folded at a 20 nM concentration, the nano-hinge didn't aggregate over time (Fig. A.4E-F). Therefore,

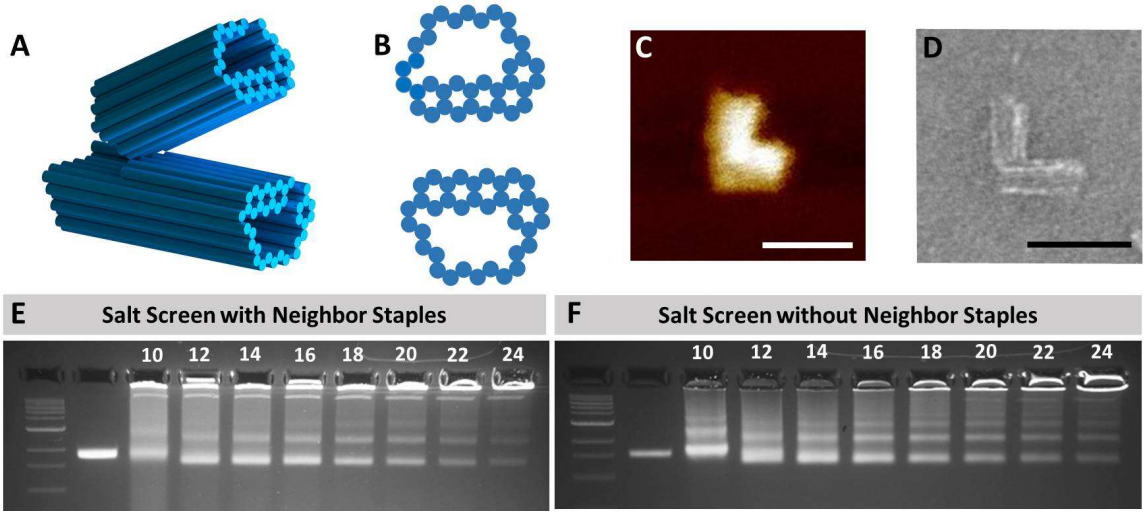

Figure A.3: Nano-hinge Structure. (A) Cylinder model and (B) cross-section of the nano-hinge. (C) AFM and (D) TEM images of side view of nano-hinge. Scale bar, 50 nm. Salt screen of nano-hinge folded (E) with neighbor staples and (F) without neighbor staples from 10 mM to 24 mM $MgCl_2$. Gel order: One Kilobase DNA Ladder, 8064 Scaffold, Nano-hinge Salt Screen (Last 8 wells).

the nano-hinge was folded with 0.5x FoB (1x FoB (Folding Buffer: 1 mM EDTA, 5 mM NaCl, 5 mM Tris), 16 mM $MgCl_2$, 100 nM Working Stock and 20 nM 8064 Scaffold. To fold the hinge it underwent the same 2.5 day annealing ramp that was used in folding the nano-platform. The nano-hinge was also gel purified in 0.5x TAE with 4 mM $MgCl_2$.

A.2 Assembly of Extended Systems

All of the polymerization strands connecting the nano-bricks and nano-hinge were designed with a u-shaped motif where half of them have a higher affinity to attach to one end of the nano-brick while the other half have a higher affinity to the opposite; therefore a single polymerization staple would not hold the nano-bricks together. However, by adding many polymerization staples in series, the binding energy is greatly increased thereby fostering a strong binding affinity to form polymers. In forming the polymers, gel purified nano-bricks were incubated with neighbor and polymerization staples in 5 times excess in an assembly buffer containing 8 mM $MgCl_2$ and 0.2% of the surfactant NP40 at a constant temperature

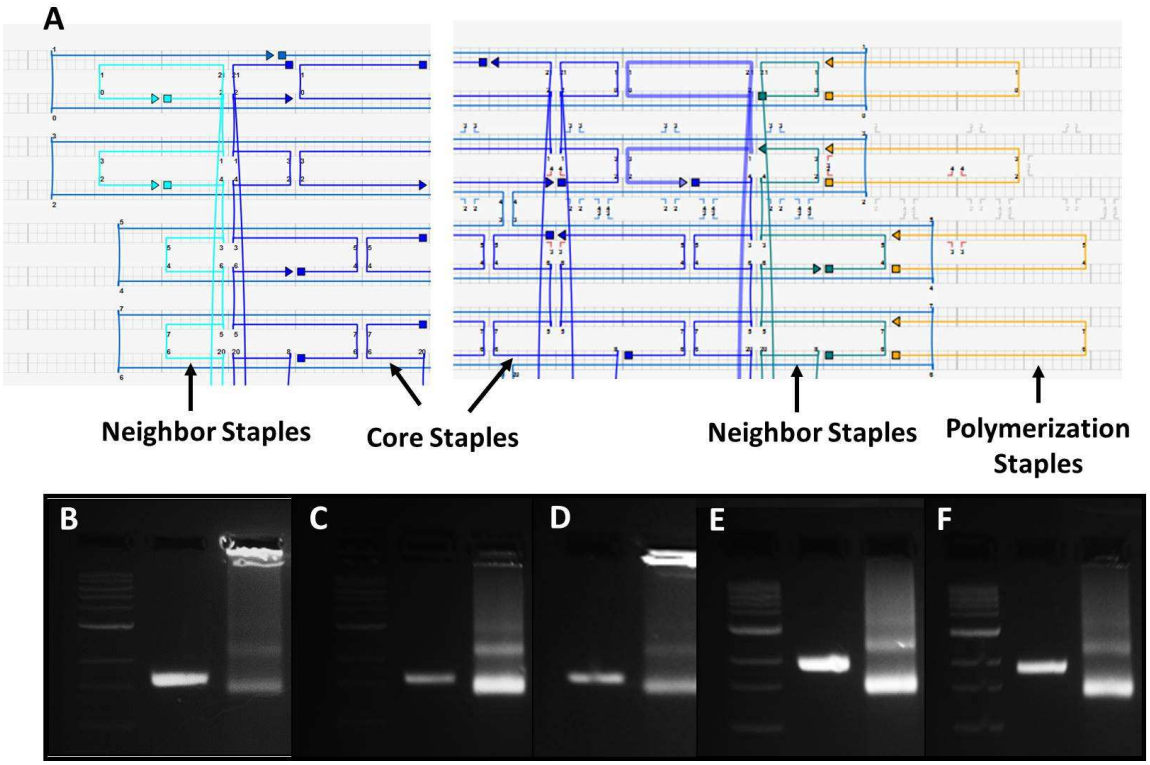

Figure A.4: Nano-hinge Optimization. (A) Part of the caDNAno file for the nano-hinge showing the neighbor staples (cyan), core staples (blue) and polymerization staples (yellow). To optimize the concentration, the nano-hinge was folded with various set of staples at two different concentrations and gel purified. Gel purified nano-hinge (B) at 40 nM concentration folded with core and neighbor staples, (C) at 40 nM concentration folded with core staples and immediately purified after folding, (D) at 40 nM concentration and purified a week after folding, (E) at 20 nM concentration folded with core staples and immediately purified after folding, and (F) at 20 nM concentration folded with core staples and purified a week after folding.

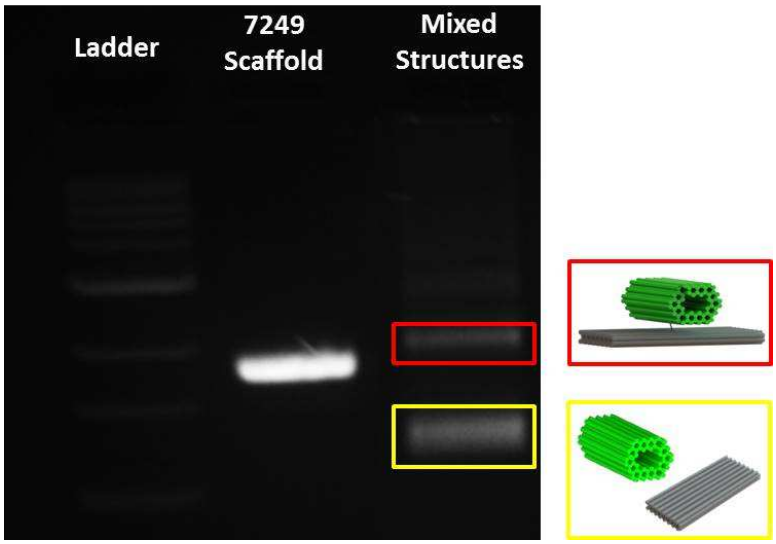

Figure A.5: Nano-rotor Purification Gel. Nano-bricks are incubated overnight at 37°C with nano-platforms in a 1:1 ratio. The ssDNA overhang on the nano-brick is complementary to the ssDNA overhang on the nano-platform and binds to form the nano-rotor. Only a portion of the nano-bricks bind to the nano-platforms therefore, a pure nano-rotor sample was exacted out using gel purification. Gel Order: One Kilobase DNA Ladder, 7249 Scaffold (used to fold the nano-brick), and the incubated sample of nano-bricks and nano-platforms in which two bands form nano-rotors (boxed in red) and unattached nano-bricks and nano-platforms (boxed in yellow). Well-folded structures run past their scaffold and multicomponent structures will run slower than single component structures.

of 37°C for 16 - 18 hours when formed in a channel. When fabricated in a tube, the mixture underwent a thermal ramp starting at 45°C and decreased by 2°C every hour until it reached 4°C for 2 cycles. Polymers incubated in the thermal ramp for 1 cycle were much shorter. However, after 3 cycles, the lengths were not significantly longer overall. Furthermore, using surfactants such as NP40 and lowering salt concentration helped to reduce unwanted base stacking and structure aggregation. Yet, if the salt concentration was too low, the polymerization staples will not bind as effectively and the desired structures do not readily form.

The nano-rotor was formed in an overnight incubation at 37°C from attaching PEG-purified nano-bricks designed with a ssDNA overhang on the side of the nano-brick to PEG-purified platform designed with the complementary ssDNA overhang incorporated on

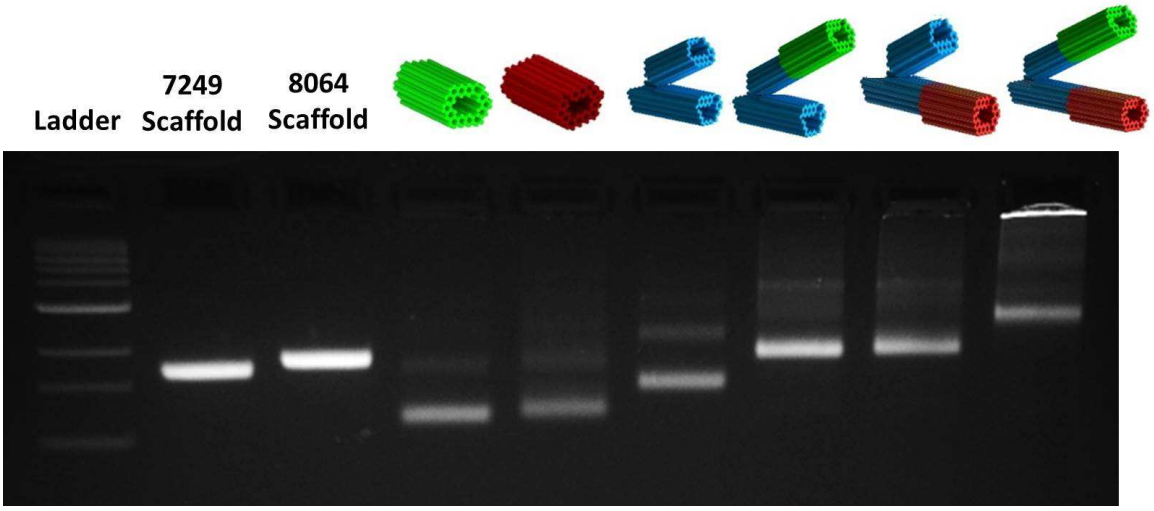

Figure A.6: Nano-hinge with Initial Nano-brick Attachment Purification Gel. Polymerization staples are gel purified out of the samples after initial nano-bricks were attached to the nano-hinge. Gel Order: One Kilobase DNA Ladder, 7249 Scaffold (folds the nano-bricks (red and green)) 8064 Scaffold (folds the nano-hinge), nano-hinges incubated with green nano-bricks and corresponding polymerization staples, nano-hinges incubated with red nano-bricks corresponding polymerization staples, nano-hinges incubated with green and red nano-bricks corresponding polymerization staples. The nano-hinge with a single nano-brick runs slower than the single nano-hinge or the single nano-brick but faster than the nano-hinge attached to two nano-bricks. As seen in the last three lanes, almost all nano-hinges and nano-bricks attached to one another.

the top of the nano-platform. A pure sample of nano-rotors were gel purified as seen in Fig. A.5 for lever arm attachment in the next step. The lever arms are formed off the gel purified nano-rotors by attaching them to premade micron length levers which were incubated in excess to the nano-rotors and with excess polymerization staples in a thermal ramp that repeats three cycles of cooling the sample from 45°C to 4°C by decreasing the temperature at a rate of 2°C every hour.

In forming the extended hinge the initial PEG-purified nano-bricks were attached to the top and bottom arms of the PEG-purified nano-hinge by incubating them together in equal concentrations with polymerization staples that were in 5x excess to the hinge concentration and neighbor staples that were in 2x excess to the hinge concentration. The nano-bricks were subsequently incubated on a thermal ramp starting at 45°C and decreased by 2°C

every hour until it reached 4°C. The mixture was then gel purified to extract a pure yield of this initial unit as shown in Fig. A.6. This approach, in comparison to incubating it at a constant temperature, greatly increased the attachment efficiency of the nano-brick to the nano-hinge. Additionally, in order to reduce aggregation, six neighbor / polymerization staples which had overlapping sequences between 11 - 14 consecutive bases were not added in the attachment step. None of the staple sequences had similarities above 14 consecutive bases. Next, the stiff extension arms are subsequently formed off these initial nano-brick-hinge units by attaching them to premade micron length rods using the same thermal ramp except that the cycle was repeated two additional times since the concentration of the structures was much lower than in attachment of the first unit.

A.3 Surface Attachment and Bead Labeling

To prepare the structures for actuation, each system had to be fixed to the surface in a channel. Nonspecific binding was reduced by initially cleaning the coverslips with piranha and coating with unmodified and biotin-modified PEG. Free streptavidin was attached to the biotin on the surface. After removing excess streptavidin, the structures were flowed into the channel and attached to the surface. In the case of the rod system, the rod was assembled in the channel due to the entropic limitations of confining a long rod initially to the surface through the attachment of only one biotin to streptavidin. Therefore, in assembling the rod system, a single nano-brick with a biotin overhang on one end was attached initially to the surface. Subsequently, additional nano-bricks were attached end-to-end following an overnight incubation at 37°C with its polymerization staples. Unlike the rod system, the fully assembled rotor and hinge system can be easily attached to the surface since the rotor has eleven biotin overhangs on the bottom of the nano-platform and the nano-hinge has six overhangs on its bottom arm and five biotin overhangs on each sequential nano-brick along the bottom arm. Finally, superparamagnetic beads coated in anti-digoxigenin are flowed into the channel and attach to the digoxigenin overhangs on the ends of the free lever arms of each structure.

A.4 Measuring Lever Arm Persistence Length

Measuring the Variance in Transverse Fluctuations from TEM Images

TEM images of levers were analyzed using MATLAB (Mathworks, Natick, MA, USA). To discretize the shape of the lever, points along the trajectory were manually selected (∼every 50 - 100 nm along the filament path) by clicking on the image. These selected points were used to fit a cubic spline of the trajectory coordinates every ∼5 nm along the filament path to obtain fine resolution of the curvature. Only filaments that were at least 1 μm in length were considered for the shape fluctuation analysis. Configurational distributions were obtained by aligning the filament trajectories so that they started at the origin and initially pointed in the horizontal direction.

The filament persistence length, L_p, is defined as the tangent vector correlation length, or in other words the length over which the filament stays approximately straight when subject to thermal fluctuations, which for a system confined to 2D is defined as:

$$\langle cos[\theta(s) - \theta(0)]\rangle = exp(-\frac{s}{2L_p}) \tag{A.1}$$

where $\theta(s)$ is the angle tangent to the filament at arc length position s. We assumed that filament trajectories are reflective of 2D fluctuations due to the surface deposition. Based on this expression, Isambert et al. [219] derived a relation between the filament L_p and the average transverse fluctuations, $\langle[D(s)]\rangle$, or essentially, the splay width for the configurational distributions previously described [219]:

$$\langle[D(s)]\rangle = L_p^2[2\frac{2}{L_p} + \frac{16}{3}exp(-\frac{s}{2L_p}) - \frac{1}{3}exp(-\frac{s}{2L_p}) - 5] \tag{A.2}$$

The average transverse fluctuations were determined as a function of arc length from the filament configurational distributions. Only the first 1 μm of all filament trajectories was used for this analysis to avoid averaging transverse fluctuations over a smaller number of filaments for larger arc lengths.

Lever arms were manually traced and fit with a cubic spline to obtain fine resolution of the trajectory. Fig. A.7A illustrates an example of traced levers. To obtain configurational

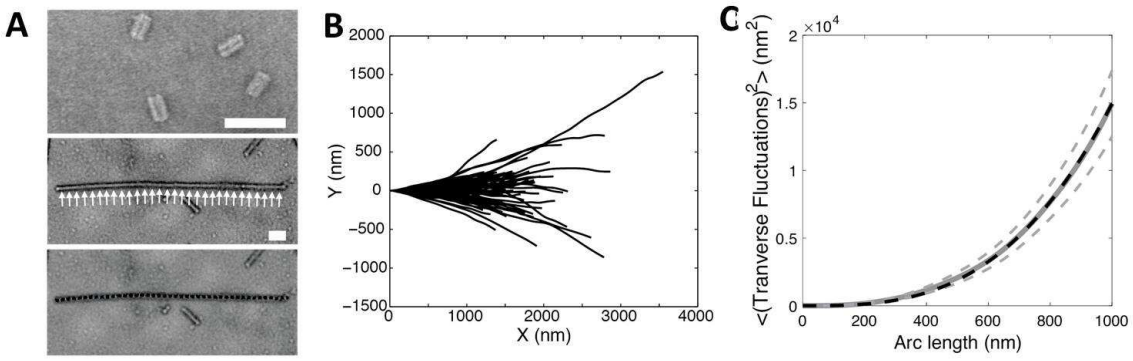

Figure A.7: (A) TEM images illustrating 56-helix DNA origami bundles (nano-brick) (top), lever arm constructed from many 56-helix structures as indicated by the arrows (middle), and a manually traced trajectory fit with a cubic spline (bottom). (B) Many lever arms were traced to construct a conformational distribution. (C) The variance of the transverse fluctuations were fit to equation A.2 to give a persistence length of 22 ± 4 μm. The dashed lines indicate ± standard deviation of the variance in the transverse fluctuations, which were used to determine the uncertainty in persistence length.

distributions, lever trajectories were aligned so that they all started at the origin ($x = 0$, $y = 0$) and pointed initially in the positive x-direction with zero slope. Fig. A.7B shows configurational distributions for the 56hb (nano-brick) (N=68). The filaments exhibited lengths of 1.74 ± 0.52 μm, with the average length corresponding to approximately 41 units in the lever arm. The levers generally point in the x-direction with the splay width decreasing for larger cross-sections.

The L_p of the lever arm was characterized by calculating the average of the transverse fluctuations squared from the configurational distributions and fitting equation A.2. Fig. A.7C shows the model fits compared to the data, which resulted in L_p of 22 ± 4 μm, based on the fit with R2 = 99.9%. As expected the fluctuations decrease for larger, or equivalently stiffer, cross-sections. The dashed gray lines show the standard error of the mean when calculating the mean of the transverse fluctuations squared as a function of arc length. The uncertainty in the persistence length was determined by fitting equation A.2 to these dashed gray lines to determine persistence length for transverse fluctuations up to one standard deviation from the mean.

Measuring Thermal Fluctuations from TIRF Images

An alternative method for calculating the persistence length was implemented from measuring the thermal fluctuations from TIRF images of the lever arm sandwiched between two coverslips. The coverslips were initially treated with casein in order to reduce any non-specific binding of the DNA levers. Initially, 20 μL of 1 mg/mL of casein dissolved in 0.5x TAE with 4 mM $MgCl_2$ were incubated between two coverslips for 10 minutes followed by a wash with ddH_2O. Then 0.5 μL of the DNA lever labeled with fluorophores are sandwiched between the coverslips for imaging. TIRF images are recorded at 5 Hz up to 300 frames. Using a MATLAB (Mathworks, Natick, MA, USA), the bending fluctuations of the lever arm in each frame is fitted to a superposition of Fourier modes as has previously been done for actin filaments, microtubules, and amyloid fibers [220, 221]. The fluctuation/variance in amplitudes determined in each mode gives an independent approximation of the rigidity of the structure. Preliminary results for 10 lever arms give a persistence length of 27 ± 19 μm. It was observed that some of the structures are photobleaching over time therefore, further data needs to be required in which the photobeaching is reduced by increasing exposure, decreasing laser intensity and turning the lasers off in between measurements.